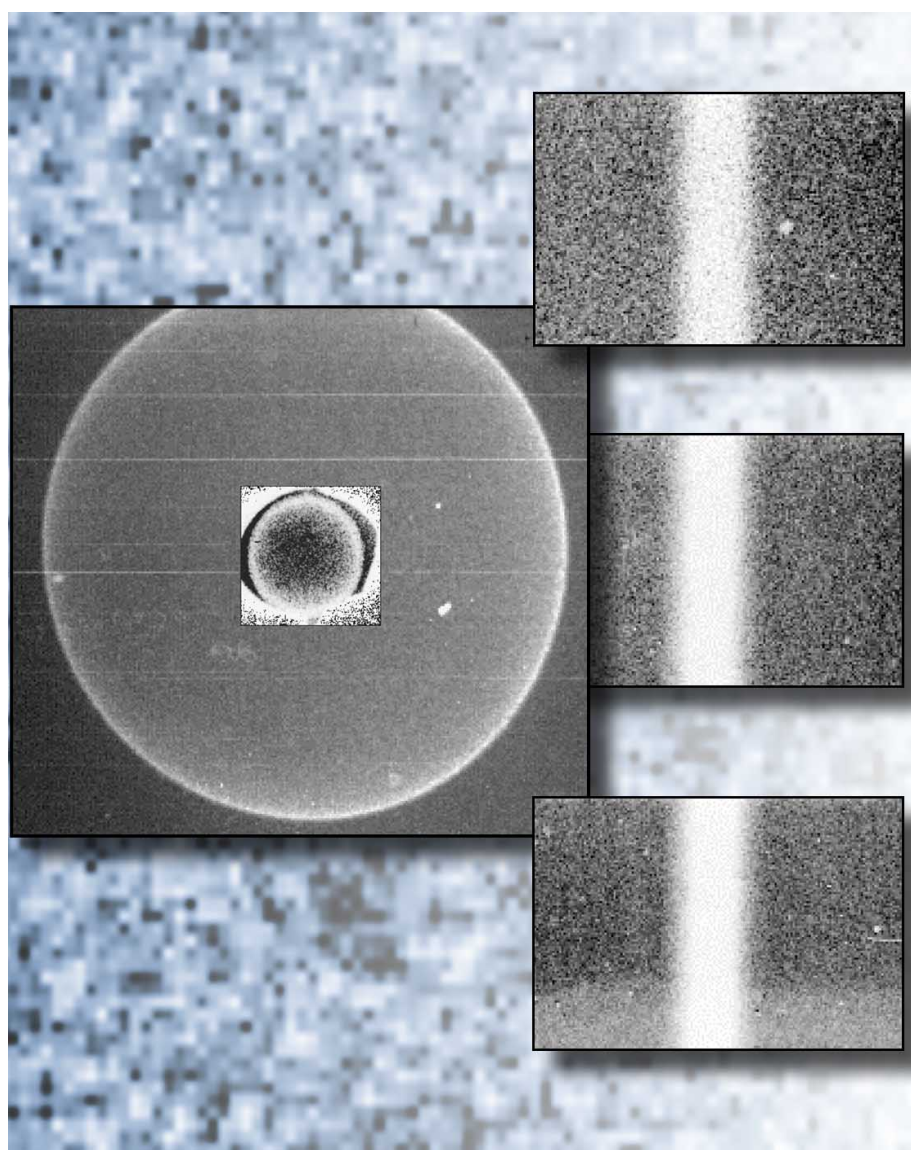


INERTIAL CONFINEMENT FUSION

Lawrence
Livermore
National
Laboratory

ICF Quarterly Report

April-June 1999, Volume 9, Number 3



*Control of Debris
and Shrapnel
Generation in the
National Ignition
Facility*

*X-Ray Backlighting
for the National
Ignition Facility*

*Using Intense
Lasers in the
Laboratory to
Model
Astrophysical
Phenomena*

*Unconverted Light
Management for
the National
Ignition Facility*

*X-Ray Backlighting for the
National Ignition Facility*

UCRL-LR-105821-99-3

The Cover: Gated, 4.7-keV, x-ray images from a new x-ray backlighting technique. The technique uses backlit pinholes, combining the arbitrary-duration, fixed-resolution advantage of area backlighters with the efficiency of point-projection backlighters. The smaller snapshots (right) show a series of 21- μm -resolution backlit images of a 50- μm tungsten wire taken at 1-ns intervals. The larger snapshot (left) compares the backlit image of an imploding NIF-scale, 3-mm-diam capsule using the new technique with the backlit image (centered inset) of a Nova- or OMEGA-scale, 500- μm -diam capsule using the traditional area-backlighter technique. The new technique used 10 \times less laser power, yet provided a more uniformly illuminated image over a 30 \times larger area.

The ICF Quarterly Report is published four times each fiscal year by the Inertial Confinement Fusion (ICF) Program at the Lawrence Livermore National Laboratory. The journal reports selected current research within the ICF Program. Major areas of investigation presented here include fusion target theory and design, target fabrication, target experiments, and laser and optical science and technology. In addition, the Laser Science and Technology program element of LLNL's Laser Programs serves as a source of expertise in developing laser and electro-optics capabilities in support of the ICF mission and goals and also develops new lasers for government and commercial applications. To keep our readers informed of these new capabilities, the *ICF Quarterly Report* now covers additional non-ICF funded, but related, laser research and development and associated applications. We also include summaries of the quarterly activities within Nova laser operations and the NIF Project. Questions and comments relating to the technical content of the journal should be addressed to ICF/NIF and HEDES Program, Lawrence Livermore National Laboratory, P.O. Box 808, L-475, Livermore, CA 94551.

On the Web:

<http://lasers.llnl.gov/lasers/pubs/icfq.html>

This document was prepared as an account of work sponsored by an agency of the United States Government. Neither the United States Government nor the University of California nor any of their employees makes any warranty, express or implied, or assumes any legal liability or responsibility for the accuracy, completeness, or usefulness of any information, apparatus, product, or process disclosed, or represents that its use would not infringe privately owned rights. Reference herein to any specific commercial product, process, or service by trade name, trademark, manufacturer, or otherwise, does not necessarily constitute or imply its endorsement, recommendation, or favoring by the United States Government or the University of California. The views and opinions of authors expressed herein do not necessarily state or reflect those of the United States Government or the University of California and shall not be used for advertising or product endorsement purposes.

UCRL-LR-105821-99-3

April-June 1999

Printed in the United States of America

Available from

National Technical Information Service

U.S. Department of Commerce

5285 Port Royal Road

Springfield, Virginia 22161

Price codes: printed copy A03, microfiche A01.

This work was performed under the auspices of the U.S. Department of Energy by University of California Lawrence Livermore National Laboratory under Contract No. W-7405-Eng-48.

INERTIAL CONFINEMENT FUSION

ICF Quarterly Report

April–June 1999, Volume 9, Number 3

In this issue:

Foreword iii

Control of Debris and Shrapnel Generation in the National Ignition Facility (*D. C. Eder*) 213

Limits are discussed for the amount of mass that can become debris and shrapnel associated with NIF target/diagnostic configurations. We show that the velocity of the shrapnel fragments is critical in determining the limits on material becoming shrapnel. Directing debris and shrapnel away from the 192 debris shields is discussed as a way to relax the mass limit.

X-Ray Backlighting for the National Ignition Facility (*O. L. Landen*) 227

X-ray backlighting will continue to be an important tool for the National Ignition Facility (NIF) for diagnosing a wide variety of inertial confinement fusion and high-energy-density physics experiments. We describe recent developments in backlighting techniques that provide the 100× improvements in backlighting efficiency and better data quality that will be required or desirable at NIF scale.

Using Intense Lasers in the Laboratory to Model Astrophysical Phenomena (*B. A. Remington*) 239

Before the development of intense lasers, scientists could only observe astrophysical phenomena in large observatories, and then explained their observations with theoretical models. They did not have the ability to quantitatively test the theories and models in an experimental setting where the initial and final states are well characterized. Now intense lasers that produce very high energy densities are being used to re-create aspects of astrophysical phenomena in the laboratory. Results from these experiments will help in the understanding of phenomena such as supernovae, supernova remnants, gamma-ray bursts, and giant planets.

Radiation Transport Experiments on the OMEGA Laser (*C. A. Back*) 255

Diffusive supersonic radiation transport, where the ratio of the diffusive radiation front velocity to the material sound speed > 2 , has been studied in a series of experiments on low-density foams. This article discusses spatially and temporally resolved measurements of samples that are up to 4 mean free paths long.

A New Laser-Driven Source for Studying Radiation Hydrodynamic Phenomena (*J. Edwards*) 263

A new laser driver is being developed for a variety of radiation hydrodynamics studies. This article describes application to turbulent, classical Rayleigh–Taylor instability.

Scientific Editors

Jeffrey Colvin
Brian MacGowan

Publication Editor

Jason Carpenter

Designer

Pamela Davis

Technical Editors

Jason Carpenter
Kimberly Herrmann
Al Miguel

Classification Editor

Roy Johnson

Art Staff

Sandy Lynn

Cover Design

Kathy McCullough

Nova Update	A-1
NIF Update	B-1
Publications and Presentations	C-1

FOREWORD

This issue has articles from a diverse range of subjects pertaining to execution of experiments on the National Ignition Facility (NIF). The first article looks at the issue of operability of the NIF target chamber from the perspective of emissions of target debris and shrapnel. Damage to chamber optics by such target emissions directly or through seeding of laser damage is likely to be a major driver for NIF operating costs. It is essential that we are able to minimize the impact of such debris. This article reviews our current understanding of target-generated debris and shrapnel and recommends limits on total target and shrapnel mass for NIF target designs.

The second article reviews experiment designs and diagnostic techniques that can be used for x-ray radiography in laser-plasma experiments. Techniques that have been used successfully at Nova and other laser facilities are described, and the problems with scaling them to the much-higher-energy plasmas of NIF are discussed. These problems include greater stand-off of diagnostics at NIF as well as higher energy requirements in the beams used to heat the backlighting plasma. Alternate diagnostic techniques that are applicable to NIF are described along with the results of tests at OMEGA.

The third article is a review of the application of large laser facilities such as NIF to the field of laboratory astrophysics. In past experiments at Nova and ongoing work at OMEGA and other facilities, intense lasers are being used to re-create aspects of astrophysical phenomena in the laboratory, allowing the creation of experimental testbeds where theory and modeling can be quantitatively compared with data.

The final two articles review experiments conducted on the OMEGA and Nova laser facilities to study the characteristics and applications of supersonic radiation wave transport in low-density foams. In ongoing OMEGA experiments, studies of supersonic radiation transport over several radiation mean free paths are beginning to enhance significantly our understanding of the details of how radiation and matter interact with one another in contexts relevant both to inertial confinement fusion (ICF) and to other applications. The first of these two articles describes these experiments. The second one describes the application of such radiative heating techniques to development of a “piston” for shocklessly accelerating materials. This new experimental technique, first developed on Nova, shows promise as a way to diagnose the development of acceleration-driven hydrodynamic instabilities in the compressible regime, a longstanding ICF problem that is currently only poorly understood.

Brian J. MacGowan and Jeffrey D. Colvin
Scientific Editors

CONTROL OF DEBRIS AND SHRAPNEL GENERATION IN THE NATIONAL IGNITION FACILITY

D. C. Eder

F. Serduke

M. T. Tobin

*R. E. Tokheim**

B. J. MacGowan

*D. R. Curran**

M. Gerassimenko

*L. Seaman**

The National Ignition Facility (NIF) will have a wide range of target and diagnostic configurations to support the large variety of its planned users. The interaction of the focused laser beam, unconverted light, x rays, and neutrons with the target and diagnostic structures will produce shrapnel and debris. Managing these contributions will be a critical part of controlling the operating costs of NIF.

The NIF components affected the most by debris and shrapnel are the 192 debris shields that protect the final optics assemblies. There are major cost and time constraints on how often these shields can be cleaned, refinished, or replaced. Diagnostics, target positioners, and other objects in the NIF chamber can also be severely affected by debris and shrapnel.

The first step in managing debris and shrapnel generation is to reduce the amount of material near target center. The second step is to control the type of material near target center, e.g., Pb-doped plastic shields as compared to solid metal shields, to reduce the consequences of debris and shrapnel generation. The third step is to control the composition (size and velocity) of the debris and shrapnel to mitigate its negative impact. The fourth step is to attempt to direct the debris and shrapnel to areas of the chamber where the impact is the smallest.

This article first describes the consequences of debris and shrapnel on debris

shields and the important difference in shrapnel velocities between the Nova laser at Lawrence Livermore National Laboratory (LLNL) and NIF (to begin partial operation in 2003). Next, we describe recent data taken on Nova that relates debris accumulation to reduced transmission through debris shields. Using this data, we discuss general NIF-specific requirements on debris and shrapnel. We obtain a rough debris mass limit of 400 mg/shot associated with material coming from the target/diagnostic configuration and the first wall. Next, we describe a simple model that is useful for understanding the effect of shrapnel size and velocity on damage. We obtain limits on the mass that can become shrapnel that depends on the size and velocity of the shrapnel fragments. For fragments moving at 1000 m/s with an average radius of 5 μm , the shrapnel mass limit per shot is of order 5 mg. Finally, we describe more detailed calculations to show the possibility of directing shrapnel and the effect of shrapnel impacting on materials.

Debris and Shrapnel Issues

Basic Definitions

Debris is vaporized material (including plasma) that rapidly expands outward from target center, with condensation possible prior to impact on chamber surfaces. Sources of debris include hohlraums, outer layers of shields, and other material heated

* Poulter Laboratory, SRI International

above their vaporization temperatures. *Shrapnel* is solid or melted (droplets of) material with sufficient velocity to damage exposed surfaces as a result of its impact. Sources of shrapnel are diagnostic shields, pinholes arrays, target support structures, and other objects close enough to target center to be melted or shocked with resulting small fragments that can be accelerated.¹ Debris and shrapnel can interact, e.g., the expanding debris can accelerate the shrapnel and alter its direction. This interaction can be a useful means to direct shrapnel to portions of the chamber wall away from the optics.

Consequences

The consequences of debris impacting on debris shields are twofold. First, debris on the surface of the shields will reduce the transmission of laser light. (The amount of the reduction depends strongly on the state of the debris, e.g., particle size.) Second, the debris on the surface reduces the laser-damage threshold of the debris shield. Laser damage of the debris shield results in additional transmission reduction. While the majority of the debris can be removed during the cleaning/recoating process, laser damage sites remain. There can be a major cost benefit of removing a debris shield prior to the onset of significant laser damage. The probability of laser damage depends on both the laser fluence and the debris accumulation. The removal of a given NIF debris shield for cleaning and/or refinishing will be determined by the amount of debris on the shield and the laser powers of the upcoming shots.

The consequences of shrapnel hitting the debris shields are also twofold, but they occur over a longer time frame. First, fracture craters formed during shrapnel impact can refract and diffract the laser light and thus reduce the amount of energy reaching target center. Second, the presence of these fracture craters, as shown in Figure 1, reduces the laser-damage threshold. A fracture crater is defined by the region in the debris shield where there are a large number of fractures (cracks) radiating out from the

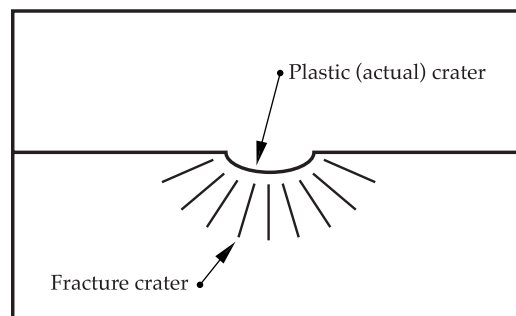


FIGURE 1. Sketch of a fracture crater in fused silica. The plastic region of a crater in brittle material is a small portion of the larger crater. (50-00-0899-1572pb01)

plastic (actual) crater where the fused silica has been removed. Because the debris shields are made of brittle fused silica, the size of the fracture crater is approximately an order of magnitude larger than the size of the plastic crater. To control costs, we must force the accumulation of fracture craters to occur over a longer time period than debris accumulation because removal of fracture craters requires refinishing or replacement of debris shields, which is significantly more expensive than cleaning. Only relatively shallow fracture craters (<10% of the shield thickness) can be removed by refinishing. In addition to being hard to remove, large fracture craters are more likely to trigger laser damage, which can create damage sites on the laser side of the debris shield that are significantly larger than the initial fracture crater.

Shrapnel Differences between Nova and NIF

The most important change in going from Nova experiments to NIF is the predicted higher velocities of the shrapnel fragments. Given NIF's 100× larger laser energy and given that the kinetic energy of a fragment is proportional to the velocity squared, one might expect shrapnel velocities a factor of 10 times larger. Detailed simulations of Nova and NIF experiments also show that the velocity of NIF fragments are a factor of 10 (or more) higher than Nova fragments. (In the final section, we discuss one detailed NIF simulation in the context of directing

shrapnel.) For example, a simulation of a Nova hohlraum with Cu shine shields had an average fragment size of 35 μm and an average velocity of 100 m/s; in contrast, a simulation of a no-yield NIF hohlraum with Cu shine shields had fragments a factor of 10 larger and velocities a factor of 10 to 100 times larger.² In fact, this simulation has shown that such shine shields are unacceptable on NIF because of very large shrapnel-related damage. To solve this problem, Pb-doped plastic shine shields are being planned for NIF.

Another NIF simulation of a target using stainless-steel cryogenic cooling tubes² had droplets with diameters of 5 to 25 μm moving at 1000 m/s. The tube material moving at this velocity was originally 1 cm from target center. As discussed later in this article, going from a velocity of 100 m/s (Nova) to 1000 m/s (NIF) can decrease the allowed shrapnel material by more than two orders of magnitude. Note that it is possible to have lower velocities on NIF if the material becoming shrapnel is further away from target center. For example, the same simulation of stainless-steel cryogenic cooling tubes had solid fragments with diameters of 40 to 400 μm moving at 300 m/s for parts of the tubes located 3 cm away from target center.

Shrapnel fragments traveling the larger distance (7 m vs 2.4 m) to the debris shields on NIF as compared to Nova do not slow down. Thus the higher velocities for NIF fragments still exist when the fragments strike the debris shields. However, the larger distance does decrease the number of fragments hitting a given area by approximately a factor of 10 for a constant number of fragments leaving chamber center.

Recent Measurements of Debris on Nova

Mass and Transmission Data on Debris Shields

The reduction in light transmission through debris shields as a result of debris accumulation is being studied on Nova using data taken during its last months of

operation. The normal period for cleaning/recoating of debris shields on Nova was every two weeks, and the period for refinishing/replacement was approximately every six to nine months. During the first two weeks of March 1999, we put in two new debris shields and repeated this with two new shields for a number of additional two-week periods. The initial transmission of the March debris shields was a little over 99%. After two weeks (~35 shots), the two shields were removed, and the transmission was measured. Figure 2 shows results of the transmission measurement for one of the two shields. The regions of reduced transmission, where the beam is blocked, are clearly seen. The reason for the higher “in-the-beam” transmission is due to laser cleaning, where the laser heats material on the surface causing it to be ejected. For this debris shield, the transmission for regions outside of the beam is approximately 93%, a drop of about 6% from the initial value. In contrast, the in-the-beam transmission is about 97%, only a 2% drop.

To measure the amount of debris accumulation, acid wipes were taken on different regions of the debris shields, including regions in and out of the laser beam. A chemical analysis of the removed debris was made allowing for an estimate of the mass per unit area of the different materials found on the shield. For the debris shield

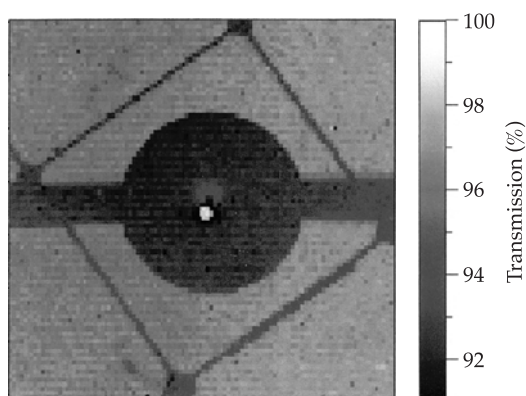


FIGURE 2. The transmission through the center portion (32 cm by 32 cm) of a Nova debris shield after being in chamber for two weeks of shots. Laser cleaning accounts for the clearing seen. (50-00-0899-1573pb01)

shown in Figure 2, the total mass for regions out of the beam was measured to be approximately $0.7 \mu\text{g}/\text{cm}^2$, with Au contributing about two-thirds of the total mass. The other major contributors were Cu and Al, with about another dozen elements contributing smaller amounts. A simple model that uses the actual target/diagnostic configurations for each of the shots during the two-week period gives very similar results for the total mass and the relative contributions of the different elements. The majority of the Au comes from vaporized hohlraums, with the Cu and Al coming from shields and supports. The mass for regions in the beam was measured to be approximately 0.4 times the mass measured for regions where laser cleaning was not taking place.

There were some fracture craters observed on the debris shield shown in Figure 2. Given that the shield was in for only a fraction (two weeks out of six months) of the normal operation lifetime and that the reduction due to shrapnel-induced fracture craters over six months is only a few percent, the contribution to loss of transmission for the shield in this study must be due primarily to debris accumulation and reduction in the effectiveness of the antireflective coating.

The combination of the transmission measurements and the mass measured using wipes shows that a mass of $0.7 \mu\text{g}/\text{cm}^2$ results in a loss of transmission of approximately 6%. Laser cleaning reduces this drop to about 2% because some of the deposited debris is removed, as well as some of the C-based deposits that affect the antireflection coating. These numbers give an approximate size of the debris particles on the surface. (For a given mass of material, smaller particles block the laser light more effectively because they have a larger cross section compared to their volume than larger particles.) If the debris particles are spherical with an average diameter of 20 nm ($0.02 \mu\text{m}$), one obtains a 6% drop in transmission for $\sim 2 \times 10^{10}$ particles/ cm^2 . Assuming a density of $10 \text{ g}/\text{cm}^3$, this number of particles gives the measured mass of $0.7 \mu\text{g}/\text{cm}^2$. Some of the drop in transmission is likely due to a reduction in the effectiveness of the antireflection coating. This would allow for a larger average size of debris particles.

Aerogel Samples

Aerogel, which is sometimes called “solid smoke,” is a very low-density material that can be used to capture debris and shrapnel. This quality of aerogel is useful for NASA in knowing the space-debris deposition that the orbiters (space shuttles) experience during missions. NASA needs to determine the space-debris deposition to ensure protection of the orbiter windows, which are made of fused silica. Aerogel samples are taken up with each orbiter flight and exposed to space debris. Upon the orbiter’s return, Hypervelocity Impact Technology Facility (HITF) staff at Johnson Space Center analyze this debris to determine what impacted the orbiter during its mission.

This same technique was recently applied to Nova shots to diagnose its shrapnel and debris. NASA provided LLNL four aerogel samples, three small ones ($2 \times 2 \times 1 \text{ cm}^3$, $20 \text{ mg}/\text{cm}^3$) and one large one ($4 \times 4 \times 2.5 \text{ cm}$, $40 \text{ mg}/\text{cm}^3$). All samples have been placed in the Nova chamber for one week at a time at two different locations: the three small ones in port Theta 155, Phi 72, and the large one in port Theta 25, Phi 252. The first of these samples has been partially analyzed using a scanning electron microscope and energy-dispersive x-ray analyses.³ The analysts have forwarded annotated pictures with their early results, one of which is shown in Figure 3. Examples of particle sizes and track lengths in the aerogel are a $130\text{-}\mu\text{m}$ particle with a 1.1-mm-long track, a $19\text{-}\mu\text{m}$ particle with a 2.12-mm-long track, and a $34\text{-}\mu\text{m}$ particle with a 2.05-mm-long track.

NASA will be able to describe the specific velocities that the particles achieved because they have calibrated the response of aerogels to shrapnel. An advantage of aerogel over higher-density foams (e.g., polyethylene targets discussed in the subsection “Penetration of Shrapnel Fragments”) is that slower-velocity fragments can be tracked.

NASA is in the process of finishing a report of their analyses of this first sample of aerogel. The remaining three samples will also be analyzed by NASA.

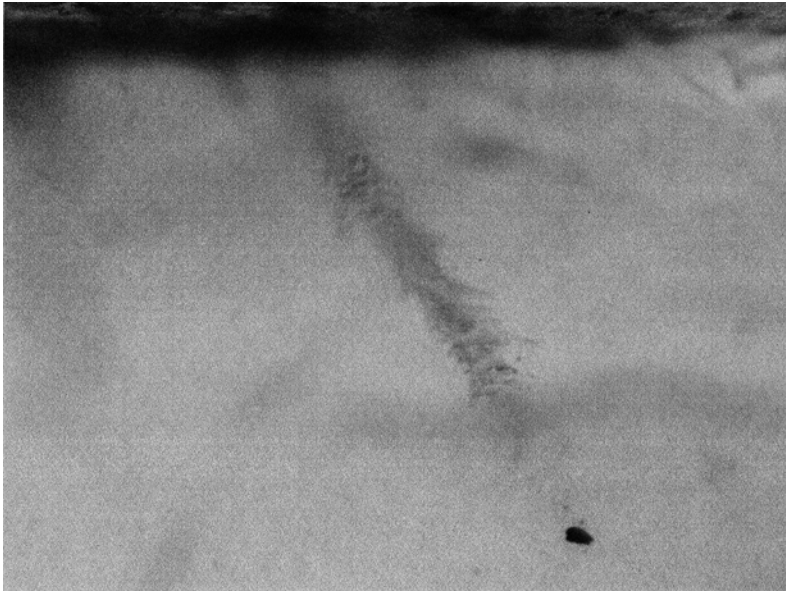


FIGURE 3. Photo of a fragment and its track as it passes through an aerogel sample.
(50-00-0899-1574pb01)

NIF-Specific Debris and Shrapnel Issues

Removal of Debris Shields

The determination of when a given debris shield must be removed from the NIF chamber depends on the level of debris and fracture-crater accumulation and on the requirements of the shots that follow. It is expected that the spatial distribution of debris and shrapnel will not be isotropic. This means that some debris shields will accumulate debris and fracture craters faster and will have to be removed more often. It is very important that the status of each debris shield be known through modeling supported by direct measurement, such as witness plates that are sampled periodically. This was not considered necessary on Nova, where half of the debris shields (5 out of 10) were removed every week for cleaning and recoating independent of their current condition. The two-week removal period for each shield came from many years of measuring the transmission of the removed shields. For the 192 debris shields on NIF, it will be cost- and time-effective to remove only the debris shields that need to be removed, according to three basic criteria:

1. Is the reduction in total energy reaching target center too large?
2. Is the level of power balance adequate?
3. Will significant laser damage occur?

If only a few shields have significant accumulation, the total energy reaching target center may not be reduced very much. However, the loss in transmitted energy through the “dirty” shields may not be acceptable because of power balance requirements. The last criterion is mainly a cost-control issue. There can be a major cost benefit of removing a debris shield for cleaning/recoating before there is significant laser-induced damage to the shield because of the reduced damage threshold. Laser damage is not removed by cleaning and can result in replacement of the debris shield earlier than needed.

Similar criteria determine when a debris shield should be refinished. In particular, it can be cost-effective to refinish a debris shield before the level of fracture-crater accumulation leads to major laser-induced damage. It is expected that a shield can be refinished at least once by removing up to approximately 1 mm from the 1-cm-thick shield. This would remove all fracture craters with depths less than 1 mm and reduce the area of deeper craters. Laser-induced damage sites can occur on the side

of the debris shield away from target center, making it necessary to refinish both sides to remove these sites. A debris shield can be refinished more than once provided that the total removal thickness does not exceed 1 mm. As for the case of deep fracture craters, deep laser-induced damage sites cannot be removed by refinishing. Because of the large number of debris shields on NIF, it is critical to keep the refinishing and replacement rate at acceptable levels, e.g., a full set refinished and a full set replaced per year. Cleaning and recoating a full set more frequently than once per week would also be a major cost and time issue. Given that the accumulation is not expected to be uniform, the cleaning/recoating, refinishing, and replacement rates could be larger for some shields than the weekly and semiannual numbers.

Allowed Mass of Debris

The amount of debris allowable on debris shields depends strongly on the state of the debris, i.e., a thin film vs small particles. The measurements of transmission and debris mass on the Nova debris shields indicate that the debris is in the form of small particles with diameters of order 20 nm or larger depending on loss of antireflective coating. For the purpose of the estimates given in this article, we assume that the form of the debris on the NIF shields will be similar to Nova. However, this is an issue that merits additional investigation.

Another uncertainty on NIF is what mass or reduction in transmission will be acceptable. As discussed in the previous subsection, removal of NIF shields depends on the requirements of the following shots. In order to get an estimate of the allowed mass for NIF, we take $1 \mu\text{g}/\text{cm}^2$ as a reasonable number. If one assumes similar laser cleaning as Nova, this gives an expected transmission of $\sim 3\%$. (The factor of $\sim 5\times$ higher laser fluences through NIF shields, as compared to Nova, could make laser cleaning more effective, but could also drop the allowed mass because of laser-damage issues.)

If the deposition of mass is uniform and isotropic, a mass per unit area of $1 \mu\text{g}/\text{cm}^2$ at the NIF debris-shield radius of 7 m corresponds to a total mass of approximately

6 g. For a shot rate of 15 shots per week, this corresponds to 0.4 g or 400 mg per shot. It is expected, however, that the deposition of mass will not be isotropic. If this is the case and if 400 mg is deposited each shot, some debris shields will have to be cleaned and recoated more often than once a week. The vaporized target is not the only source that must be considered in the 400 mg/shot limit. Surface layers of shields, diagnostic components, target positioners, etc., can be vaporized by unconverted laser light or by x rays from the target. Given the large surface area of the first wall, even a very small layer of x-ray vaporization on the wall can contribute significant mass.

Various first-wall materials were considered for NIF, including stainless steel and B_4C . The major advantage of B_4C is a reduced x-ray ablation rate. However, the first wall is relatively quickly coated with debris from vaporized targets, and this advantage is lost with time. This effect combined with cost considerations results in stainless steel being chosen as the first-wall material. To control the amount of vaporized wall material getting back into the chamber, louvers were developed for the first wall that trap approximately 90% of the ejected material.⁴ At this time, we budget approximately one-half of the 400 mg/shot to come from vaporized wall material that escapes the louvers, and we budget the remaining 200 mg/shot to come from the target and structures close to target center.

It is expected that high-yield (20-MJ) shots will exceed these mass limits because of more massive targets and higher x-ray fluxes giving more wall ablation. The planned shot rate for these high-yield shots is only 50 per year, and it is not unreasonable to consider removal of a full set of debris shields for cleaning/recoating following each of these shots. It is possible that high-yield shots may also require new debris shields prior to the shot to ensure that the total power and beam balance requirements can be satisfied.

Limits on Shrapnel

The most expensive NIF hardware in the path of shrapnel coming from target center are the final optics assemblies

(FOAs), which are protected by 1-cm-thick fused-silica debris shields. We consider three levels of damage to these debris shields.

The first level is damage caused by shrapnel fragments with sufficient mass and velocity (e.g., 2-mm-diam Cu sphere moving at 10 km/s) to break through a shield. This would require immediate replacement of the debris shield plus possible effects on other components in the corresponding FOA. A reasonable limit on first-level damage is penetration through one of the 192 debris shields per month, or once per 16 years for a given debris shield.

The second level of damage is associated with fracture craters whose depths exceed approximately one-fourth the thickness of the debris shields. (Based on formulas given in the next section, a Cu sphere with a diameter of 250 μm moving at 1000 m/s would produce such a fracture crater.) Such large fracture craters are not removed by refinishing, and they are likely sites for inducing laser damage. A reasonable limit for these large fracture craters is 50 in a six-month period, or 100 per year for a given debris shield. (This limit is associated with laser-induced damage and merits future investigation.)

The third level of damage is associated with fracture craters whose depths do not exceed approximately one-fourth the thickness of the debris shields. Most of these fracture craters can be removed during refinishing, and their major impact is a loss of energy reaching target center because of scattering and a reduction in the laser-damage threshold. The larger fracture craters are the most likely to trigger laser-induced damage. The debris shields on Nova are refinished or replaced when the reduction in transmission associated with fracture craters and corresponding laser damage sites exceed 5%. In determining how much mass can become shrapnel on NIF, we take as a reasonable requirement that the surface area of fracture craters not exceed 2% of the debris shield. Unlike debris, this requirement does not translate directly into allowed shrapnel mass even if a fragment size is assumed. This is because the size of a fracture crater depends on the size and velocity of the shrapnel fragment.

In the next section, we use a simple model to show the effect of changing fragment sizes and velocities on the allowed mass that can become shrapnel.

Model for Shrapnel-Induced Fracture Craters

Modeling of Fracture Craters

The size of fracture craters depends on the size, density, and velocity of the incoming shrapnel fragments. When an initially solid piece of material becomes shrapnel, the size of the fragments (solid and liquid) depends on the thermal and mechanical stress imposed on the piece. In general, fragments will be produced with a range of sizes and velocities. There is direct experimental evidence⁵ and indirect evidence from modeling² that the fragment size distribution is approximately that of a Poisson distribution

$$N(R) = N_{\text{tot}} \exp(-R/R_1), \quad (1)$$

where N_{tot} is the total number of fragments, N is the number with radii greater than R , and R_1 is the average radius of the fragments. If the total mass of shrapnel is M_{tot} , the total number of fragments is

$$N_{\text{tot}} = \left[\frac{M_{\text{tot}}}{(8\pi\rho R_1^3)} \right], \quad (2)$$

where ρ is the density of the fragments. In the model discussed in this section, we assume that the fragments are specified by a Poisson distribution with an average radius R_1 and a uniform velocity. This model agrees well with more detailed simulations, where the velocities of the fragments are approximately the same as the material that broke up into fragments. There can be situations where significant acceleration occurs after breakup with smaller fragments reaching larger velocities.

Given sizes and velocities of fragments, we wish to determine the sizes of the corresponding fracture craters. Experiments have been conducted with metal spheres of various sizes and velocities impacting on fused silica.^{2,6} An empirical formula has been developed that fits this data:²

$$D_s/L = \beta(\alpha\rho v^2/Y)^{1/3}, \quad (3)$$

where $\alpha = \text{Min}[0.1\rho v^2/Y, 1]$, D_s is the depth of the fracture crater, L is the diameter of the sphere, β is the ratio of the fracture crater to the plastic crater ($\beta = 10$ for fused silica), ρ is the density of the sphere, and Y is the dynamic compressive yield strength ($Y = 1$ GPa for fused silica). As an example, a 25- μm -diam fragment having a velocity of 10 km/s and a density of 8 g/cm³ will produce a fracture crater having a depth of 0.25 cm and a diameter of 0.5 cm. The assumption that the width is approximately twice the depth has been confirmed by measurements.²

Allowed Mass That Can Become Shrapnel

In the subsection “Limits on Shrapnel,” we discussed three levels of damage associated with shrapnel and corresponding requirements. We use the expressions given above to translate these requirements to limits on the amount of mass that can become shrapnel. These limits depend on the average size of the fragments and their velocity.

The first requirement is that no more than one of the 192 debris shields be penetrated by a shrapnel fragment per month. In Figure 4, we give the number of penetrations per month for each gram of material that becomes shrapnel fragments. We give results as a function of fragment velocity for two values of the average radius R_1 . This calculation assumes 600 shots per year, and the number plotted per month is for the whole facility, i.e., all 192 debris shields. All of our calculations for shrapnel limits use a density of 8 g/cm³. If the velocity is of order 1000 m/s, even relatively large fragments with average sizes in the 100- μm range are

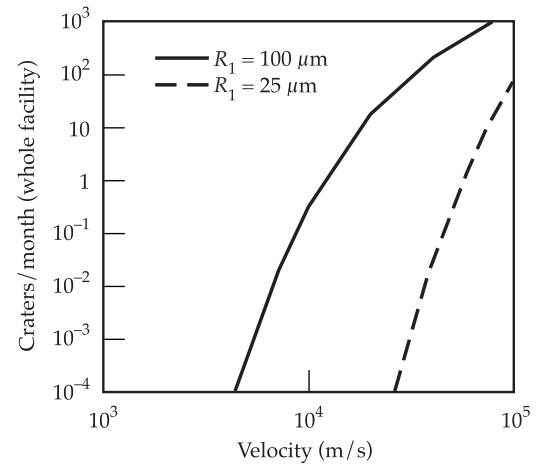


FIGURE 4. The number of NIF debris-shield penetrations in the facility per month per gram per shot of shrapnel material. Curves are for fragment distributions having average radii of 25 and 100 μm . (50-00-0899-1575pb01)

not a problem. If the velocity is 10 km/s, then a fragment with a radius of 1 mm (1000 μm) can penetrate a shield. If the average radius of the distribution is 100 μm (top curve in Figure 4), there exist fragments with radii a factor of 10 or more larger than the average. These are the fragments that are contributing to the penetrations per month shown in the graph. The rapid increase with velocity occurs because the fragments that can penetrate are in the tail of the Poisson distribution. An increase in velocity means that smaller fragments can contribute, and the number of these fragments increases exponentially with decreasing size. For a velocity of 10 km/s and an average radius of 100 μm , there are 0.33 penetrations per month per gram of material. This implies that up to 3 g of material is allowed to become this type of shrapnel to meet the requirement of only one penetration per month. Fragments with this velocity and sizes were calculated to arise from the NIF Cu-shine-shields calculation. Such shields are acceptable based on this requirement but are not acceptable based on the requirements discussed below. If the average size of the fragments is 25 μm or less, there is little chance of a penetration because shrapnel velocities significantly greater than 10 km/s are not likely.

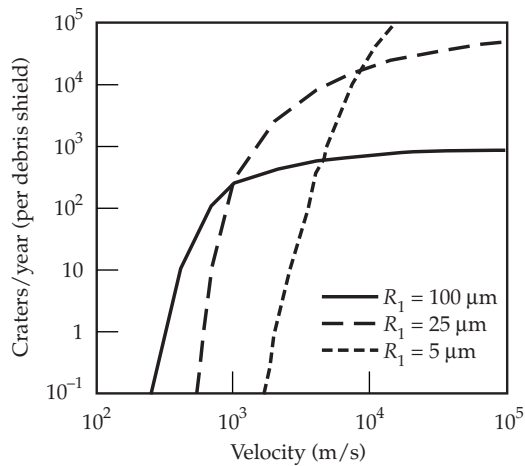


FIGURE 5. The number of fracture craters with depths that exceed 2.5 mm (one-fourth of the debris-shield thickness) per year per gram of shrapnel material. Curves are for fragment distributions having average radii of 5, 25, and 100 μm . (50-00-0899-1576pb01)

The second requirement is that the debris shields do not have a large number of fracture craters with depths that exceed one-fourth the thickness of the debris shield. In Figure 5, we give the number of such large fracture craters per year per debris shield. For size distributions with average radius of 25 and 100 μm , we see a rolloff in the number with increasing velocity. This occurs because a majority of the fragments in the distribution start to have sufficient energy to create such large fracture craters. The reason that the curve for $R_1 = 25 \mu\text{m}$ goes to larger numbers than the curve for $R_1 = 100 \mu\text{m}$ is that the curves are for a fixed mass (1 g) of material, and smaller-size distributions have larger numbers of fragments. For a velocity of 1000 m/s, the distributions with R_1 equal to 25 and 100 μm both have about 275 large fracture craters per year per gram. If 100 is the target number, the allowed mass becoming shrapnel is 360 mg for fragments moving at 1000 m/s with average radii between 25 and 100 μm . For a velocity of 10 km/s, masses of 3, 5, and 133 mg each give 100 large fracture craters for average fragment radii of 5, 25, and 100 μm , respectively.

The third requirement is that the surface area covered by shallow craters does not

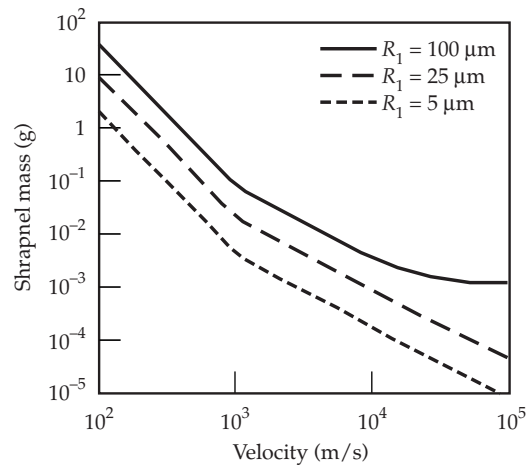


FIGURE 6. The shrapnel mass per shot that would produce fracture craters having a total surface area of 2% of the debris shield area after 300 shots. Mass as a function of fragment velocity is plotted for three fragment distributions having average radii of 5, 25, and 100 μm . (50-00-0899-1577pb01)

exceed 2% of the surface area of the debris shield during six months of operation. In Figure 6, we give allowed mass that can become shrapnel as a function of velocity for three size distributions. The calculation assumes 300 shots during the 6-month period and fragment density of 8 g/cm³. As for the other requirements discussed above, there is a rapid decrease in allowed mass as the velocity increases. For a velocity of 1000 m/s, the allowed masses are 5, 15, and 100 mg for average fragment radii of 5, 25, and 100 μm , respectively. For a Nova-type velocity of 100 m/s, the allowed masses are all over 2 g. If the shrapnel has a high velocity like 10 km/s, very little mass is allowed to become shrapnel. If a piece of shrapnel breaks into larger fragments, more mass is allowed for a given velocity. However, larger fragments produce deeper craters.

There is a distribution of fracture crater sizes at a given velocity because of the Poisson fragment size distribution. Thus the contribution to the total surface area of craters comes from a range of crater sizes. In Figure 7, we show this contribution for fragment distributions with average radii of 5, 25, and 100 μm and a velocity of 1000 m/s. This model also shows the effect of changing the average size of the shrapnel

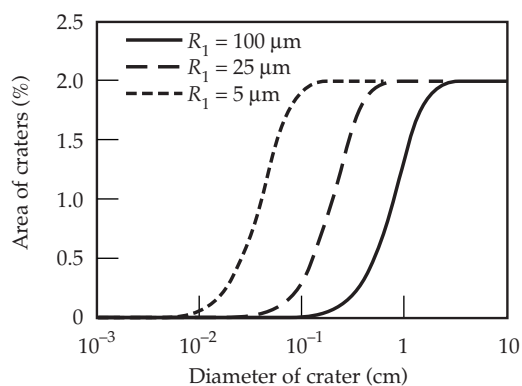


FIGURE 7. The contribution to the total surface area of craters from craters below a given diameter for fragment distributions having average radii of 5, 25, and 100 μm and a velocity of 1000 m/s. (50-00-0899-1578pb01)

fragment while holding the velocity constant. The allowed mass that can become shrapnel scales with size and is 5, 25, and 100 mg per shot for these average radii. While increasing the average radii from 5 to 25 μm increases the allowed mass by the same amount, the majority of surface area is from craters with depths greater than 10% of the shield thickness. Such craters would not be removed during a refinishing process. For an average radius of 100 μm , essentially all the fracture craters are too deep to be removed during refinishing. In addition, these larger fracture craters are more likely to induce laser damage of the debris shields.

We see from our simple model that the strongest limit on mass becoming shrapnel is associated with the third-level damage requirement associated with keeping the surface area of craters below 2% of the total. If we also require that the fracture craters be shallow, e.g., less than 10% of the shield thickness, the allowed shrapnel mass is only of order 5 mg per shot for a fragment velocity of 1000 m/s. Laser-induced damage can lower this limit further because existing crater sites can grow in size. It is desired to have structures, e.g., pinhole arrays, whose mass will exceed 5 mg. One solution is to place the structure close enough to target center to be vaporized or far enough away that the velocity of the fragments is significantly below 1000 m/s. Another solution is to attempt to direct the shrapnel away from the debris shield. In the next section, we

discuss a simulation showing the feasibility of directing shrapnel away from shields.

Detailed Simulations of Shrapnel Damage

In this section, we discuss two detailed simulations of shrapnel damage. The first is for a cryogenic hohlraum NIF shot producing ignition and yield using sapphire cryogenic cooling rods, which shows that directing shrapnel by a debris wind is possible. The second is a simulation of a shrapnel fragment penetrating into polyethylene. These calculations are examples of detailed simulations that can be used to guide us in reducing damage associated with NIF shrapnel.

Directing Shrapnel Away from Debris Shields

There are some sources of shrapnel whose positions cannot be changed, i.e., they cannot be placed close enough to be vaporized or move far enough away to have slow velocities. One of these is cryogenic cooling tubes or rods that are essential for high-yield cryogenic targets. In the previous section, we gave some shrapnel size and velocity information for a NIF simulation using liquid-He-filled stainless-steel cryogenic cooling tubes.² This simulation predicts that tube shrapnel will cause excessive damage to approximately 20% of the debris shields in a single shot. A new cryogenic target was designed using sapphire cooling rods in place of stainless-steel tubes along with a number of other changes, including the location of cooling rings around the hohlraum. While the simulation we discuss here is for this design, there have been further changes in the design of the cryogenic target. Some of these changes will likely affect shrapnel generation and damage. We discuss this issue at the end of this subsection.

A cryogenic target design is shown in Figure 8. The two sapphire rods provide mechanical support for the hohlraum and carry heat away from the hohlraum to maintain its temperature near 18 Kelvin.

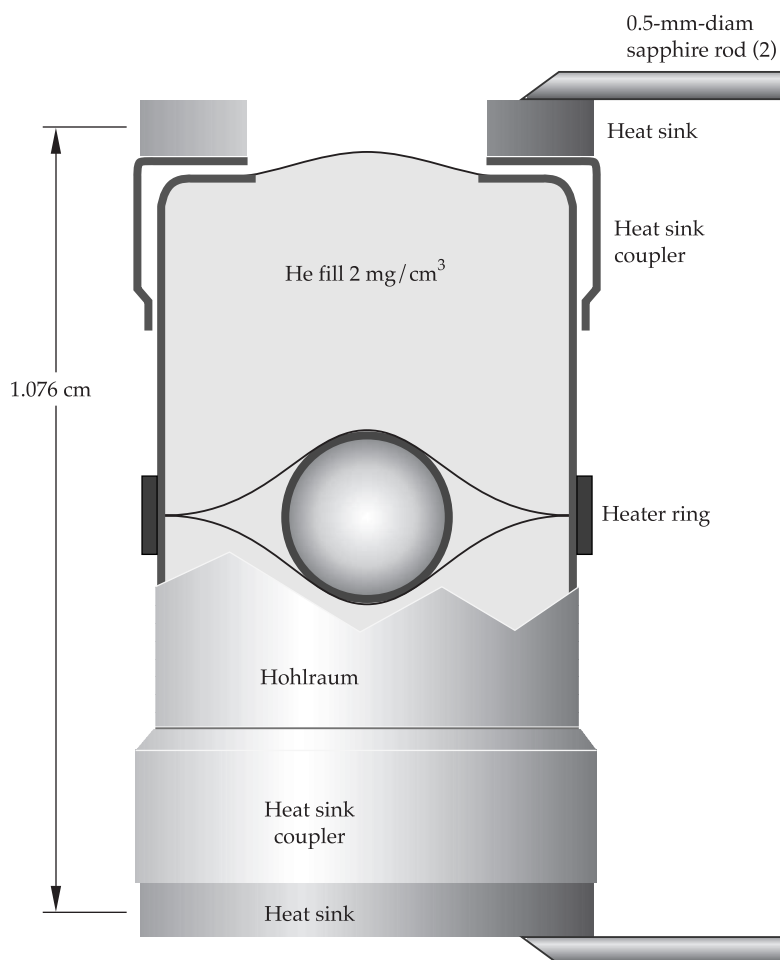


FIGURE 8. A design for a NIF cryogenic target using sapphire cooling rods.
(50-00-0899-1579pb01)

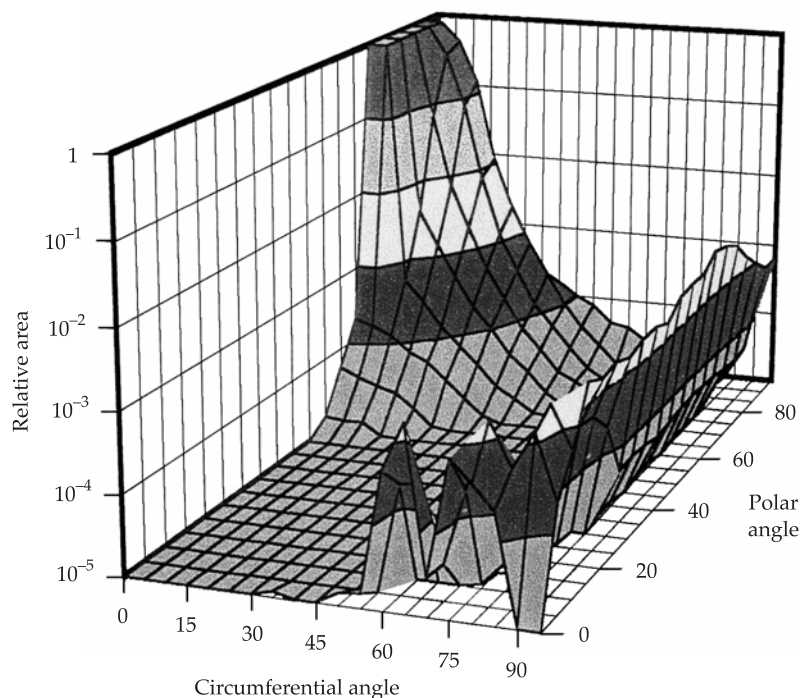
The 0.5-mm-diam rods are attached to two Si cooling rings that act as heat sinks. The wall of the hohlraum is 30- μm -thick Au with additional Au used for two 30- μm -thick heat-sink couplers and for the 50- μm -thick heater ring. The total mass of the target is approximately 300 mg.

The simulation is for a 20-MJ fusion yield, where the sapphire rods are radiated with neutrons and x rays and then struck by debris from the vaporized hohlraum. The neutron heating vaporizes the rods out to approximately 1 cm from the hohlraum axis, with the next 0.5 cm being melted. This sudden heating causes shock waves within the rods, which produce large radial velocities and subsequent fracture. In comparison to the stainless-steel cryogenic cooling tubes, the liquid droplets and solid fragments are relatively small in size, having diameters of 0.2 to 2 μm . The outward expansion of the rods is modified by the arrival of the x rays,

which act only on the surface facing the hohlraum. Then the debris wind catches the sapphire fragments and droplets and drags them along in the direction of the wind. The velocity of the material is very high; some 1- μm objects initially 1.5 cm from the axis move faster than 50 km/s. The fragments/droplets are tracked until they strike the chamber wall and produce fracture craters. This calculation has the majority of the fracture craters located near the waist of the chamber, i.e., polar angles greater than 65°. This is seen in Figure 9, where the relative area of fracture craters is plotted as a function circumferential and polar angles. The debris shields have polar angles of 23.5°, 30°, 46.5°, and 50° and thus are not significantly damaged in this calculation.

An important source of the debris wind responsible for pushing the rod material towards the waist of the chamber is associated with the Si cooling

FIGURE 9. The location of shrapnel damage from the sapphire cooling rods is plotted as a function of the circumferential and polar angles.
(50-00-0899-1580pb01)



rings/heat sinks. In this role, the location of the rings near the hohlraum entrance hole is important. Because of concerns of hole closure, the current cryogenic target design has these cooling rings located away from the entrance hole. It is expected that the confinement of shrapnel to the waist will not be as effective. Simulations are planned for the new design, and additional modification of the design will be done to control shrapnel damage.

Penetration of Shrapnel Fragments

When shrapnel fragments strike brittle, hard material, e.g., debris shields made of fused silica, they create fracture craters, and the fragment is vaporized or otherwise destroyed on impact. If shrapnel fragments impact soft, low-density material, the fragments can penetrate a significant depth into the material and remain relatively intact. This has already been discussed in this article in the con-

text of the aerogel samples that were placed in the Nova chamber. Another material that has been used to capture shrapnel fragments is polyethylene. In particular, there have been a number of experiments and simulations in France using polyethylene to understand shrapnel. Because the French are building the Laser Megajoule (LMJ) facility, they are also very interested in shrapnel. Some of their work we have already cited,⁵ where polyethylene was used to show that the size distribution of the fragments is approximated well by a Poisson distribution. Velocity of the fragments can also be determined by measuring the depth of penetration. To obtain the velocity, a relationship between depth and velocity must be determined experimentally or through modeling.

In Figure 10, we show results of French experiments, where 550- μ m stainless-steel spheres were impacted onto polyethylene at various velocities, and penetration depth was measured.⁷ There is also one data point for a 350- μ m sphere. The figure

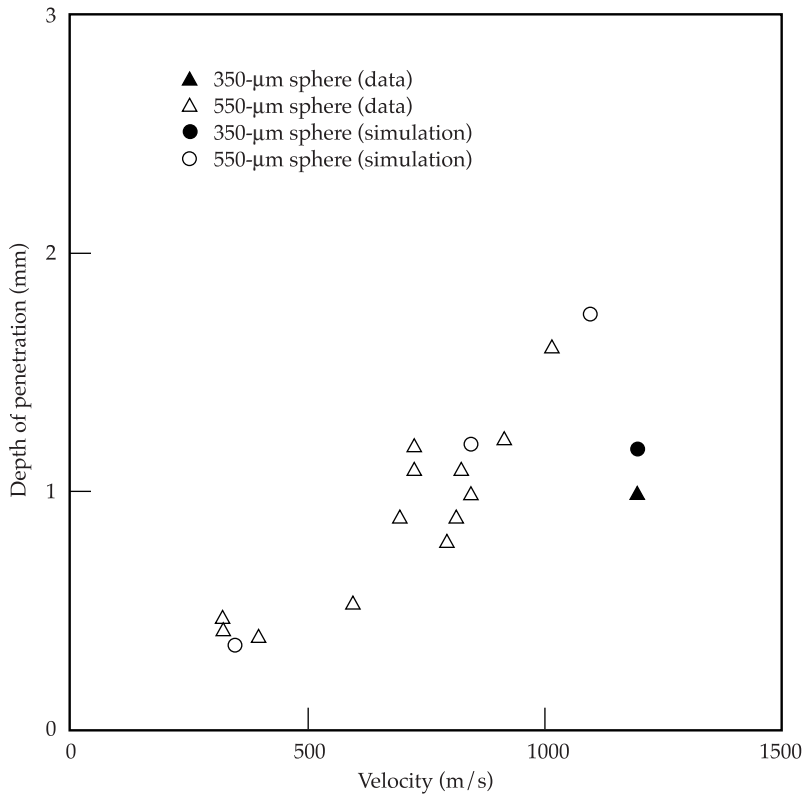


FIGURE 10. The measured depth of penetration of stainless-steel 350- μm and 550- μm spheres into polyethylene as a function of the velocity of the spheres. Results of LLNL calculations are shown to be in reasonable agreement with the data. (50-00-0899-1581pb01)

also includes simulations done at LLNL using the CALE code, which show quite good agreement with the data.⁸ Earlier simulations done in France gave comparable results, but when the stainless-steel spheres came to rest in the polyethylene, they were more distorted in the simulations than when observed.⁷ This was one of the motivations to do the LLNL simulations, and we show the results for simulation of a 550- μm sphere that impacted polyethylene with a velocity of 1100 m/s in Figure 11.⁸ The sphere has come to rest in the polyethylene at a depth of about 1.7 mm. The stainless-steel projectile remained nearly spherical. In contrast, the earlier simulations showed a projectile that became significantly distorted by the time it came to rest.

Simulations are planned for projectiles impacting fused silica. In particular, we plan to study issues that are hard to study experimentally. These include the impact of high-velocity liquid droplets and nonspherical objects.

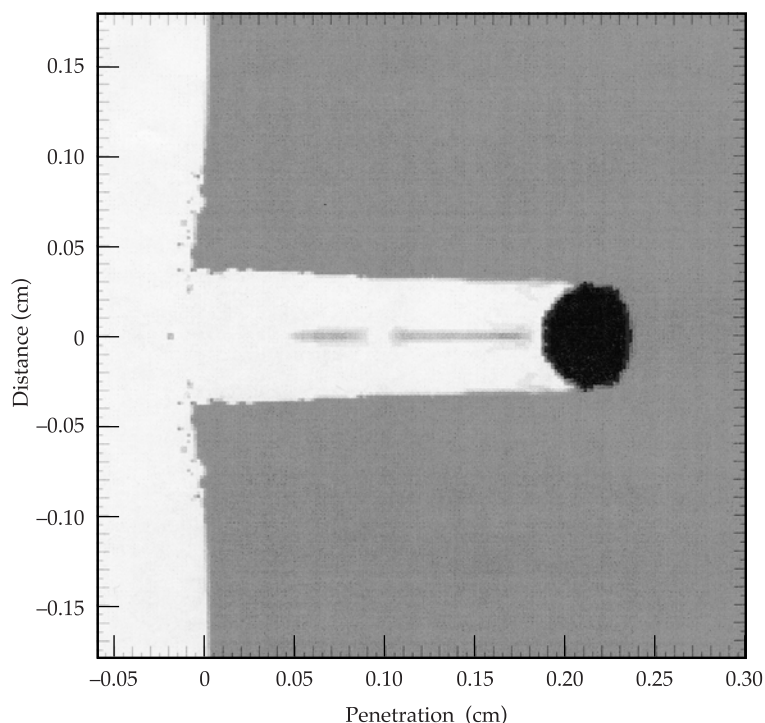
Conclusion

Recent measurements of debris accumulation and transmission on Nova debris shields have been helpful in setting limits on the amount of material that can become vaporized debris on NIF. This mass limit of 400 mg/shot is divided roughly equally between contributions from the first wall and from target/diagnostic configurations. This limit can be relaxed for a subset shots, e.g., high-yield shots, but must be used as a guide for all shots. The mass limit also assumes that NIF will have similar debris material and composition on its shields as measured on Nova and that the level of laser cleaning is comparable. An area that merits additional work is the limits imposed on debris accumulation associated with laser-induced damage given the higher laser fluences passing through the shields on NIF.

The requirements on mass that can become shrapnel are not as easy to define. We showed that the higher velocities expected for NIF, as compared to Nova,

FIGURE 11. The calculated shape of the stainless steel after coming to rest in the polyethylene is shown along with the track through the polyethylene.

(50-00-0899-1582pb01)



have a large impact on the allowed mass levels. If the velocity of the shrapnel fragments are of order 1000 m/s and if deep craters are not allowed, the allowed mass that can become shrapnel is only 5 mg/shot and must be in the form of particles having average sizes of order 5 μm . The 2% limit on transmission loss due to fracture craters does not allow for the increase in crater size due to laser-induced damage. This effect can reduce the allowed mass below the 5-mg limit presented here. Slower velocities are possible on NIF if the material that becomes shrapnel is placed some distance (3 to 10 cm) from target center. If it is possible to direct shrapnel away from the debris shields, as shown in the simulation using sapphire cooling rods, higher mass limits are possible.

Managing debris and shrapnel is an important part of controlling the operating costs of NIF. Continued analysis of existing data, such as the aerogel samples taken on Nova, and additional simulations will aid in our understanding of debris and shrapnel generation and their impact in the NIF chamber.

Notes and References

1. *High-Pressure Shock Compression of Solids II*, L. Davison, D. E. Grady, and M. Shahinpoor, Eds., Springer, NY (1996).
2. R. E. Tokheim, D. R. Curran, and L. Seaman, *Damage and Hardening Assessments for the National Ignition Facility Target Chamber Design*, Lawrence Livermore National Laboratory, UCRL-CR-128686 (1998).
3. E. Christenson and F. Bernhard, personal communication (1999).
4. A. K. Burnham et al., "Constraints on Target Chamber First Wall and Target Designs That Will Enable NIF Debris Shields to Survive," *Proceedings of Solid State Lasers for Application to Inertial Confinement Fusion Conference*, Monterey, CA (June 1998).
5. J. P. Thebauly, L. Bianchi, F. Jequier, and R. Courchinoux, *Shrapnel Experiments on PHEBUS*, in *Proceedings of LLNL/CEA Meeting*, Limeil-Valenton, France (September 1997).
6. K. S. Edelstein and M. L. Fudge, "Penetration and Surface Spalling due to Hypervelocity Impact into Fused Silica," personal communication (1995).
7. A. Geille, F. Jequier, and Y. Hermouet, "Simulation of Shrapnel Experiments," in *Proceedings of LLNL/CEA Meeting*, Limeil-Valenton, France (September 1997).
8. M. Gerassimenko and F. Serduke, *Modeling of Steel Spheres Impacting Polyethylene*, Lawrence Livermore National Laboratory, Livermore, CA, UCRL-ID-135763 (1999).

X-RAY BACKLIGHTING FOR THE NATIONAL IGNITION FACILITY

O. L. Landen L. M. Logory F. D. Lee C. A. Back
D. R. Farley P. M. Bell D. K. Bradley R. E. Turner
S. G. Glendinning J. A. Koch D. H. Kalantar

X-ray backlighting refers to the technique of radiographing transient phenomena in high-density materials. It is a powerful method of measuring hydrodynamic evolution of a material subject to external pressures, such as those created by x-ray¹⁻⁶ or laser ablation.⁷⁻⁹ When the backlighter is either monochromatic or spectrally resolved by the imaging instrument, information on the opacity or equation-of-state of a material can also be gleaned.¹⁰⁻¹⁹ Transient, picosecond- to nanosecond-duration x-ray backlighter sources emanate from plasmas created by the interaction of high-intensity laser beams with foils.²⁰⁻²⁹ Imaging is usually provided by one of three methods:

1. Pinholes³⁰⁻³⁶ (for 2D imaging) or slits^{4,35,37} (for 1D imaging) are placed between the backlit sample and detector.
2. A point source of x rays is created that casts a shadow of the sample at the detector.^{22,23,38-40}
3. X-ray optics such as curved mirrors^{35,41-44} and Fresnel lenses⁴⁵ cast a backlit image at the detector.

The intrinsic spatial resolution depends on a combination of the detector resolution and the pinhole diameter, point source size, or quality of the figure of the optic, respectively.^{30,35} The effective resolution, however, as limited by data noise, can be worse. Noise arises from insufficient photons collected per resolution element (shot noise), or spatial nonuniformities in the instrument response.

In the first section of this article, “Imaging Techniques” on p. 228, we review the strengths and weaknesses of the first two backlighting geometries, especially in the context of extrapolating to NIF scale. Because the third backlighting method, utilizing x-ray optics, is inherently expensive and calibration-intensive, it has not been able to accommodate the wide variety of high-energy-density and inertial confinement fusion (ICF) experiments demanding timely, quantitative backlighting at arbitrary photon energy. Hence, we will not further discuss this third option, but rather endeavor to show how improvements in the first two techniques can make them at least as valuable for the National Ignition Facility (NIF) as they have been at Nova and OMEGA. For example, we propose variants on these backlighting geometries that should improve the backlighter efficiency for some current experiments by factors of up to 100. Recent results from Nova and OMEGA with the new techniques are also presented as proof of principle.

In the second section, “Backlighter Sources” on p. 233, we discuss how the backlighter source efficiency can be increased by using spatially distributed, broader-bandwidth sources. Supporting results from Nova are also presented. In the third section, “Detectors” on p. 234, we discuss the choice of detector, particularly with respect to the data signal-to-noise ratio (SNR). We present recent results showing significant improvements in data SNR by switching from film to a charge-coupled device (CCD) as the final recording

medium and by correcting postshot for fixed pattern noise on framing camera data. We conclude by discussing the experiments we have planned at OMEGA for further validating these new backlighting concepts, which will be essential for NIF.

Imaging Techniques

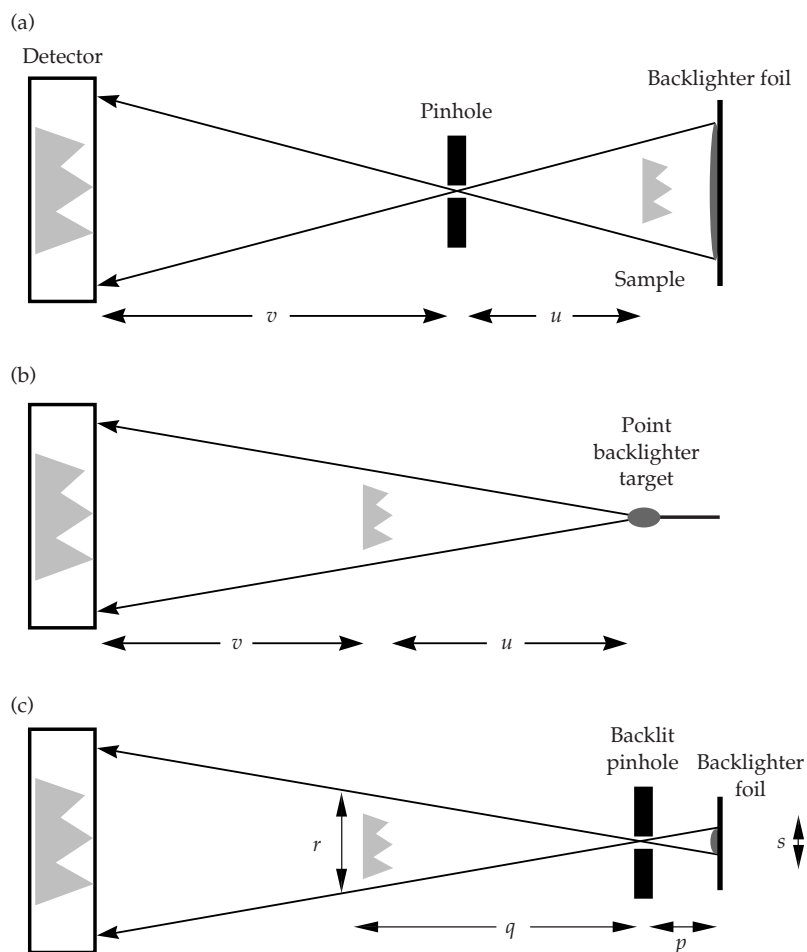
We first review the two standard imaging techniques utilizing backlighting sources commonly known as area backlighting and point-projection backlighting. We explain why current area backlighting is impractical at NIF scale, and why current point-projection backlighting has not and will not become a mainstay technique at any size facility. We then present a variant on the current point-projection technique, backlit

pinhole backlighting, which combines the best features of both traditional techniques while providing a potentially more efficient x-ray source for all future experiments. Methods for further increasing the photon-collection efficiency by using redundant imaging apertures are also discussed.

Area Backlighting

For area backlighting, imaging with magnification $M = v/u$ is provided by a pinhole or slit placed between the backlit sample and the detector, as shown in Figure 1a. The backlitter source size, by simple geometry, must be at least as large as the sample transverse dimensions. There are three principal advantages to this technique:

FIGURE 1. Schematic of backlighting configurations. (a) Area backlighting, (b) Point-projection backlighting using point targets, and (c) Point-projection backlighting using pinholes.
(08-00-0899-1590pb01)



1. The spatial resolution is determined by a fixed entity, a pinhole or slit that can be easily precharacterized and can almost always be shielded or distanced sufficiently from the target and backlighter environment to avoid closure during the experiment.
2. Multiple images from slightly different lines of sight can be cast on a single detector using a single backlighter spot. If each image is gated at a separate time while the backlighter laser beam is on, then a sequence of images is obtained in time, typically 16 for a wide variety of experiments at Nova and OMEGA. Alternatively, those 16 images could be recorded on a static detector such as x-ray film or an x-ray CCD and then summed for improving SNR. In this case, the temporal resolution is set by the backlighter x-ray duration.
3. The cooling of the backlighter plasma due to energy loss out the edges of the laser spot is mitigated by having a large spot.

We now consider how area backlighting scales from Nova and OMEGA to NIF. Consider an experiment seeking to backlight a sample driven by a given radiation temperature hohlraum environment. NIF will have $\approx 4^2 \times$ more power than Nova or OMEGA, hence NIF will be able to drive a $4 \times$ larger hohlraum to the same temperature. If the sample is also scaled up by $4 \times$ in size and $4^2 \times$ in area, then the area backlighter must also be scaled up by $4^2 \times$ in area. Assuming for the moment a fixed-photon-energy backlighter, keeping the backlighter x-ray intensity fixed is equivalent to keeping the backlighter laser intensity fixed. Therefore, under the current assumptions, the backlighter laser power must be $4^2 \times$ larger. Stated differently, the fraction of laser power apportioned to backlighting would be fixed as we transition from Nova to NIF. Because we typically use 10 to 20% of the beams at Nova for backlighting, we would require 10 to 20% of the beams on NIF. However, this is overly optimistic. First, because of the $\approx 4 \times$ longer drive durations possible with NIF for

fixed hohlraum temperature, the samples are likely to be thicker, hence requiring higher photon energy backlighting, which requires higher backlighter intensities and power. Second, for a given spatial and temporal resolution and number of collected photons per resolution element, the required backlighter x-ray intensity is fixed only if the imaging detector is kept at the same stand-off distance as at Nova. This in general will not be possible when considering how diagnostic damage and debris concerns scale to NIF.⁴⁶ Consider NIF vs Nova, with NIF providing 4^3 more energy. For fixed debris and x-ray fluence ($\propto \text{energy}/v^2$), the stand-off distance v would be $4^{1.5} \times$ further at NIF. For the same number of collected photons per resolution element, the required backlighter x-ray and hence laser intensity would be $4^3 \times$ greater. Therefore, the combination of higher backlighter intensity and larger area required for NIF experiments could easily set the backlighter power requirement greater than the total NIF power available.

One could consider increasing the x-ray conversion efficiency of area backlighters by switching to underdense volume emitters such as foams and gas-filled targets.^{47–49} However, even for a predicted $30 \times$ increase in conversion efficiency at NIF scale (from, e.g., 0.3% to 10%) by switching from foil to volume emitters, the required fraction of laser power apportioned to such an area backlighter could still reach an undesirable 40% by the above scaling arguments.

Point-Projection Backlighting Using Point Targets

In point-projection backlighting, a point source of x rays casts a shadow of magnification $M = (v + u)/u$ of the sample of interest at the detector³⁸ (see Figure 1b). The principal advantage of this technique over area backlighting is that for a given x-ray photon energy and hence given laser intensity I_L , the power requirements are greatly reduced,²³ by the ratio of the point source area to the sample area (often factors of $>100 \times$). The other main advantage is that the detrimental long-range spatial structure from area backlighter nonuniformities are

absent for an isotropically emitting point source. Current techniques create a point source by firing a best-focus beam on thin wires or dot targets. However, point-projection backlighting has been less widely used up to now because area backlighter power requirements were still reasonable at Nova scale, and because of the following disadvantages:

1. The spatial resolution is determined by the hot emitting plasma size, which expands in time, degrading resolution. To counteract this effect, experiments have used either a short (<200-ps) backlighter pulse and a static detector, or a gated detector timed to view the earliest unexpanded phase of the backlighter plasma. A related disadvantage is that x-ray conversion efficiency is lowest early in time.⁵⁰
2. The small plasma-source size leads to more cooling by 2D and 3D expansion, reducing efficiency (i.e., edge effects are proportionately more important).
3. Because there are no imaging elements between the sample and detector as in area backlighting, the background contribution from sample self-emission is increased by the ratio of the sample to resolution element area. This forces point-projection experiments to view either cold samples, images at very high $h\nu$, or images in gated mode after the drive beams are off. Fortunately, many high-energy-density experiments are diagnosed under these conditions. For opacity experiments, the backlighter must be spectrally brighter than the sample of interest over a large range of wavelengths.
4. Until a true single-line-of-sight x-ray framing camera is in routine use,^{51–53} multiple lines of sight are required for each radiograph, translating to a separate point backlighter per frame.

The combination of the area backlighter advantages and the multitude of point-projection backlighter disadvantages has

discouraged the routine use of point-projection imaging at facilities such as Nova. However, because area backlighting does not scale well to NIF, we have revisited point-projection backlighting in the following section with the aim of mitigating or eliminating several disadvantages.

Point-Projection Backlighting Using Pinholes

A new point-projection x-ray radiography technique has been developed that combines all the advantages in efficiency and flexibility of the previous methods. This technique uses pinholes to define the backlighter source size (see Figure 1c), thus allowing for arbitrarily long-duration backlighting with minimal laser-power requirements. The energy losses from 2D and 3D expansion are mitigated because the optimum plasma size is now set by the minimum laser spot size rather than the fiber size (for NIF, a 300- μm spot vs a typical 10- μm -diam fiber).

In Figure 2a, we show gated, 4.7-keV x-ray point projection radiographs of a 50- μm vertical wire created by a backlit 25- μm pinhole. Lineouts (Figure 2b) across the wire show that the expected 1D resolution of 21 μm is maintained for several nanoseconds (Figure 2c). The backlighter laser power was only 0.2 TW, representing 20 \times less power than used by typical Nova area backlighters. The required backlighter laser power could have been further reduced, only limited by either the minimum achievable spot size or, as in this case, the conservative tolerance given to beam alignment (± 200 μm). The technique has also been used recently to image imploding foamballs and shells used for quantifying symmetry in NIF-scale hohlraums. A comparison of such 4.7-keV data from backlit-pinhole backlighting vs traditional area backlighting is shown in Figure 3. Clearly, the image SNR and uniformity are superior in the case of the backlit pinhole. In addition, it is interesting to note that while the backlit image of the 3-mm shell is Figure 3 used only two 3.5-ns-duration OMEGA backlighting beams totaling 0.15 TW in power, an area backlighting image would have

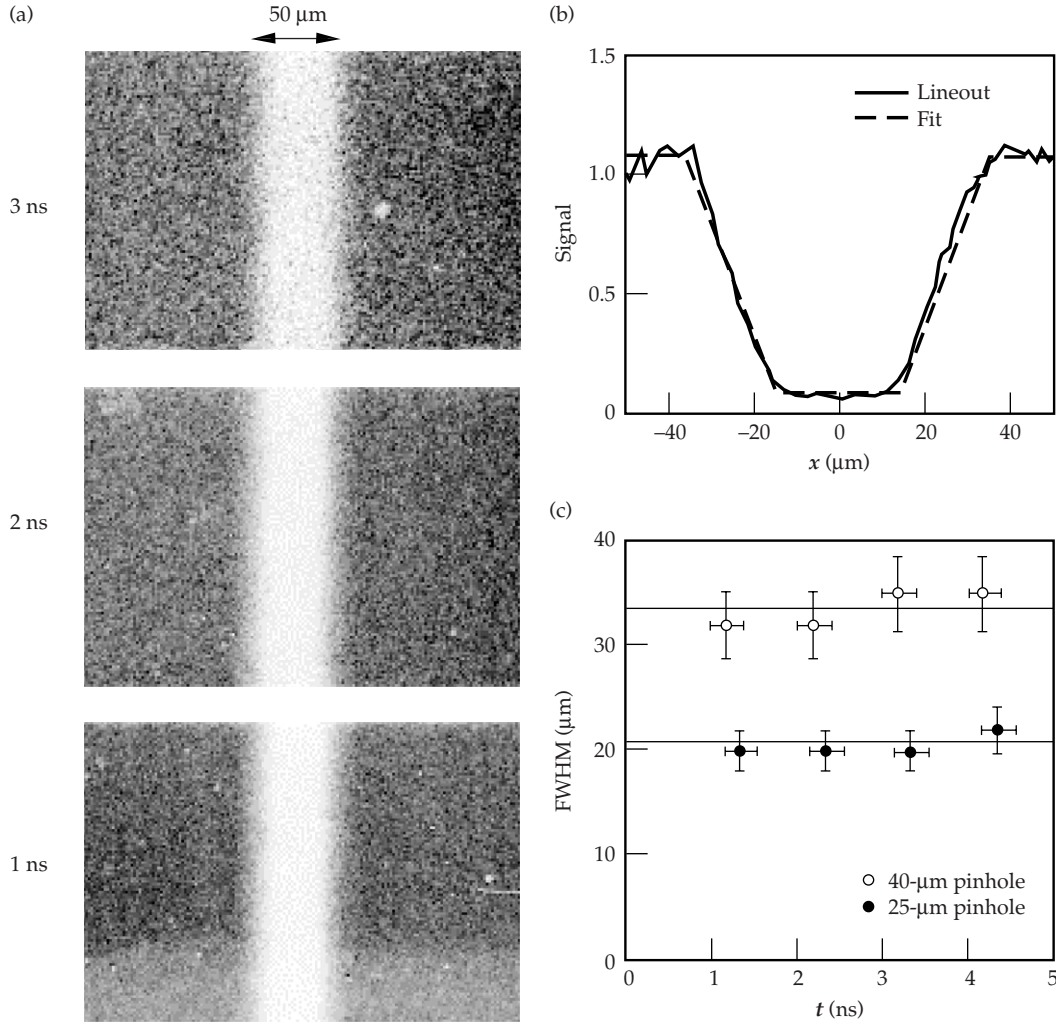


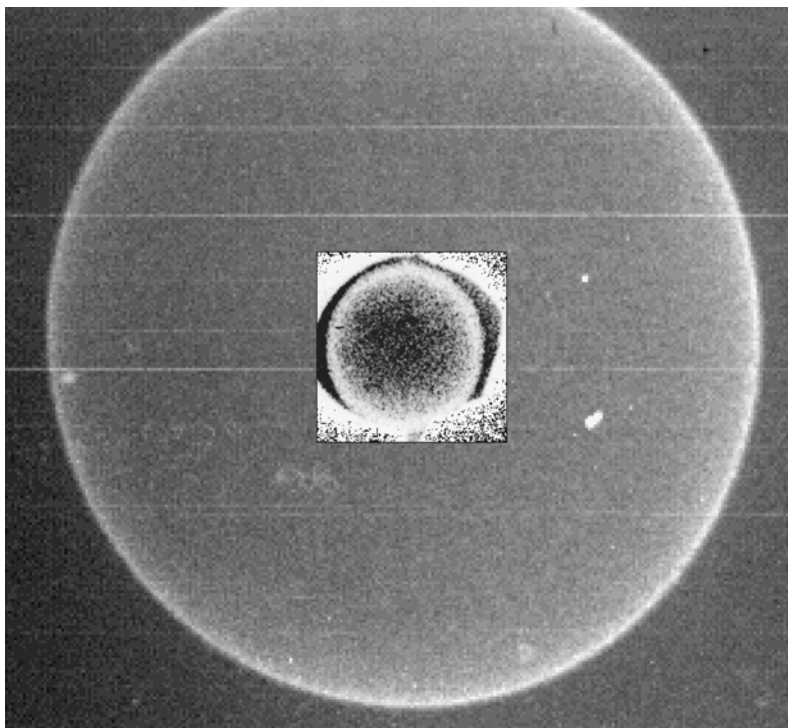
FIGURE 2. (a) Gated backlit pinhole radiographs at 4.7 keV of 50-μm-diam W wire. Pinhole diameter is 25 μm. (b) Lineout across wire radiograph at $t = 1$ ns (solid line), overplotted with fit (dashed line) convolving 50-μm-diam wire shadow with 21-μm-FWHM source size. (c) Resolution vs time for 25-μm-diam backlit pinhole (closed circles) and 40-μm-diam pinhole (open circles). Horizontal lines are predicted resolution assuming no pinhole closure. (08-00-0899-1591pb01)

required 15 TW, $3\times$ greater than all the laser power available from the OMEGA laser at that pulse length.

The new issue brought to the fore by backlit pinholes is the possibility of pinhole closure due to pinhole substrate ablation by the backlighter x rays produced at a distance p . From Figure 1c, ensuring an adequate backlighter field of view r at the sample a distance q from the pinhole requires that $p < q(s/r)$, where s is the backlighter source size. Because q is limited by beam travel and s should be minimized to reduce laser power requirements, this sets a maximum value for p and hence a minimum value for the x-ray fluence at the pinhole, which, assuming an intensity-independent x-ray conversion efficiency,

is $\propto I_L \tau s^2 / p^2$. The current experience at Nova (as shown on Figure 2c) and OMEGA is that 25- and 50-μm pinholes do not close appreciably during 4 ns of 4.7-keV irradiation from plasmas created by a 0.15-TW, 400-μm-diam laser spot at $p = 500$ μm. Scaling to NIF, with $s_{\min} = 250$ μm, $q_{\max} = 5$ cm, and assuming a required field-of-view $r \approx 5$ mm, sets $p_{\text{NIF}} = 2.5$ mm. Hence, for the same duration backlighter pulse length and same x-ray fluence at the pinhole, the backlighter power at NIF could be increased by $\sim 25\times$ (i.e., to 4-TW) levels without increased risk of closure. For smaller pinholes, the effects of closure can be mitigated by limiting the duration of the backlighter x rays, by tamping the

FIGURE 3. Gated backlit pinhole radiograph of 3-mm-diam Ge-doped plastic shell. Pinhole diameter is 50 μm . Inset: gated radiograph from 500- μm -diam Ge-doped plastic shell obtained using area backlighter and 15- μm pinholes. (08-00-0899-1592pb01)



pinholes with low-Z materials, or by allowing for some closure during the experiment.

We note that the 64 \times increase in backlighter intensity will keep the image intensity fixed given the 4^{1.5} \times larger stand-off distances that will be required for NIF diagnostics. The 25 \times power increase is also consistent with the idea that only a single 3-TW NIF beam per frame will be required when using backlit pinholes, at least for the mid-keV backlighting range.

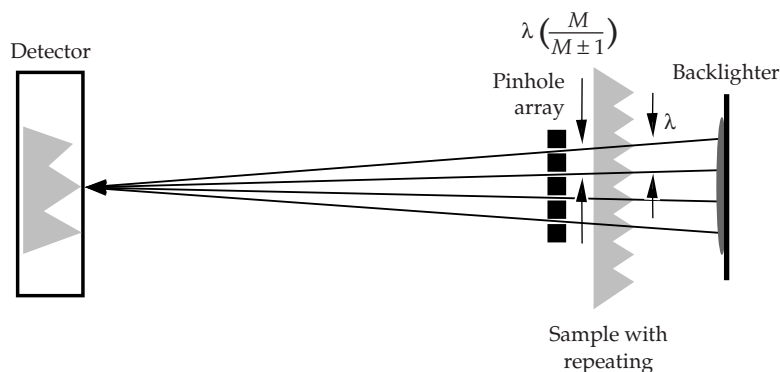


FIGURE 4. Example of use of pinhole array to increase throughput when backlighting samples with repeating features. A similar scheme exists in point-projection mode. (08-00-0899-1593pb01)

Pinhole and Slit Arrays

For NIF, the assumption so far has been that the number of photons per resolution element can be maintained fixed at a more distant detector by increasing the backlighter laser intensity and hence x-ray intensity. However, increasing laser intensity can lead to over-driven plasmas, which suffer from reduced absorption due to parametric laser-plasma instabilities, reduced x-ray conversion efficiency at the photon energy of interest, and production of unwanted, higher-energy penetrating photons. One alternative to increasing laser intensity is to collect more photons by creating redundant images. If the sample to be backlit is nonrepeating (such as an implosion), one can use a pinhole array to produce several nonoverlapping images that later can be summed⁵⁴ electronically to improve SNR. If the sample to be backlit has a repeating pattern (such as a single-mode Rayleigh–Taylor-type experiment), then one can constructively add images directly onto the detector by an appropriate choice of pinhole or slit array separation. For example, Figure 4 shows that if the pinhole or slit separation is set at $\lambda[M/(M\pm 1)]$ where λ is the wavelength of the feature of interest and where the + (–) is

for area (point-projection) backlighting, respectively, then the signal can be increased by a factor of n , where n is the number of slits or pinholes.

The use of even short slits (<300 μm long) rather than pinholes for imaging 2D sample features (such as planar interfaces⁴ and ridge modulations²) is recommended when photons are scarce, because a factor of 10 \times increase in collection efficiency is easily realized with minimal rotational-tolerance requirements on the slit. We note that the slits can be used either in the traditional manner with area backlighters or to provide line-projection backlighting.

Backlighter Sources

Besides increasing the collected photon flux, one can work at increasing the emitted backlighter photon flux. A second alternative to increasing incident laser intensity as a means of increasing backlighter photon flux is to create distributed or spectrally broader sources.

Distributed, Polychromatic Backlighters

Many beam facilities such as OMEGA and NIF are ideally suited for creating distributed backlighter sources. Figure 5a shows an example of a configuration using stacked foils. This scheme has the advantage of providing more photons without the above-mentioned problems associated with driving just one foil. In particular, the use of multiple foils allows flexibility in setting the optimum laser intensity for producing a given photon energy source. Clearly, the flux at the detector will be optimized if there is no reabsorption as the radiation passes through intervening foils, a particular concern for commonly used resonance line radiation. Because the vast majority of backlighter experiments do not require monochromatic sources (just spectrally well understood sources), one possibility is to make each foil of a slightly different element, stacked in such a way that each intervening foil is transparent to the characteristic radiation of the previous foils.

The example shown in Figure 5a is for K-shell emitters, where foil thicknesses need only be as thin as 10 μm . The backlighter

concept of irradiating a thin foil from both sides has already been demonstrated.⁵⁵ The multiple foil scheme should also work for more opaque L- (see Figures 5b and c) or M-shell emitters,²⁷ by switching to micron-thick coatings on low-Z substrates. Besides providing higher x-ray fluxes when necessary, these backlighter schemes should be useful for point-projection spectroscopy studies of interface hydrodynamics and for opacity studies. For the latter, the polychromatic M-shell backlighter may be the solution for creating spectrally brighter

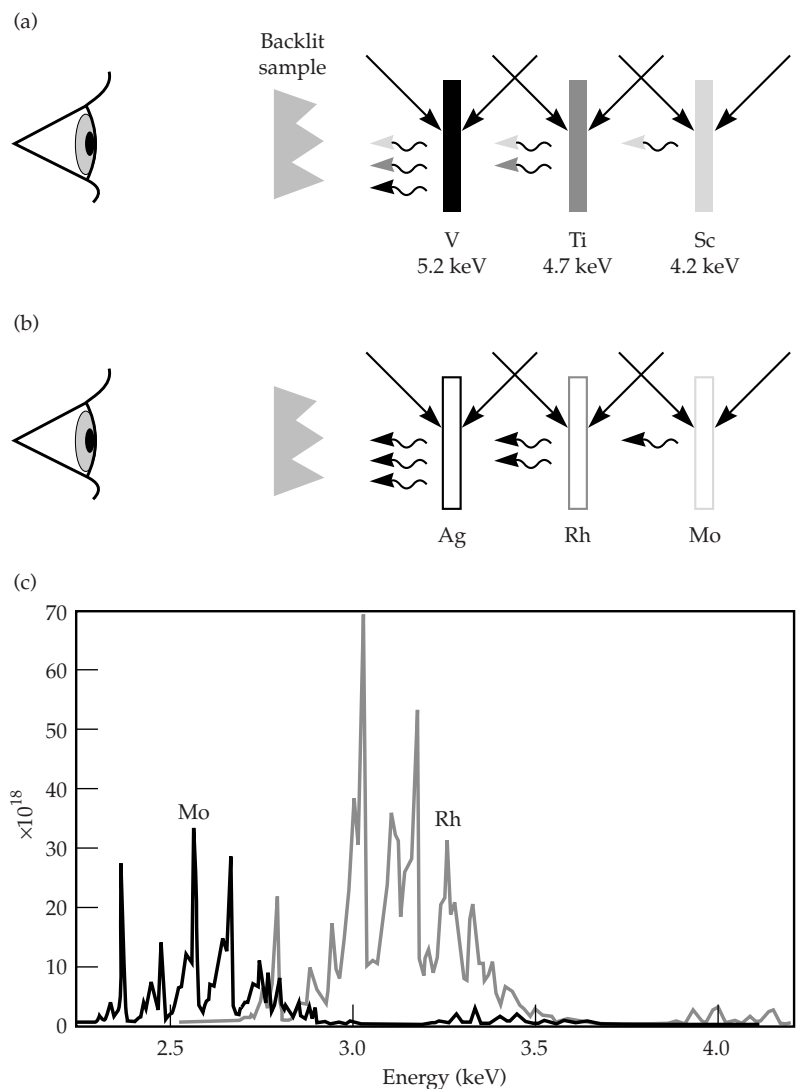


FIGURE 5. (a) Schematic of polychromatic backlighting configuration for K-shell emitters. Each foil is transparent to its own He-like resonance line radiation and to line radiation of foils behind it. (b) Schematic for L-shell emitters. (c) Example of characteristic resonance L-shell line radiation from laser plasmas from two neighboring elements ($Z = 42$ and 45) in the periodic table. (08-00-0899-1594pb01)

backlighters, which need not be spectrally continuous, over a range of photon energies below ~ 4 keV.

Picket-Fence Backlighters

Long-pulse (>500 -ps) laser backlighters have been found to be more efficient than shorter-pulse backlighters for photon energies <10 keV.^{21,50} This is generally attributed to better laser coupling^{56–58} in the longer-scale-length plasmas that are allowed to develop with a longer pulse. Coupling this fact with the desire to operate at peak laser power without approaching peak-laser-fluence damage concerns suggests a picket-fence backlighter approach. Figure 6a shows an example of a streaked x-ray spectrum from a Nova 1-TW, 2ω picket-fence laser beam irradiating a Zn disk at 3×10^{15} W/cm². The first 500-ps picket produces a monochromatic He-like emission line at 9 keV. The second and third pulses at 4-ns intervals interact with a pre-expanded volume of Zn ions to produce a broadband x-ray source, with up to $3\times$ more brightness and efficiency when integrated over the 8.5- to 9.5-keV spectral range (see Figure 6b).

Detectors

Until recently, x-ray film was used for short-pulse backlighting. Framing cameras based on microchannel plates (MCPs)^{59–61} equipped with film recording media were used for long-pulse backlighting or to reduce background levels during short-pulse backlighting.⁴⁰ In Table 1, the SNR contribution from these detectors and their subelements (where measured) is tabulated for a pixel size at the detector plane of $100\text{ }\mu\text{m}$. This SNR has been verified to be almost independent of the signal level or detector gain; it is not associated with shot noise, which should not be a concern for a well designed experiment. The representative $100\text{-}\mu\text{m}$ pixel size has been chosen to be large compared to the spatial resolution of the detectors but small compared to the dimensions of the detector. The SNR increases roughly linearly with pixel size between the size range of detector resolution and detector dimensions. The table shows that x-ray film provides a factor of ~ 2 better SNR, that the combination of MCP and optical film, at a level very similar to the optical film. However, it is clear from these small values of SNR that the

FIGURE 6. (a) Streaked spectrum from picket-fence backlighter. Backlighter was created by three ~ 1 -TW, 500-ps, 2ω pulses separated by 4 ns and focused to 3×10^{15} W/cm² on single spot on Zn foil. Spectrum is centered around 9-keV He-like resonance line of Zn. The weaker interleaved streaked spectrum occurring ~ 1 ns earlier is from second, lower-intensity beam. (b) Running spectral integral of x-ray output for each picket in arbitrary units. (08-00-0899-1595pb01)

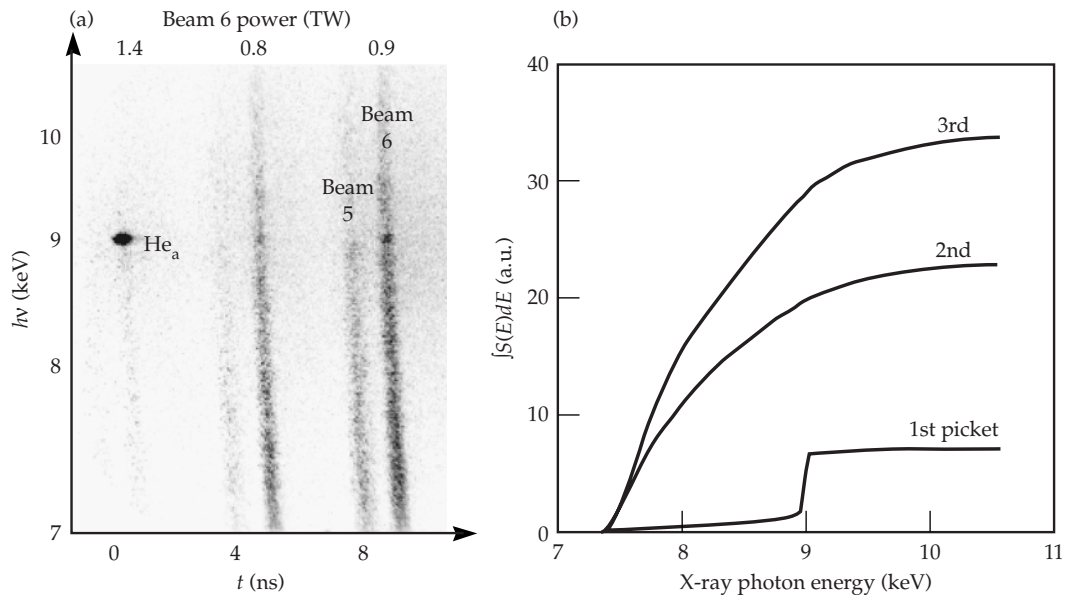


TABLE 1. SNR at 100- μm scale for various detectors and subelements, with and without flat-fielding, in the absence of shot noise. For CCD, signal approaching MCP saturation level of 20,000 counts is assumed.

Detector element	Raw SNR	SNR after flat field
X-ray film (DEF)*	18	
Optical film (T3200)	17	
MCP + T3200	8	12
CCD	10,000	
MCP + CCD	9	>50

*DEF = direct-exposure film

useful spatial resolution for 2D images recorded on both static and gated detectors has been limited by noise⁶² rather than by the intrinsic resolution (30 to 40 μm for MCPs,^{63–65} <5 μm for film).

Removal of Film Random Noise

To reduce random noise levels, the x-ray film used for static backlighting has been gradually replaced by x-ray CCD detectors. Similarly, the optical film used as recording medium for MCP-based framing cameras has been replaced by optical CCDs.⁶⁶ While the SNR for film is characteristically a constant,⁶³ the absolute value of the CCD noise is characteristically a constant, as determined by the dark noise level. For a typical 9- μm -pixel optical CCD in use at OMEGA, the random dark noise is 20 counts compared to an optimized exposure level (i.e., approaching MCP saturation) of 20,000 counts. Averaged over a 100- μm spatial scale, the CCD SNR is hence $\sim 10,000$, a $>500\times$ improvement over the film SNR (see Table 1). Even at a few percent of maximum exposure level, the CCD SNR is still an order of magnitude greater than for film. Adding prompt data viewing and analysis capabilities and at least as good a dynamic range to the SNR advantage, we see CCDs as clearly desirable for replacing film in all future backlighting experiments.

Removal of MCP Fixed-Pattern Noise

In Table 1, we note that the SNR for MCP-based film data is smaller than the film SNR on its own. We have recently discovered that this additional noise source in photon-rich MCP-based framing camera data is repeatable on spatial scales as small as 20 μm (see Figure 7a). This noise is dominated by nonuniformities in the MCP phosphor. The noise can be removed on any data by dividing, pixel by pixel, by a uniformly illuminated test image (i.e., by flat-fielding⁶⁷). An example of the improvement in uniformity before and after flat-fielding is shown in Figure 8. The improvement in SNR accomplished so far through such flat-fielding is also given in Table 1 for both film and CCD as the recording medium.

In summary, the combination of flat-fielding MCP-based data and switching to CCD as recording medium can increase SNR by close to an order of magnitude. We anticipate that this will improve gated backlighting data quality for a wide variety of experiments at OMEGA and NIF. Moreover, the recent retro-trend of using

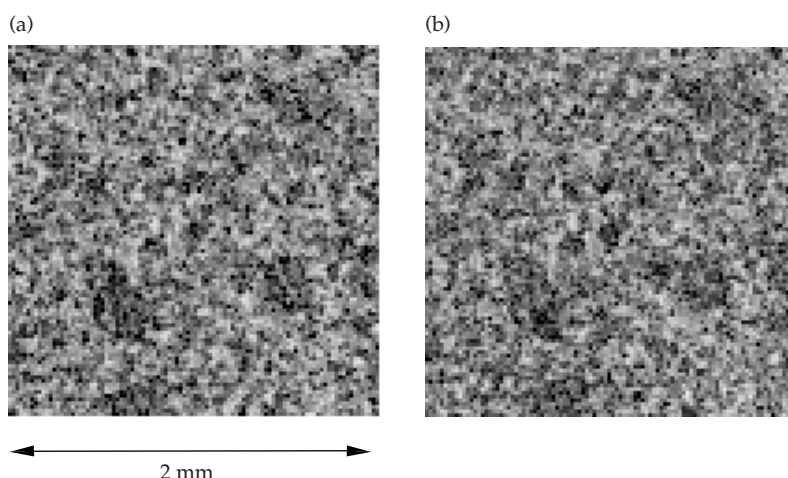
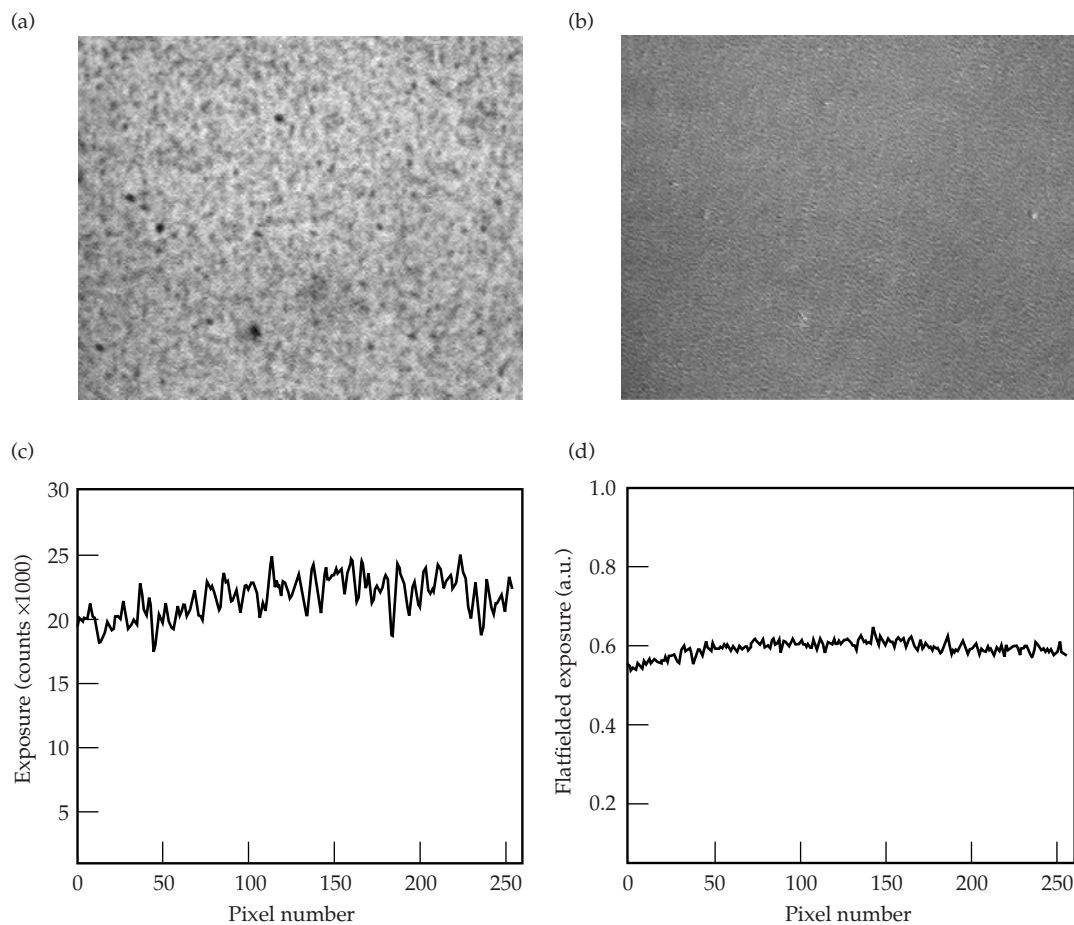


FIGURE 7. (a) and (b) are two successive film images of a 2 mm \times 2 mm section of uniformly x-ray illuminated microchannel plate (MCP) run in dc mode. The MCP is operated at low gain (<100) to minimize the contribution of shot noise. The two images show repeatable structure down to a 20- μm scale. (08-00-0899-1596pb01)

FIGURE 8. (a) CCD image of uniformly illuminated section of MCP run at low gain in pulsed mode. (b) CCD image (a) divided by second uniformly illuminated image. (c) 81- μm -wide lineout across image (a). (d) 81- μm -wide lineout across flat-fielded image (b), demonstrating 5 \times improvement in SNR. (08-00-0899-1597pb01)



static x-ray CCDs to avoid gated-detector fixed-pattern noise can now be reversed. Clearly static detection has limitations; it is not applicable in those experiments where the time-integrated noise from sample self-emission and target background emission exceeds the backlit image exposure level. The discovery of how to provide high-SNR gated imaging also paves the way for long-pulse, point-projection, backlit-pinhole backlighting to become perhaps the backlighting method of choice for NIF.

Summary

X-ray backlighting is a powerful tool for diagnosing a large variety of high-energy-density phenomena. Traditional area backlighting techniques used at Nova and OMEGA cannot be extended efficiently to NIF scale. New, more efficient backlighting sources and techniques are required and have begun to show promising results.

These include a backlit-pinhole point-projection technique, pinhole and slit arrays, distributed polychromatic sources, and picket-fence backlighters. In parallel, there have been developments in improving the data SNR and hence quality by switching from film to CCD-based recording media and by removing the fixed-pattern noise of MCP-based cameras.

We plan to further validate these new backlighting concepts at the OMEGA facility over the next year. In particular, we hope to validate the backlit pinhole concept for pinholes as small as 5 μm and quantify the improvements in flux available from distributed polychromatic sources.

Acknowledgments

The authors thank the Operations crews of the Nova and OMEGA facilities, and support from the Z/Beamlet project for the picket-fence backlighter development.

Notes and References

1. J. D. Kilkenny, *Phys. Fluids B* **2**, 1400 (1990).
2. B. A. Remington et al., *Phys. Rev. Lett.* **67**, 3259 (1991).
3. S. G. Glendinning et al., *Rev. Sci. Instrum.* **70**, 536 (1999).
4. B. A. Hammel et al., *Phys. Fluids B* **5**, 2259 (1993).
5. D. H. Kalantar et al., *Rev. Sci. Instrum.* **68**, 814 (1997).
6. W. W. Hsing and N. M. Hoffman, *Phys. Rev. Lett.* **78**, 3876 (1997).
7. S. G. Glendinning et al., *Phys. Rev. Lett.* **80**, 1904 (1998).
8. B. Yaakobi, D. Shvarts, R. Epstein, and Q. Su, *Lasers and Part. Beams* **14**, 81 (1996).
9. V. A. Smalyuk et al., *Phys. Rev. Lett.* **81**, 5342 (1998).
10. S. J. Davidson et al., *Appl. Phys. Lett.* **52**, 847 (1988).
11. J. Balmer et al., *Phys. Rev. A* **40**, 330 (1989).
12. C. Chenais-Popovics et al., *Phys. Rev. A* **40**, 3194 (1989).
13. J. Bruneau et al., *Phys. Rev. Lett.* **65**, 1435 (1990).
14. J. M. Foster et al., *Phys. Rev. Lett.* **67**, 3255 (1991).
15. D. M. O'Neill et al., *Phys. Rev. A* **44**, 2641 (1991).
16. T. S. Perry et al., *J. Quant. Spectrosc. Radiat. Transfer* **54**, 317 (1995).
17. C. A. Back et al., *J. Quant. Spectrosc. and Rad. Trans.* **58**, 415 (1997).
18. L. B. Da Silva et al., *Phys. Rev. Lett.* **69**, 438 (1992).
19. P. T. Springer et al., *Phys. Rev. Lett.* **69**, 3735 (1992).
20. D. L. Matthews et al., *J. Appl. Phys.* **54**, 4260 (1983).
21. D. W. Phillion and C. J. Hailey, *Phys. Rev. A* **34**, 4886 (1986).
22. O. L. Landen, E. M. Campbell, and M. D. Perry, *Opt. Commun.* **63**, 253 (1987).
23. B. H. Failor, E. F. Gabl, R. R. Johnson, and C. Shepard, *J. Appl. Phys.* **66**, 1571 (1989).
24. A. A. Hauer, N. D. Delamater, and Z. M. Koenig, *Lasers and Part. Beams* **9**, 3 (1991).
25. K. Eidmann and W. Schwanda, *Lasers and Part. Beams* **9**, 551 (1991).
26. R. L. Kauffman, *Physics of Laser Plasma*, A. Rubenchik and S. Witkowski, Eds. (North-Holland, Amsterdam, 1991) pp. 111–162.
27. P. Mandelbaum et al., *Phys. Rev. A* **44**, 5752 (1991).
28. J. D. Molitoris et al., *Rev. Sci. Instrum.* **63**, 5104 (1992).
29. S. G. Glendinning et al., *Ultrahigh- and High-Speed Photography, Videography, and Photonics*, G. Kyrall, Ed., in *Proc. SPIE* (Society of Photo-optical Instrumentation Engineers, Bellingham, WA, 1995) Vol. 2549, p. 38.
30. D. Attwood, B. W. Weinstein, and R. F. Wuerker, *Appl. Opt.* **16**, 1253 (1977).
31. P. M. Bell et al., *Ultrahigh- and High-Speed Photography, Videography, and Photonics*, in *Proc. SPIE* (Society of Photo-optical Instrumentation Engineers, Bellingham, WA, 1989) Vol. 1155, p. 430.
32. J.-P. LeBreton et al., *Ann. Phys. (Paris)* **19**, 87 (1994).
33. H. Azechi et al., *Appl. Phys. Lett.* **37**, 998 (1980).
34. O. L. Landen, *Rev. Sci. Instrum.* **63**, 5075 (1992).
35. J. A. Koch et al., *Appl. Opt.* **37**, 1784 (1998).
36. J. A. Koch et al., *Rev. Sci. Instrum.* **70**, 525 (1999).
37. B. A. Remington, B. A. Hammel, O. L. Landen, and R. A. Pasha, *Rev. Sci. Instrum.* **63**, 5083 (1992).
38. C. L. S. Lewis and J. McGlinchey, *Opt. Commun.* **53**, 179 (1985).
39. T. S. Perry et al., *Phys. Rev. Lett.* **67**, 3784 (1991).
40. K. S. Budil et al., *Rev. Sci. Instrum.* **68**, 796 (1997).
41. B. Yaakobi and A. J. Burek, *IEEE J. Quantum Elect.* **19**, 1841 (1983).
42. E. Forster, K. Gabel, and I. Uschmann, *Lasers and Part. Beams* **9**, 135 (1991).
43. F. J. Marshall and Q. Su, *Rev. Sci. Instrum.* **66**, 725 (1995).
44. R. Kodama et al., *Opt. Lett.* **17**, 1321 (1996).
45. N. M. Ceglio, *Lasers and Part. Beams* **9**, 71 (1991).
46. O. L. Landen, Ed., *NIF Diagnostic Damage and Design Issues*, Lawrence Livermore National Laboratory, Livermore, CA, UCRL-ID-134644 (1999).
47. R. L. Kauffman, L. J. Suter, H. N. Kornblum, and D. S. Montgomery, *ICF Quarterly Report* **6**(2), 43–48, Lawrence Livermore National Laboratory, Livermore, CA, UCRL-LR-105821-96-2 (1996).
48. L. J. Suter, R. L. Kauffman, J. F. Davis, and M. S. Maxon, *ICF Quarterly Report* **6**(3), 96–102, Lawrence Livermore National Laboratory, Livermore, CA, UCRL-LR-105821-96-3 (1996).
49. L. J. Suter, O. L. Landen, and J. Koch, *Rev. Sci. Instrum.* **70**, 663 (1999).
50. R. Kodama, T. Mochizuki, K. A. Tanaka, and C. Yamanaka, *Appl. Phys. Lett.* **50**, 720 (1987).
51. R. Kalibjian and S. W. Thomas, *Rev. Sci. Instrum.* **54**, 1626 (1983).
52. N. Finn, T. A. Hall, and E. McGoldrick, *Appl. Phys. Lett.* **46**, 731 (1985).
53. W. Sibbett et al., *Rev. Sci. Instrum.* **61**, 717 (1990).
54. L. Logory, P. Miller, and J. Moreno, Ed., *Image Averaging for Analysis and Display*, Lawrence Livermore National Laboratory, Livermore, CA, UCRL-ID-130146.
55. R. E. Turner et al., to be published in *Phys. of Plasmas* **7**, 333 (2000).
56. M. H. Key, *Phil. Trans. R. Soc. London A* **300**, 599 (1981).
57. W. C. Mead et al., *Phys. Fluids* **26**, 2316 (1983).
58. W. L. Kruer, *The Physics of Laser Plasma Interactions* (Addison-Wesley, Redwood City, 1988).
59. J. D. Kilkenny, *Lasers and Part. Beams* **9**, 49 (1991).
60. D. K. Bradley et al., *Rev. Sci. Instrum.* **63**, 4813 (1992).
61. M. Katayama et al., *Rev. Sci. Instrum.* **62**, 124 (1992).
62. V. A. Smalyuk et al., *Rev. Sci. Instrum.* **70**, 647 (1999).
63. J. D. Wiedwald et al., "Ultrahigh- and High-Speed Photography, Videography, and Photonics," in *Proc. SPIE* (Society of Photo-optical Instrumentation Engineers, Bellingham, WA, 1990) Vol. 1346, p. 200.
64. O. L. Landen et al., "Ultrahigh- and High-Speed Photography, Videography, and Photonics," in *Proc. SPIE* (Society of Photo-optical Instrumentation Engineers, Bellingham, WA, 1995) Vol. 2549, p. 38.
65. H. F. Robey, K. S. Budil, and B. A. Remington, *Rev. Sci. Instrum.* **68**, 792 (1997).
66. L. M. Logory et al., *Rev. Sci. Instrum.* **69**, 4054 (1998).
67. D. S. Montgomery, R. P. Drake, B. A. Jones, and J. D. Wiedwald, "High-Speed Photography, Videography, and Photonics," in *Proc. SPIE* (Society of Photo-optical Instrumentation Engineers, Bellingham, WA, 1987), Vol. 832, p. 138.

USING INTENSE LASERS IN THE LABORATORY TO MODEL ASTROPHYSICAL PHENOMENA

B. A. Remington

*D. Arnett**

R. P. Drake[†]

*H. Takabe***

Astrophysics traditionally has been the domain of large astronomical observatories and theorists' computers—the former producing images from deep space and the latter constructing intricate models to explain the observations. A component often missing has been the ability to quantitatively test the theories and models in an experimental setting where the initial and final states are well characterized.

In a new development, intense lasers are being used to re-create aspects of astrophysical phenomena in the laboratory, allowing the creation of experimental testbeds where theory and modeling can be quantitatively compared with data. Modern intense lasers produce energy densities in submillimeter-scale volumes that are far larger than those produced in any other laboratory. This allows access in the laboratory to phenomena that otherwise appear only in energetic astrophysical systems. With these highly versatile laser facilities, matter can be prepared reproducibly in conditions that are equivalent, in a rigorously scaled sense, to those in large astrophysical systems such as supernovae, Herbig-Haro jets, or giant planets. Examples of areas that can be studied include strong shock phenomena, high-Mach-number jets, strongly coupled plasmas, compressible hydrodynamic instabilities, radiation flow, photoevaporation front hydrodynamics, and fundamental

properties such as opacities and equations of state. Consequently, a vibrant new field of research is emerging—laboratory astrophysics with intense lasers. This topic was the subject of the *2nd International Workshop on Laboratory Astrophysics with Intense Lasers*, held in Tucson, Arizona, March 19–21, 1998.¹

The research discussed at this meeting has a different emphasis than work traditionally described as “laboratory astrophysics.” Most often, traditional laboratory astrophysics has focused on measuring fundamental parameters such as nuclear reaction cross sections and opacities. Nuclear fusion reactions are the fundamental energy source of the stars, and their cross sections quantify the individual reaction probabilities, allowing the heat production inside stars to be calculated. Opacities are the fundamental atomic properties that govern radiation transport within stars. Opacities quantify the probability that an atom will absorb photons that pass within its vicinity and consequently control to a large extent the temperature profiles of the interiors of stars. These fundamental “input” quantities—cross sections and opacities—are required in models of phenomena such as stellar pulsations and supernova (SN) light curves.

The research reviewed in this article is aimed at probing astrophysical dynamics directly by creating scaled reproductions of the astrophysical systems in the laboratory. This allows the “output” of astrophysics theories and modeling to be tested directly, where the initial and final states

*University of Arizona, Tucson, AZ

†University of Michigan, Ann Arbor, MI

**Osaka University, Osaka, Japan

are well characterized. We present a brief review of this conference on *Laboratory Astrophysics with Intense Lasers*, selecting out of the many topics discussed supernovae, supernova remnants, gamma-ray bursts, and high-pressure equations of state (EOS) relevant to the giant planets.

Supernovae

Core-collapse supernovae (SNe) represent the dramatic endpoint of one of nature's most impressive cycles: the life and death of a massive star.²⁻⁶ The final death throes of the star are spent in a high-stakes "tug of war" pitting quantum mechanical degeneracy pressure against the more familiar gravitational pressure. The outcome determines whether the final state is a white dwarf, neutron star, or black hole, and is based on the strength of the degeneracy pressure to withstand the radially inward tug of gravity.⁷ Stars with initial masses of $1-8 M_{\text{sun}}$ finish their hydrogen burning while their cores are not yet degenerate. They undergo core contraction, which raises the core density and temperature sufficiently to trigger He burning. These stars subsequently lose mass effectively, and end their lifetimes as white dwarfs, with masses of $\sim 0.6 M_{\text{sun}}$. White dwarfs are supported by the pressure of the degenerate electrons in their interiors; that is, it is the quantum mechanical Pauli exclusion principle that prevents further collapse. The maximum mass possible for a white dwarf is the Chandrasekhar limiting mass, $M_{\text{Ch}} \approx 1.4 M_{\text{sun}}$. Larger stars have high enough temperatures in their cores to continue the nuclear fusion burning cycle up to Fe. Once the core reaches Fe, the nuclear fusion reactions no longer release net energy (because the nuclear binding energy per nucleon is maximum in Fe, at nearly 9 MeV/nucleon), and the thermonuclear fires are extinguished. The mass of the Fe core continues to grow as the surrounding layers burn their way to this thermonuclear endpoint until the Fe core mass exceeds $\sim 1.4 M_{\text{sun}}$. At this point, there is no longer sufficient heat produced in the core to balance cooling by neutrino emission and photonuclear dissociation, and the core surrenders to gravity, triggering a catastrophic gravitational collapse that is over in a matter of seconds. This collapse is arrested only

when the core density reaches that of degenerate nuclear matter ($\sim 2 \times 10^{14} \text{ g/cm}^3$). The Fermi degeneracy pressure $P_{\text{deg}} \propto \rho^{2/3}$ (where ρ is density) increases sufficiently to stop the implosion, and a spectacular nuclear rebound occurs whose strength is determined by the EOS of bulk nuclear matter. By a mechanism still debated, this launches the powerful outward-propagating shock that first "stalls" in the infalling matter, then gets reenergized by convection and by energy deposition due to neutrinos emitted from the core. The shock thus restarted traverses the overlaying layers and effectively blows the star apart. Thus, the catastrophic end of the massive star marks the spectacular beginning of a core-collapse SN. This explosive birth is observed as a bright flash of UV light, as illustrated by the calculated light curve for SN1987A in the inset of Figure 1a.^{4, 8} If the core has a mass larger than $2-3 M_{\text{sun}}$, the core collapse continues to form a black hole.

Supernova Light Curves

The visual SN commences when the shock breaks out through the surface of the star about an hour after the core collapses.⁴ There is a sudden increase in temperature to 20–30 eV and luminosity, followed by a rapid drop in both quantities, as the star expands and cools adiabatically (Figure 1a inset). About 30 minutes after shock breakout, the luminosity approaches a constant value as the recombination front, which determines the photosphere, moves inward in mass at roughly the constant temperature (for hydrogen) of 6000 K. After some 20–40 days, the heat from the radioactive core, heated by Compton scattering of the γ -rays produced from ^{56}Ni , ^{56}Co , and ^{44}Ti , reaches the photosphere, and the light curve rises up in a broad secondary maximum (Figure 1a). Subsequently, the decay of the light curve is monotonic in time at a rate determined by the half-lives of the various radioactive nuclei that serve as the heat source. The light curve contains a wealth of information about the star and its explosion. The luminosity varies directly with the explosion energy per unit mass E/M and is also proportional to the initial radius of the star. For the same E/M , SNe from small stars are not as bright because more energy goes into hydrodynamic expansion. The

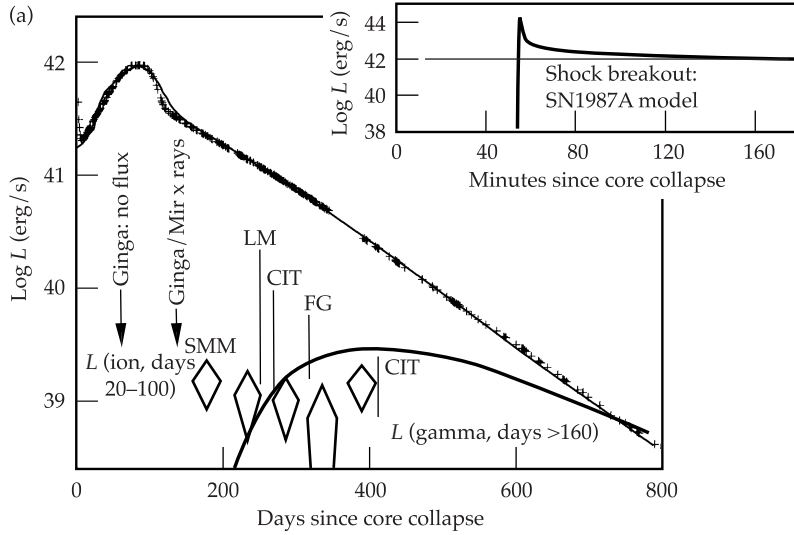
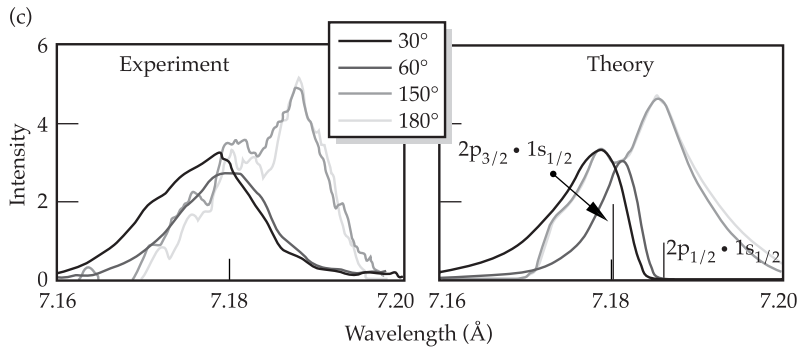
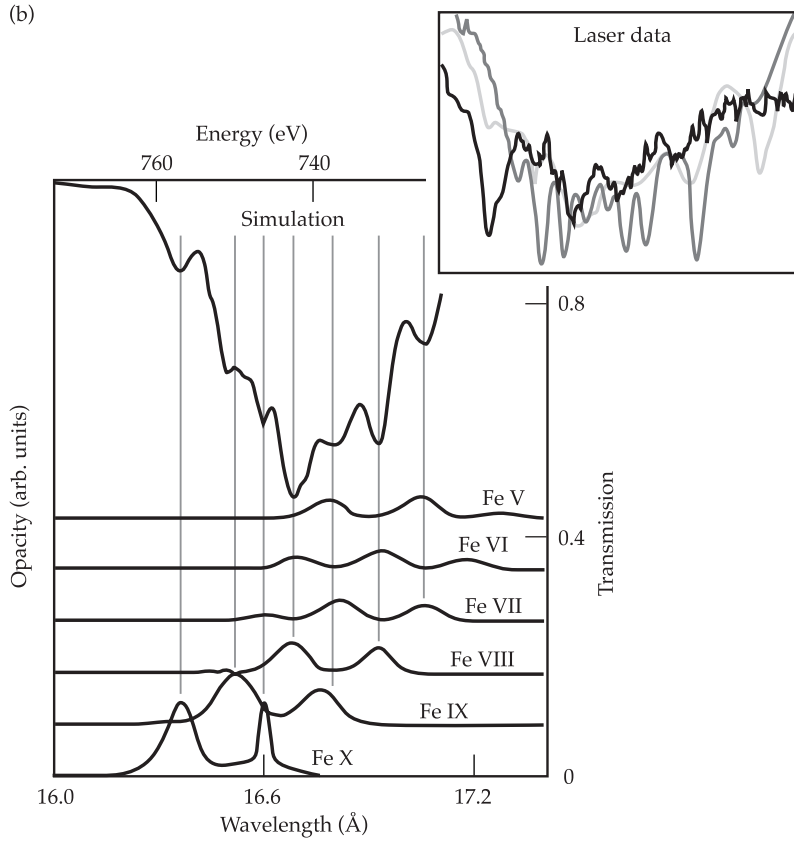


FIGURE 1. Supernova (SN) light curves and opacities. (a) Calculated light curves for SN1987A (reproduced from Ref. 4). (b) Modeling and experimental measurements of the opacity of Fe at a temperature of $T = 20$ eV (reproduced from Ref. 13). (c) Experimental measurements of radiation line transport through an expanding Al plasma with a large velocity gradient (reproduced from Ref. 14). (08-00-0899-1605pb01)



luminosity is on average inversely proportional to the opacity, because lower opacity means shorter radiative diffusion times. Finally, the light curve time evolution is sensitive to the degree that the core hydrodynamically mixes outwards into the envelope, bringing heat nearer to the photosphere. An ability to quantitatively calculate an SN light curve would allow the intrinsic brightness of the SN to be known. Comparison with the observed brightness would give its distance, through the expanding photosphere method.^{9,10} Together with spectroscopic measurements of its redshift, this allows the Hubble constant H_0 to be determined.¹¹ There are several aspects to synthetic light-curve calculations that could benefit from laboratory experiments, such as radiation flow, opacities, and hydrodynamic mixing.

Exploding stars create a homologous expansion, where each radiating region resides in a velocity gradient and sees plasma receding from it in all directions. For photons emitted in one region to escape the star, they have to pass through “windows” in opacity, where the absorption probability is low. In other words, the absorbing regions are always red shifted relative to the emitting regions. To construct a synthetic light curve, one needs to calculate these “expansion opacities.” Such calculations are very complex, and sophisticated opacity codes such as OPAL¹² are indispensable.

Experiments are being developed to test these difficult opacity calculations, focusing on atomic transitions that have not been explored previously. For example, in one experiment an Fe foil 25 nm thick was sandwiched between two C layers and heated to ~20 eV using x rays. The absorption spectrum near 730 eV was measured and analyzed, comparing several different opacity calculations (Figure 1b).¹³ Another experiment measured radiation line transport in an expanding plasma (Figure 1c).¹⁴ The experiment studied the structure of a doublet in the Al spectrum, at a wavelength near 7.18 Å. The emission occurs from an optically thick plasma with a significant velocity gradient, so that emission in one line is often absorbed and reemitted by the other line at another location in the plasma. The resulting line structure is complex, but can be repro-

duced by modeling only when this expansion effect on the radiation transport is taken into account. Hence, experiments are under development to test opacity calculations, both static and in expansion, relevant to SN light curves.

The 1D modeling of light curves such as those for SN1987A, even with the most sophisticated opacities, still fail to reproduce the time evolution. It appears that additional dynamics are at work. The modeling used to successfully reproduce the light curve for SN1987A shown in Figure 1a assumes that the radioactive Ni, while centrally concentrated, was distributed half-way to the surface of the star.⁴ This suggests that large-scale hydrodynamic mixing had to have occurred after the ⁵⁶Ni was synthesized in the core in the explosion. Hence, hydrodynamic instabilities appear to be an important ingredient in the dynamics of SN.

Instabilities in the Explosion Phase

A core-collapse SN is driven by an extremely powerful shock, and strong shocks are the breeding ground of hydrodynamic instabilities. Two such instabilities seem particularly important: the Rayleigh–Taylor (RT) and Richtmyer–Meshkov (RM) instabilities. The RT instability occurs when gravity tries to pull a heavier fluid through an underlying lighter one (for example, large air bubbles under water, or heated gas from a powerful explosion in the atmosphere). The RM instability is closely related, with the role of gravity replaced by the inertia from an impulsive acceleration due to a shock wave.

During the shock transit phase, the RM instability is triggered at each discontinuity in the density profile of the star, i.e., at the O-He and He-H “interfaces.” After shock transit, hydrodynamic mixing continues due to the RT instability, as the denser layers are decelerated by the lower-density outer layers. The outward mixing of the higher-density, radioactive core material (e.g., ⁵⁶Ni, ⁵⁶Co, ⁴⁴Ti) brings the radioactive heat source towards the surface of the star. These

explosion products decay by the emission of γ -rays, which Compton scatter off electrons in their vicinity. The consequent reheating of the photosphere causes the secondary maximum in the light curve (Figure 1a). The RT mixing induces this reinvigoration of the light curve to start earlier, broadening the secondary maximum. Observations of the light curve of SN1987A unambiguously showed this broadening of the secondary peak, suggesting enhanced transport from the core out to the photosphere.^{2,3} 2D calculations of the development of the mixing at the O-He and He-H interfaces using the supernova code PROMETHEUS^{15,16} show that spikes of denser O and He penetrate outward into the less dense envelope of H, while bubbles of H move inward relative to the average location of the H/He boundary (Figure 2a). This interpenetration occurs through the growth and nonlinear evolution of the RT instability.

Laser-based experiments can generate strong-shock initiated nonlinear hydrodynamic mixing conditions similar to those found in SNe. In a set of experiments scaled to reproduce the hydrodynamics of the He-H interface of SN1987A about an hour after explosion, a strong shock was passed through an interface separating dense “core” material (Cu) from the lower-density outer envelope (CH₂).^{17,18} A 2D

sinusoidal ripple (1D wave vector) was imposed at the interface. The subsequent 2D growth due to the RM and RT instabilities was measured by x-ray backlighting. Spikes of Cu penetrating upward into less-dense CH₂ were observed as a consequence of the RT instability (Figure 2b). This interpenetration was calculated in 2D with PROMETHEUS, and the simulations reproduced the observations very well.

A theoretical look at the relation between the hydrodynamics occurring in the SN versus in the laboratory experiment shows that a rigorous mapping exists. Consider the He-H interface at 1600 s in the SN and the Cu-CH interface at 20 ns in the laser experiment. In both settings, the Reynold’s number (the ratio of the inertial to the viscous force) and the Peclet number (the ratio of the convective to the conductive heat transport) are large. Therefore, viscosity and thermal diffusivity are negligible, and the dynamics of the interface are well described by Euler’s equations for a polytropic gas,¹⁹

$$\begin{aligned} \rho \left(\frac{\partial \mathbf{v}}{\partial t} + \mathbf{v} \cdot \nabla \mathbf{v} \right) &= -\nabla p , \\ \frac{\partial \rho}{\partial t} + \nabla \cdot (\rho \mathbf{v}) &= 0 , \text{ and} \\ \frac{\partial p}{\partial t} - \gamma \frac{p}{\rho} \frac{\partial \rho}{\partial t} + \mathbf{v} \cdot \Delta p - \gamma \frac{p}{\rho} \mathbf{v} \cdot \nabla \rho &= 0 , \end{aligned} \quad (1)$$

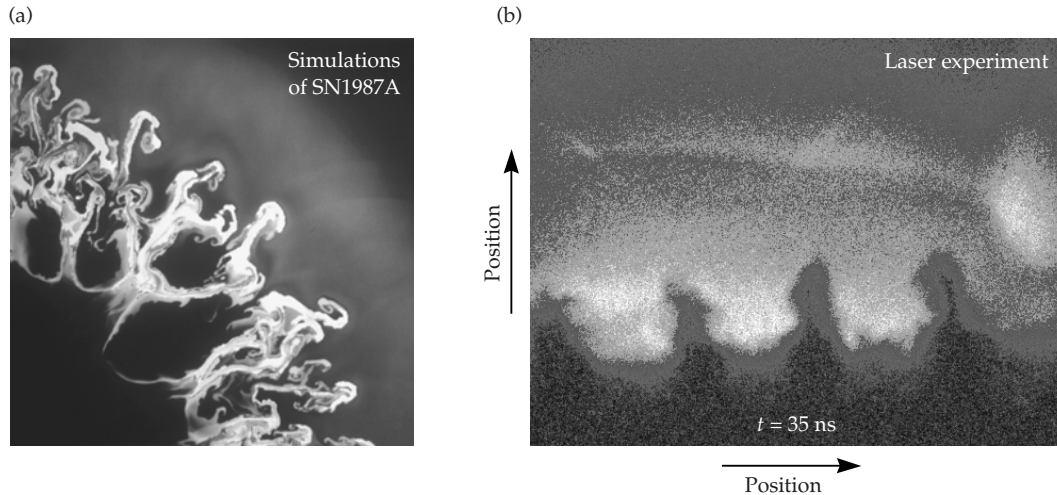


FIGURE 2. Mixing in SN explosion hydrodynamics. (a) Image of simulated hydrodynamic mixing from SN1987A at $t = 12000 \text{ s}$ (reproduced from Ref. 15). (b) An image from a laser experiment designed to measure this hydrodynamic mixing of a $\lambda = 200 \mu\text{m}$ wavelength ripple under scaled conditions at $t = 35 \text{ ns}$ (reproduced from Ref. 17). (08-00-0899-1606pb01)

which represent conservation of momentum, mass, and entropy, respectively. It is straightforward to show by substitution that Eq. 1 is invariant under the scale transformation

$$\begin{aligned} h_{\text{SN}} &\rightarrow ah_{\text{lab}}, \\ \rho_{\text{SN}} &\rightarrow b\rho_{\text{lab}}, \\ p_{\text{SN}} &\rightarrow cp_{\text{lab}}, \\ \tau_{\text{SN}} &\rightarrow a(b/c)^{1/2}\tau_{\text{lab}}, \end{aligned} \quad (2)$$

where h , ρ , p , and τ correspond to characteristic spatial, density, pressure, and time scales, and subscripts “SN” and “lab” refer to the supernova and laboratory laser experiment, respectively. When transformation (2) is inserted into Eq. 1, the constants a , b , and c cancel, and the dynamics described by Euler’s equation are indistinguishable in the SN and the laser experiment. Both settings are probing the same physics. Any insights gained through the laser experiment apply directly to the SN through the mapping described by Eq. 2. For example, the hydrodynamics illustrated in Figures 2a and 2b are similar, and can be related through the SN-to-laboratory mapping of h , ρ , p , τ , and $g = \nabla p / \rho$ (Eq. 2) giving 10^{11} to $50 \mu\text{m}$, $8 \times 10^{-3} \text{ g/cm}^3$ to 4 g/cm^3 , 40 Mbar to 0.6 Mbar, and $10g_0$ to $10^{10}g_0$, where these values were taken at times of 2000 s for the SN and 20 ns for the laboratory experiment.¹⁹

An example where laboratory experiments can generate valuable insights relative to the star is the comparison of RT instability growth in 2D versus 3D. PROMETHEUS simulations comparing the evolution of RT bubbles and spikes in two and three dimensions in a proposed laboratory experiment show that single-mode 3D perturbations should penetrate 30 to 50% farther than those in 2D, an effect which may contribute to the early rise in the secondary maximum at day ~ 30 in the light curve of SN1987A.^{2,3} Initial laboratory results confirm this difference for single-mode perturbations.²⁰

Supernova Remnants

While SN explosions mark the end of a massive star, they also mark the beginning of its new life as a supernova remnant (SNR). Well known examples of SNRs such as the remnants of Tycho’s SN,²¹ Kepler’s SN,²² the Cygnus loop,²³ SN1006,²⁴ and the Crab nebula²⁵ provide exquisite visual testimony to their violent births. There are several active areas of research regarding the dynamics and evolution of SNRs that may be better understood with laser experiments.

Shocks in the Supernova Remnant Phase

Shock dynamics dominate the evolution of SNRs. The rapidly expanding ejecta from the SN drive a shock forward into the surrounding medium, and a reverse shock forms where the ejecta are decelerated by the accumulating, shocked matter. The place where the ejecta and ambient medium meet, called the contact discontinuity, becomes hydrodynamically unstable. Currently the most actively observed SNR is the young remnant forming around SN1987A. This remnant consists of the standard SN ejecta expanding into the ambient medium, as well as a mysterious inner and two outer circumstellar nebular rings, which apparently existed prior to the SN explosion. Various models have been proposed for these rings, but as of yet no explanation accounts for accounts for their origin. The SN ejecta, however, are moving very fast ($\sim 10^4 \text{ km/s}$) compared to the nearly static ($\sim 10 \text{ km/s}$) inner ring, which has a diameter of ~ 1 light-year. It is widely expected that the ejecta-forward shock system will impact the inner edge of the inner ring within the next ~ 5 years. This should launch a strong shock into the ring, heating it to 100- to 300-eV temperatures, and cause emissions at all wavelengths, from optical to x ray. Careful observation of this impact should shed light on the structure, composition, and hopefully origin of the rings. Recent images of the inner ring^{26–28} show a

rapidly brightening, localized hot spot (upper right corner of Figure 3a), suggesting that perhaps the collision of the forward shock with the ring has actually started. Spectral imaging of Lyman- α radiation, which is produced at the reverse shock, indicates that the reverse shock has traversed about 70% of the distance from the ring to the star.²⁶

Laser experiments can produce shock structures similar to those in an SNR, under well scaled hydrodynamic conditions.^{19, 29–31} Experiments have been developed in 1D to reproduce the basic dynamics of SNR formation: fast-moving shock-induced ejecta sweeping into a surrounding low-density, static ambient atmosphere. This launches a forward shock into the ambient medium and a reverse shock into the stagnating ejecta (Figure 3b), much as the dynamics of SNR formation do. Indeed, the laboratory experiment can be modeled by the self-similar model of Chevalier³² developed to describe the 1D dynamics of SNRs.

Expectations are that the contact discontinuity (the meeting point of the ejecta and ambient plasmas) will be hydrodynamically unstable, and 2D experiments have

commenced looking at this. One of the driving motivations for studying SNR physics relevant to SN1987A is the long-awaited impact of the SN blast wave with the inner circumstellar nebular ring. The interaction of the shock with the ring is sure to be rich in 3D, strong-shock effects. A laser experiment is being developed to elucidate the 3D nature of the interaction of a strong shock with a localized high-density feature such as a sphere.³³ The 3D development strongly affects the interactions, with azimuthal (3D) modes growing, and enhancing the “shredding” of the sphere. A similar 3D effect is likely for the interaction of the SN1987A blast wave with the inner ring, and in shock-cloud interactions in general.³⁴

Under the current conditions for the remnant of SN1987A, the scale transformation based on Euler’s equations described above for the explosion hydrodynamics might be applied again. For this to be relevant, one has to consider whether the shock is radiative, and whether the ambient magnetic field localizes the plasma. For the current conditions of SN1987A, the plasma density is low enough that the shocks are not radiative; that is, the radiative cooling

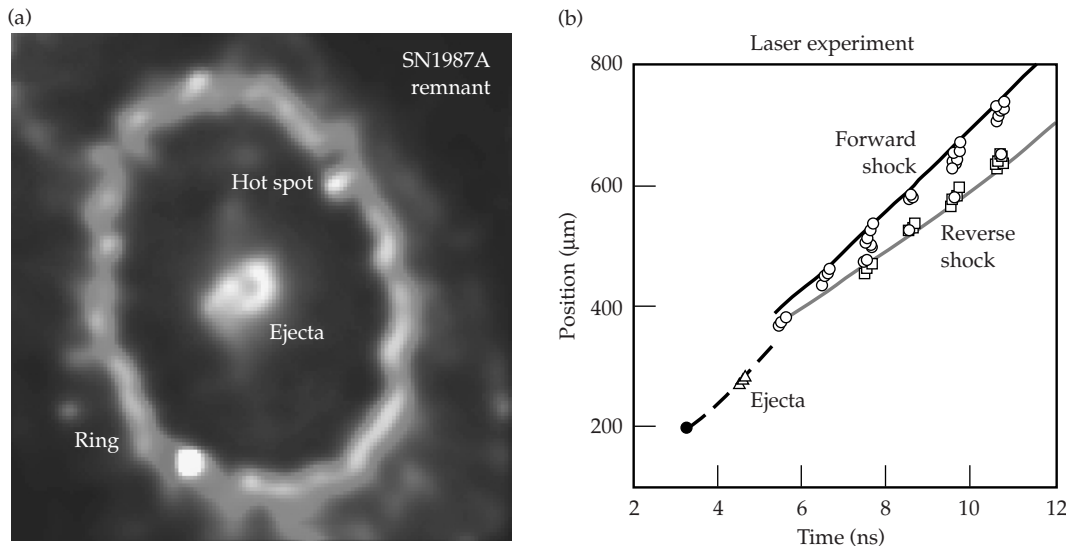


FIGURE 3. Young SN remnant dynamics. (a) Observational image of the inner circumstellar ring of SN1987A (<http://antwrp.gsfc.nasa.gov/apod/ap980217.html>). (b) Image from shock experiments designed to produce similar, scaled regimes of strong shock hydrodynamics (reproduced from Ref. 30). (08-00-0899-1607pb01)

time scale is long compared to a hydrodynamic time scale, $\tau_{\text{rad}}/\tau_{\text{hydro}} \gg 1$. Also, the ambient magnetic field, $B \sim 100 \mu\text{G}$, is large enough that the ion Larmor radius is much smaller than spatial scales of interest. Hence, the plasma can be treated hydrodynamically, the dynamics can be treated again with Euler's equations (Eq. 1), and the same rigorous scale transformation (Eq. 2) holds. For the SNR-to-laboratory transformation corresponding to the 1D experiment shown in Figure 3b, we get 0.03 light year mapping to $100 \mu\text{m}$, 10^4 km/s to

60 km/s, and 1 year mapping to 1 ns,¹⁹ where these values correspond to times of 13 years in the SNR and 8 ns in the laboratory experiment.

Another well known remnant, SN1006 (Figure 4a), is a good example of how shock-wave analysis techniques applied to recent images provide insights into the SN that exploded in the year 1006 at a distance of 2 kpc.²⁴ Spectral analysis of shock-induced astrophysical emissions can yield the temperature, density, degree of equilibration, ionization state, and velocity of the

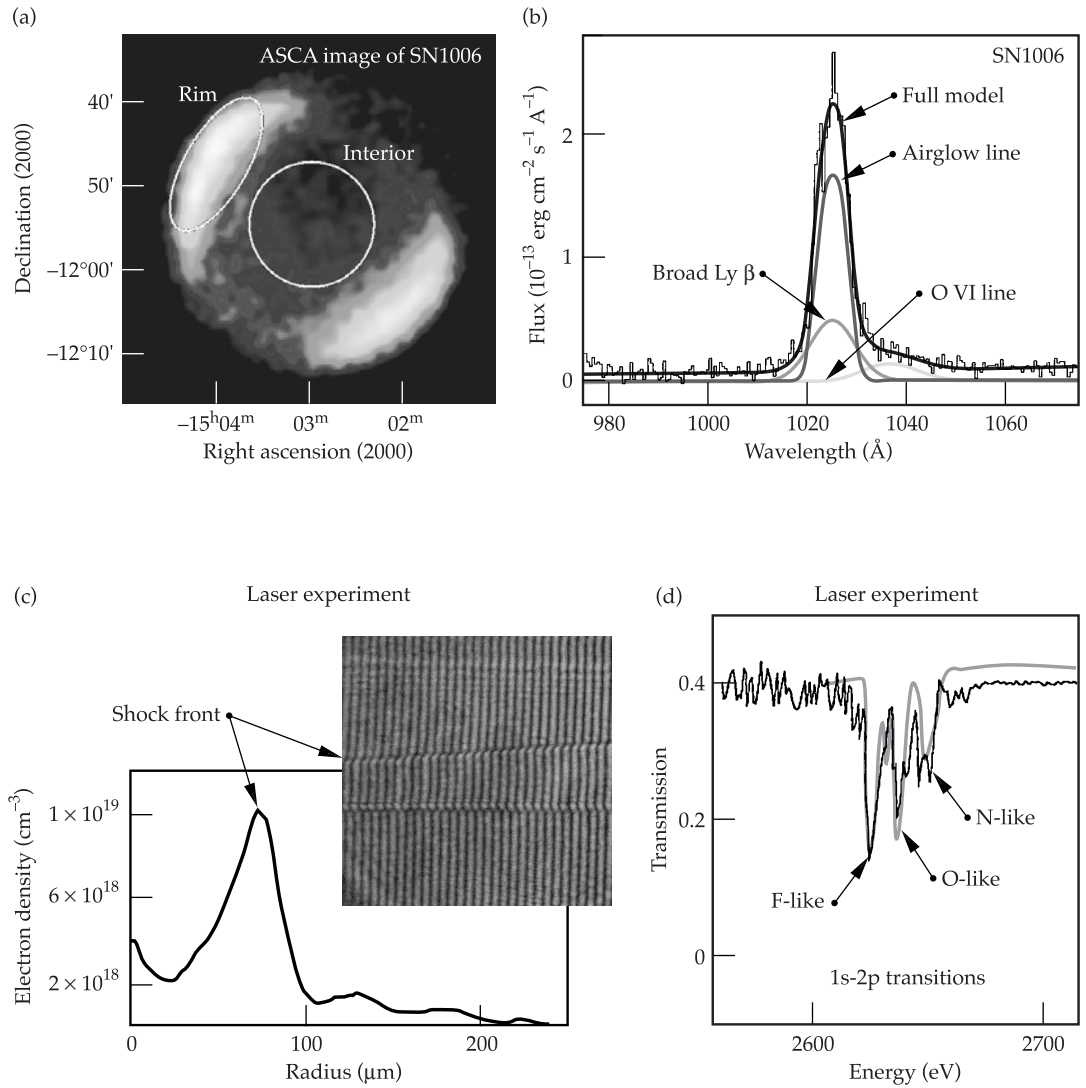


FIGURE 4. Shocks in older supernova remnants. (a) Observational image of SN1006 (http://www-cr.scphys.kyoto-u.ac.jp/research/pix/sn1006_i.gif). (b) Spectral analysis of the shocks from SN1006 (reproduced from Ref. 24). (c) Experimental image of a shock launched by a 40-fs, 15-mJ laser pulse in a gas cluster target, and diagnosed by optical interferometry (Ref. 39). (d) Spectral analysis of experimentally generated shocks in foam targets, from which the temperature behind shock front can be determined (reproduced from Refs. 43, 44). (08-00-0899-1608pb01)

shock. With an additional measure of the proper motion of the shock, the distance to the emitting source can also be determined. Such analysis of the shock-induced emissions from the remnant of SN1006 is given in Figure 4b. Here, emission lines from hydrogen (Lyman β) and from 5-times-ionized oxygen (O VI) are identified. This is an example of emissions from a “nonradiative” shock—a shock traversing a low-enough-density medium that the plasma behind the shock front is not cooling rapidly by radiation, $\tau_{\text{rad}}/\tau_{\text{hydro}} \gg 1$. The conclusion from this spectral analysis is that plasma turbulence in the shock front is not effective in producing temperature equilibration among the different ion species.

A long-standing mystery regarding astrophysical shocks is whether or not the electrons are strongly heated by the magnetized turbulence at the shock fronts of SNRs.³⁵ The impact of electrons upon emitting ions dominates the production of some emission lines, while the impact of protons dominates other emission lines. In the case of the shocks of the remnant from SN1006 and in several other cases analyzed to date, the electron temperature is found to be considerably below the ion temperature, $T_e \approx T_i/4$, for a Mach-50 shock.²⁴ This provides evidence that the magnetized turbulence at the shock wave does not rapidly force equilibration of the electrons and the ions. Developing an experimental setting to check the theories and analysis techniques of astrophysical shocks seems possible, at least for some situations, and would be very beneficial.

Laser-based experiments can produce strong shock waves for study in a variety of ways. In an experiment using a tabletop laser, a gas jet target produces an assembly of clusters of atoms of order 10 nm in size, each containing thousands of atoms. These clusters absorb the laser radiation from an 800-nm Ti:Sapphire laser with a pulse duration of 0.1 ps or less. This produces intense heating, disassembly of the clusters (“Coulomb explosion”), and radial expansion of the 2-mm-long by initially 50- μm -diameter laser-irradiated hot, cylindrical channel.^{36–38} Under sufficiently collisional conditions (Figure 4c), a Mach ~ 40 shock wave forms that drives the surrounding gas outward.³⁹ Whether a

magnetized shock can also be produced by this technique remains a topic for ongoing research, but an initial assessment looks promising.⁴⁰ Given the high initial temperature of the shock and the ability to experimentally vary the density and gas species, creating radiative and nonradiative shocks should be possible by this technique.

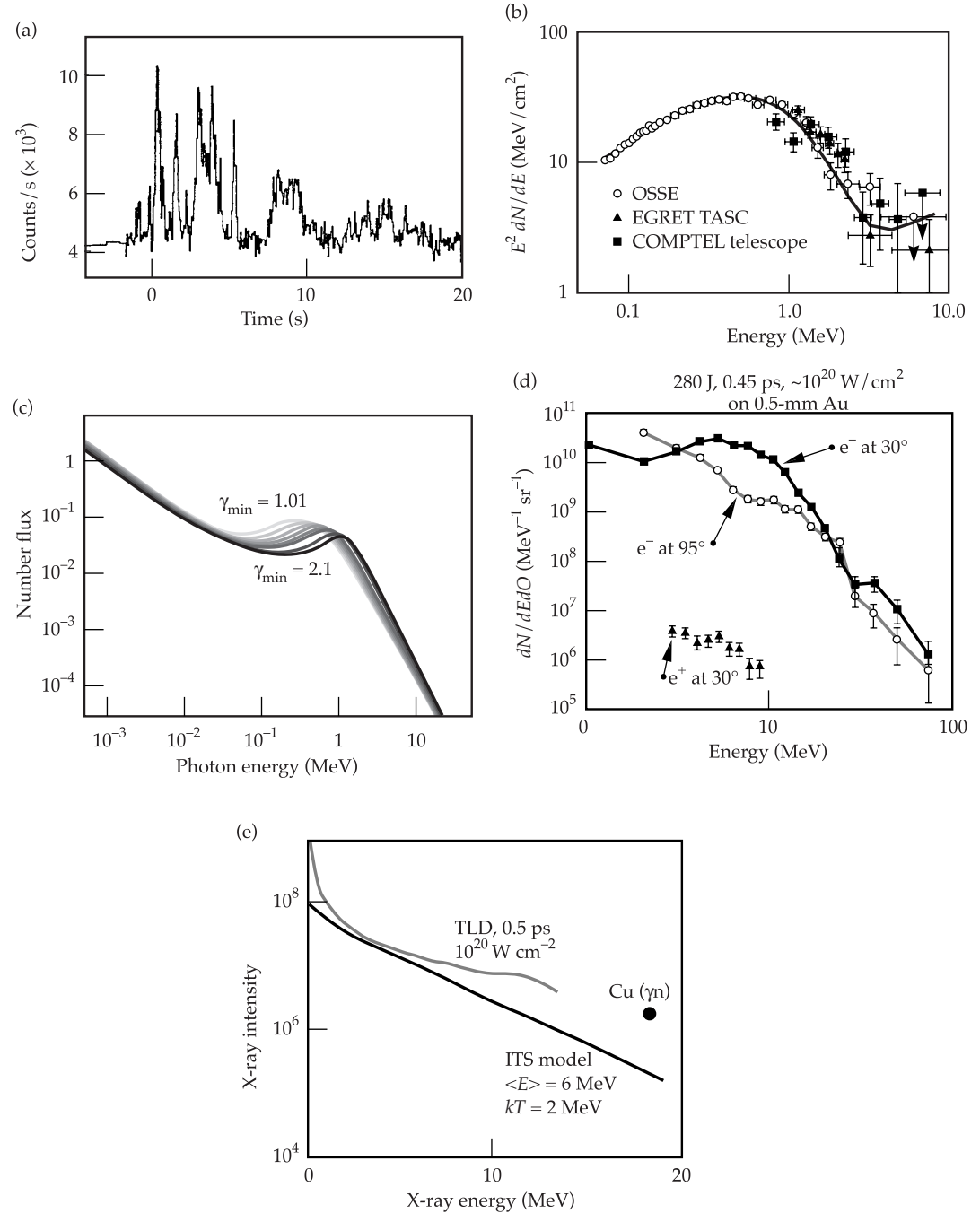
In astrophysical systems and the laboratory, shocks can be produced for which radiation is essential to the dynamics. Radiation from the shock wave can cause preheat, altering the conditions ahead of the shock wave, and the shock-generated radiation can be an important component of the energy flow within the system. An example from astrophysics is SN 1993J, whose progenitor was a red supergiant star, surrounded by a very dense stellar wind.⁴¹ The resulting shock structure was strongly radiative, and this affected the subsequent shock dynamics, leading to significantly higher densities behind the shock front. Laboratory shocks in which radiation affects the dynamics can also be created and studied. An experiment in which low-density foam was directly illuminated with an intense laser has been carried out,⁴² generating shocks whose radiation affected the matter ahead of them. Another radiative shock experiment^{43,44} has been conducted where the shock was launched by irradiating a foam target with soft x rays rather than direct laser illumination. Here, in three separate experiments conditions were created corresponding to (1) pure hydrodynamics (subsonic radiation wave), (2) pure radiation flow (supersonic radiative wave), and (3) intermediate dynamics (“transonic” regime). For each case, spectroscopy was used to determine the temperature profile in the plasma. For the case of the subsonic radiation front, the temperature behind the shock was determined spectroscopically. A spectrum from that analysis is shown in Figure 4d. What remains is to develop the theoretical transformation, mapping the conditions of astrophysical radiative shocks such as those associated with the remnant of SN1993J⁴¹ to the laboratory, so that these laser experiments can be turned into properly scaled reproductions of their astrophysical counterparts.

Gamma-Ray Bursts

Gamma-ray bursts (GRBs) are the greatest enigma in contemporary astrophysics.^{45–49} Detected at a rate of more than one per day from random directions in the sky, GRBs typically have burst durations of a few seconds, at photon energies of 0.1–10 MeV (Figures 5a, 5b). GRB distances remained unknown for the past two

decades, primarily because their radiation in all other wavelengths other than γ -rays was undetected. This changed recently with the determination of accurate positions (to within about 3 minutes of arc), obtained within hours of outburst by the BeppoSAX satellite. Optical spectroscopy of the light associated with the outburst, the “afterglow,” established that at least some of the GRBs are at cosmological

FIGURE 5. Gamma-ray bursts and relativistic plasmas. (a) Time evolution of the photon burst detected from GRB920110 (reproduced from Ref. 46). (b) Experimental γ -ray energy spectrum from GRB910601 (reproduced from Ref. 46). (c) Calculation of a GRB spectrum (reproduced from Ref. 50). (d) Measured electron-energy spectrum from Petawatt laser experiments (reproduced from Ref. 53). (e) Measured and calculated x-ray energy spectrum from experiments using the Petawatt laser (reproduced from Ref. 52). (08-00-0899-1609pb01)



distances of several billion light years (redshifts of $\Delta\lambda/\lambda = 1$ to 3). To generate the observed luminosities then requires total source energies of $\sim 10^{53}$ ergs/burst. The rapid rise time and rapid variability ($\Delta t \sim 1$ ms) observed in some bursts (Figure 5a) imply a source size $R_i \approx c\Delta t \approx 10^7$ cm, i.e., these tremendous total energies appear to be emitted from very compact sources. The observed photon energy spectra can extend to ~ 100 MeV, have a power-law shape (Figure 5b), and are well fit with a simple functional form, $N(E)dE \propto E^{-\alpha}dE$, with spectral index $\alpha \approx 2$. This suggests that the source plasma is optically thin to the radiation observed. (If the source plasma were optically thick, the photons would thermalize, and the observed spectrum would have a Planckian, not a power-law shape.) This presents a problem. When two photons with energies E_1 and E_2 interact, their center-of-mass energy is $\sim 2(E_1 E_2)^{1/2}$, and the interaction can produce an e^+e^- pair if $(E_1 E_2)^{1/2} > m_e c^2$ [Ref. 45]. Denote the fraction of photon pairs in a GRB satisfying this condition as f_p . The optical depth (OD) for the $\gamma\gamma \rightarrow e^+e^-$ process varies as $OD \propto f_p/R_i^2$, and is very large. Pairs are produced prodigiously, and, by Compton scattering, they would make the plasma optically thick, thermalizing the photon spectrum. The observed spectra, however, are nonthermal, hence the “compactness problem.” The fireball model was developed to resolve this problem without introducing “new physics.” In this model, the source creates a relativistically expanding fireball so that the emission region is moving towards the observer at relativistic velocities.^{45,49} Consider a source of radiation moving towards an observer at rest with a relativistic velocity characterized by a Lorentz factor $\Gamma = 1/(1 - v^2/c^2)^{1/2} \gg 1$. The observer detects photons with energy $h\nu_{\text{obs}}$, whereas these photons in the rest frame of the emission region have energy $h\nu_{\text{obs}}/\Gamma$. Hence, at the emitter, the fraction of photons with energies high enough to produce e^+e^- pairs, f_p , is reduced by a factor $\Gamma^{-2\alpha}$. Also, the emitting region appears Lorentz contracted, so that in its rest frame, the emission region is larger, with $R_i \approx \Gamma^2 c\Delta t$. The result is that the optical depth for the process $\gamma\gamma \rightarrow e^+e^-$ now

varies as $OD \propto f_p/\Gamma^{4+2\alpha}R_i^2$, which for $\Gamma > \sim 100$ lowers the optical depth sufficiently to resolve the compactness problem. Through the blue shift boost, we observe the high-energy photons, but the emission region remains optically thin, giving the observed γ -ray power-law spectrum. The kinetic energy of the GRB ejecta is assumed to be randomized behind internal (“reverse”) shocks and emitted as high-energy photons when the shock is at a radius of $r_{\text{int}} = \Gamma^2 c\Delta t = 10^{12}$ to 10^{13} cm, for $\Gamma = 100$ to 300. The “afterglow” is assumed to happen from emissions behind the external (“forward”) shock at a radius of $r_{\text{ext}} > \sim 10^{17}$ cm.

Most GRBs show variability on time scales much shorter than (typically one hundredth of) the total GRB duration.⁴⁸ In the fireball model, such variability comes from internal (“reverse”) shocks, which convert a substantial part of the directed kinetic energy to internal energy. This energy is then radiated as γ rays by synchrotron and inverse-Compton emission of shock-accelerated electrons. The GRB overall duration reflects the duration over which energy is emitted from the source. Following internal shocks, the fireball rapidly cools and continues to expand, driving a relativistic blastwave into the surrounding interstellar medium gas. This external shock continuously heats new gas and produces relativistic electrons that may produce the delayed radiation observed on time scales of days to months, that is, the afterglow. So, a relativistically expanding fireball produces the rapidly varying, hard x rays by internal shocks, and the longer-lived slow “afterglow” decay by the external shock.

Despite its qualitative successes, the fireball model is incomplete. The cause of GRBs is unknown, but must be spectacular because such great distances require enormous energies for the burst to appear so bright. The merger of a binary pair of neutron stars, the core collapse of a failed SN, and other exotic events involving black holes and relativistic jets have been suggested.^{45,46} Radiation escapes the fireball only after it expands to radii many orders of magnitude larger than the original size of $\sim 10^7$ cm. The γ -ray emission occurs when the source has expanded to $\sim 10^{13}$ cm

and the afterglow at $>10^{16}$ cm. Hence, the observed radiation does not provide direct information on the underlying source. The predictions of γ -ray emission from the fireball involve the interaction of plasma with shocks moving at relativistic velocities and with magnetic fields. The details of this interaction are not understood. This superheated conglomerate is thought to expand relativistically in a fiery ball or jet of plasma, with copious production of e^+e^- pairs. Explosion energies are estimated to be in the range of 10^{52} to 10^{53} erg (approaching the rest mass energy of the Sun). Figure 5c shows results of Monte Carlo simulations of the γ -ray spectrum of a GRB,⁵⁰ using a model in which energetic electrons and positrons from the fireball produce γ rays through multiple Compton upscattering of low-energy photons. This model qualitatively reproduces the observed GRB spectra and time evolution. A related phenomenon is the origin of ultrahigh-energy cosmic rays (10^{20} eV), which are thought to occur by the Fermi acceleration mechanism at the fireball wave front.⁴⁷

Aspects of the underlying fireball physics may be accessible in the lab. In experiments under development to benchmark astrophysical codes for radiation hydrodynamics, a radiative, high-Mach-number jet has been created and characterized.⁵¹ Here, the initial conditions were a hot (~ 1 keV), high-velocity (~ 700 km/s) jet of highly ionized Au plasma, where the radiative cooling effects were large. Perhaps more relevant are experiments under way using the ultrahigh-intensity laser called the Petawatt.⁵² Here, planar targets are irradiated by a laser pulse (10^{20} W/cm²), producing an expanding high-energy-density wave of hot plasma, that is, a “laboratory fireball.” The initial plasma temperature is thought to be several MeV, the plasma is relativistically hot, and e^+e^- pairs are created. For the highest-intensity shots, electrons have been observed up to energies of 100 MeV, and positron energy spectra have also been recorded (Figure 5d).⁵³ Perhaps most interesting in these experiments is the excitation of nuclear states in the ~ 20 -MeV range. The energetic electrons yield high-energy x rays through bremsstrahlung (Figure 5e), which excite the nucleus through the giant dipole resonance. The

nucleus de-excites by γ -ray emission or by emitting nucleons. Photoneutron interactions can leave the nucleus in long-lived excited states that can be counted after the fact by γ -ray spectroscopy. The exact laser-plasma dynamics and subsequent plasma fireball evolution are still being worked out, but what is clear is that plasmas have now been created in the laboratory with a $T \approx 1$ MeV “thermal” component, and a higher-energy tail.^{52,53} Significant e^+e^- production and excited nuclear levels have been observed. Hence, aspects of the underlying GRB fireball physics, such as relativistic plasma effects, are becoming accessible in the laboratory.

Giant Planets

The “high stakes tug of war” between quantum mechanical degeneracy pressure and the more familiar gravitational pressure was discussed above in the section on SNe. A somewhat more benign environment in which to consider strong degeneracy effects is the steady-state interiors of the giant planets such as Saturn and Jupiter and the newly discovered brown dwarfs,^{7, 54–56} as represented by the phase diagram shown in Figure 6a.⁵⁷ Here, because of their lower mass, $M \leq 0.08 M_{\text{sun}}$, these bodies never ignite as stars, and the degeneracy pressure and strongly coupled effects dominate.

Strongly coupled plasmas are typically characterized by the dimensionless parameter $\Gamma = (Ze)^2/akT$, where a is a characteristic separation distance between ions. In plasmas with $\Gamma \ll 1$, thermal effects dominate, and the plasma is considered “ideal.” When $\Gamma \geq 1$, the Coulomb interactions become an equal player, and the plasma enters the strongly coupled regime, represented by the region to the right and below the $\Gamma = 1$ line in Figure 6a. When $\Gamma > 178$, the plasma becomes so strongly coupled that the ions freeze solid into a crystal lattice. Also, when the densities are high enough or temperatures low enough that $kT < \epsilon_F$, where $\epsilon_F = p_F^2/2m_e = (1/8)(3/\pi)^{2/3}(h^2/m_e)n_i^{2/3} \propto \rho^{2/3}$ is the Fermi energy, the plasma is called degenerate and is represented by the region to the right and below the $\epsilon_F = kT$ line in Figure 6a. Here, electron degeneracy pressure becomes a major part of the total

pressure. The isentropes for Jupiter and the brown giant G1229B⁵⁶ shown in Figure 6a indicate that these bodies, which are made up predominantly of H and He, are both strongly coupled and highly degenerate. Hence, the internal structure, $\rho(r)$, $T(r)$, and to some extent the external magnetic fields of the giant planets are determined by the equation of state (EOS) of degenerate H and He at high pressure, $P = 1$ to 100 Mbar. The EOS of strongly coupled, degenerate plasma, however, is notoriously difficult to calculate from first-principles theories due to the complexity of including quantum mechanical effects into classical thermodynamic theories. Experiments in this parameter regime are a vital component in efforts to improve our understanding of Jupiter, the other giant planets, and brown dwarfs. Large laser facilities allow EOS experiments to be extended to high pressure, $P > 1$ Mbar.

The EOS of a material can be determined by measuring its response to a known applied pressure. Measurements of the EOS of cryogenic deuterium, D (an isotope of hydrogen), at applied pressures ranging from 220 kbar to 3.4 Mbar have been made on the Nova laser.⁵⁷ Here, laser ablation generates the applied pressure. In these experiments, the transition of H from a molecular fluid insulator phase to a monatomic metallic phase was unambiguously observed. A clear departure from the standard theoretical EOS models for H was found in the

compressibility of D_2 in this regime (Figure 6b). The results were consistent with a new model that included the potential energy sink caused by molecular dissociation ($D_2 \rightarrow D + D$). These results, together with extensive results from gas-gun experiments at lower pressure,^{58,59} have implications for the composition and dynamics of the outer layers of Jupiter, the other giant planets, and brown dwarfs.

The pressure and temperature in the mantle of Jupiter near the surface are in the range of 1 to 3 Mbar and a fraction of an electron volt. Deeper in the interior, the pressure and temperature increase, rising to 40 Mbar and a couple of electron volts at the center.⁵⁸ Near the surface, H exists as the molecule H_2 , but dissociates to $H + H$ and ionizes deeper in the mantle. This transition of H from insulator to conductor is important because conducting H in the convective zone is thought to create the 10- to 15-G magnetic field of Jupiter. One of the fundamental open questions about the interior of Jupiter is whether there is a sharp boundary, a plasma phase transition, between a molecular H mantle and a monatomic H core at a radius of $\sim 0.75 R_J$ and pressure of 3 Mbar. The regimes accessed by the laser and gas-gun experiments represented on Figure 6b span this critical transition from mantle to core of Jupiter, and suggest that a sharp discontinuity between molecular (mantle of Jupiter) to

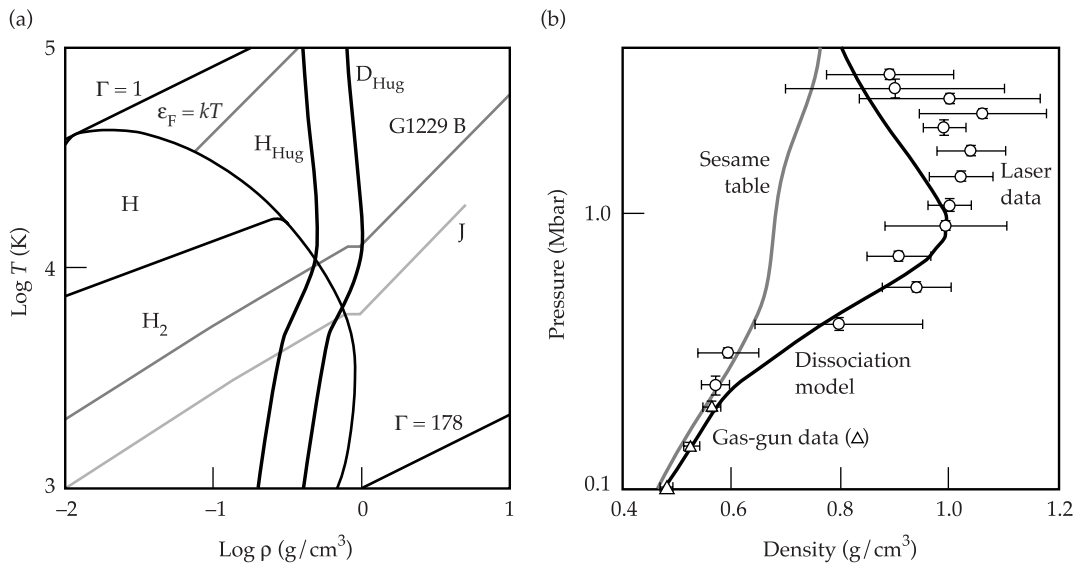


FIGURE 6. The phase diagram and equation-of-state (EOS) experiments relevant to the giant planets and brown dwarfs.⁶⁷ (a) Theoretical phase diagram of H (reproduced from Ref. 57) relevant to Jupiter and the brown dwarf G1229B. (b) Measured compression (density) vs shock-induced pressure, that is, the measured principal Hugoniot for cryogenic liquid D_2 (reproduced from Ref. 57). (08-00-0899-1610pb01)

monatomic (core of Jupiter) H does not exist. The experiments^{57,60,61} suggest that on the Jovian isentrope, molecular H probably begins to dissociate at 400 kbar and dissociation continues smoothly to completion at ~3 Mbar, with metallization occurring right in the middle of this region at ~1.4 Mbar and ~4000 K. It now seems likely⁶⁰ that currents near the surface of Jupiter at radii out to $0.95 R_J$ contribute to the surface magnetic field, whereas previously it was thought that the magnetic field was formed deeper in the interior at ~0.75 R_J . The EOSs of astrophysically relevant materials are being measured on other lasers as well, including LULI,⁶² Vulcan,^{62,63} Helen,⁶⁴ Astrix,⁶⁵ GEKKO,⁶⁶ and Shenguang-I.⁶⁷ This whole area of measuring high-pressure EOS on intense lasers represents fertile new territory for planetary and astrophysical research.

Notes and References

1. <http://lasers.llnl.gov/lasers/target/astro>
2. W. D. Arnett, J. N. Bahcall, R. P. Kershner, and S. E. Woolsey, *Ann. Rev. Astron. Astrophys.* **27**, 629–700 (1989).
3. W. Hillebrandt, and P. Höflich, *Rep. Prog. Phys.* **52**, 1421 (1989).
4. David Arnett, *Supernovae and Nucleosynthesis* (Princeton Univ. Press, 1996).
5. H. Bethe, *Rev. Mod. Phys.* **62**, 801 (1990).
6. Stan Woosley and Tom Weaver, *Scientific American*, 32 (Aug. 1989).
7. H. M. Van Horn, *Science* **252**, 384 (1991).
8. D. Arnett, *Ap. J. Suppl.* (Apr. 2000), in press.
9. B. P. Schmidt et al., *Ap. J.* **395**, 366 (1992); *ibid.*, **432**, 42 (1994).
10. R. G. Eastman et al., *Ap. J.* **466**, 911 (1996); *ibid.*, **430**, 300 (1994).
11. D. Branch et al., *Phys. Plasmas* **4**, 2016 (1997).
12. C. A. Iglesias, F. J. Rogers, *Ap. J.* **464**, 943–53 (1996).
13. C. Chenaïs-Popovics, *Ap. J. Suppl.* (Apr. 2000), in press.
14. J. Wark et al., *Phys. Plasmas* **4**, 2004 (1997); *Phys. Rev. Lett.* **75**, 1680 (1994); P. K. Patel et al., submitted to *JQSRT* (1999).
15. E. Muller, B. Fryxell, and D. Arnett, *A&A* **251**, 505–514 (1991).
16. B. Fryxell, E. Muller, and D. Arnett, *Ap. J.* **367**, 619–34 (1991).
17. J. Kane et al., *Ap. J.* **478**, L75–L78 (1997).
18. B. A. Remington et al., *Phys. Plasmas* **4**, 1994–2003 (1997).
19. D. D. Ryutov et al., *Ap. J.* **518**, 821 (1999).
20. M. M. Marinak et al., *Phys. Rev. Lett.* **75**, 3677 (1995).
21. U. Hwang, J. P. Hughes, and R. Petre, *Ap. J.* **497**, 833 (1998); P. F. Velazquez et al., *A&A* **344**, 1060 (1998).
22. K. J. Borkowski and A. E. Szymkowiak, *Ap. J.* **477**, L49 (1997); R. Braun, *A&A* **171**, 233 (1987); E. Dwek, *Ap. J.* **322**, 812 (1987).
23. N. A. Levenson et al., *Ap. J. Suppl.* **118**, 541 (1998); *Ap. J.* **484**, 304 (1997); *ibid.*, **468**, 323 (1996); J. J. Hester et al., *Ap. J.* **420**, 721 (1994); R. A. Resen et al., *A. J.* **104**, 719 (1992).
24. J. C. Raymond, W. P. Blair, K. S. Long, *Ap. J.* **454**, L31–L34 (1995); P. F. Winkler and K. S. Long, *Ap. J.* **486**, L137 (1997); *ibid.* **491**, 829 (1997).
25. J. Hester et al., *Ap. J.* **456**, 225 (1996).
26. E. Michael, R. McCray, K. J. Borkowski, C. S. J. Pun, G. Sonneborn, in preparation (1999).
27. K. J. Borkowski, J. M. Blondin, R. McCray, *Ap. J.* **477**, 281–93 (1997).
28. K. J. Borkowski, J. M. Blondin, R. McCray, *Ap. J.* **476**, L31–L34 (1997).
29. R. P. Drake et al., *Ap. J. Lett.* **500**, L157–L161 (1998).
30. R. P. Drake et al., *Phys. Rev. Lett.* **81**, 2068 (1998).
31. J. Kane, R. P. Drake, B. A. Remington, *Ap. J.* **511**, 335 (1999).
32. R. A. Chevalier, *Ap. J.* **258**, 790 (1982).
33. R. I. Klein et al., *Ap. J. Suppl.* (Apr. 2000), in press; and in preparation (1999).
34. R. Klein et al., *Ap. J.* **420**, 213 (1994).
35. J. M. Laming, J. C. Raymond, B. M. McLaughlin, and W. P. Blair, *Ap. J.* **472**, 267–74 (1996).
36. T. Ditmore et al., *Phys. Rev. Lett.* **78**, 2732–5 (1997); *ibid.*, **78**, 3121–4 (1997); *Nature* **386**, 54–6 (1997); *Ap. J. Suppl.* (Apr. 2000), in press.
37. G. S. Sarkisov et al., *JETP Lett.* **66**, 828 (1997).
38. S. Y. Chen et al., *Phys. Rev. Lett.* **80**, 2610 (1998).
39. K. Shigemori, T. R. Ditmore, T. Kuhl, and B. A. Remington, *Bull. Am. Phys. Soc.*, **43**, 1731 (1998), paper F3S38.
40. D. Ryutov et al., *Ap. J. Suppl.* (Apr. 2000), in press.
41. R. A. Chevalier, *Science* **276**, 1374 (1997); T. Suzuki and K. Nomoto, *Ap. J.* **455**, 658 (1995); C. Fransson et al., *ibid.* **461**, 993 (1996); J. M. Marcaide et al., *Science* **270**, 1475 (1995); R. A. Chevalier and C. Fransson, *Ap. J.* **420**, 268 (1994).
42. J. C. Bozier, J. P. Le Breton, et al., *Phys. Rev. Lett.* **57**, 1304 (1986).
43. T. Afshar-rad et al., *Phys. Rev. Lett.* **73**, 74 (1994).
44. D. Hoarty et al., *Phys. Rev. Lett.* **78**, 3322 (1997).
45. Tsvi Piran, in *Unsolved Problems in Astrophysics*, by John N. Bahcall and Jeremiah P. Ostriker (Princeton University Press, Princeton, New Jersey, 1997), pp. 343–369.
46. G. J. Fishman and C. A. Megan, in *Ann. Rev. Astron. Astrophys.* **33**, 415 (1995).
47. E. Waxman, *Ap. J.* **489**, L33 (1997).
48. E. Waxman, *Ap. J. Suppl.* (Apr. 2000), in press.
49. J. H. Krolick and E. A. Pier, *Ap. J.* **373**, 227 (1991).
50. E. Liang, M. Kusunose, I. A. Smith, A. Crider, *Ap. J.* **479**, L35–L38 (1997).
51. D. Farley et al., *Phys. Rev. Lett.* **83**, 1982 (1999).
52. M. H. Key et al., *Phys. Plasmas* **5**, 1966 (1998).
53. T. Cowan et al., in *Proc. of XXIV ECLIM*, to be published in *Lasers and Particle Beams* (1999); and in preparation for submittal to *PRL* (1999).
54. W. B. Hubbard et al., *Phys. Plasmas* **4**, 2011 (1997).
55. D. Saumon et al., *Phys. Rev. Lett.* **76**, 1240 (1996); *Ap. J.* **460**, 993 (1996).

56. T. Nakajima et al., *Nature* **378**, 463 (1995); B. R. Oppenheimer et al., *Science* **270**, 1478 (1995).
57. G. W. Collins et al., *Science* **281**, 1178 (1998); *Phys. Plasmas* **5**, 1864 (1998); L. B. Da Silva et al., *Phys. Rev. Lett.* **78**, 483–6 (1997).
58. S. T. Weir, A. C. Mitchell, and W. J. Nellis, *Phys. Rev. Lett.* **76**, 1860 (1996).
59. N. C. Holmes, M. Ross, and W. J. Nellis, *Phys. Rev. B* **52**, 15835 (1995).
60. W. J. Nellis, submitted to *J. Planetary and Space Sciences* (Sept. 1998).
61. W. J. Nellis, M. Ross, N. C. Holmes, *Science* **269**, 1249–52 (1995).
62. M. Koenig et al., *Ap. J. Suppl.* (Apr. 2000), in press; *Phys. Rev. Lett.* **74**, 2260 (1995).
63. A. Benuzzi et al., *Phys. Rev. E* **54**, 2162 (1996).
64. A. M. Evans et al., *Laser and Part. Beams* **14**, 113 (1996).
65. T. Lower et al., *Phys. Rev. Lett.* **80**, 4000 (1998); M. Basko et al., *Phys. Rev. E* **56**, 1019 (1997); T. A. Hall et al., *Phys. Rev. E* **55**, R6356 (1997).
66. T. Lower et al., *Phys. Rev. Lett.* **72**, 3186 (1994).
67. S. Fu et al., *Phys. Plasmas* **2**, 3461 (1995).

RADIATION TRANSPORT EXPERIMENTS ON THE OMEGA LASER

C. A. Back B. F. Lasinski M. D. Rosen

J. D. Bauer J. H. Hammer O. L. Landen

R. E. Turner L. J. Suter W. H. Hsing

Radiative heating is a significant driver in inertial confinement fusion (ICF) and some astrophysical phenomena. For instance, in indirect-drive ICF, radiation-hydrodynamic simulations must span the range from optically thin to thick transport.¹ A diffusive radiative wave approximation is found to describe the heating of Au hohlraum wall, which is important to the x-ray conversion efficiency of the target.^{2,3} A transitional region to ablative heating is found at the laser-driven ablative front where the interplay between radiation and complex hydrodynamics can produce ablation front motion that can affect x-ray symmetry on the capsule.⁴ Radiative heating can also play a role in detrimentally preheating the capsule fuel before compression.

A similar set of physics must be understood for Z-pinch driven fusion.⁵ In recent dynamic hohlraum schemes, the Z-pinch wire array implodes onto a foam that is initially optically thin but can become optically thick as the foam plasma collapses radially up to a factor of ~ 5 on-axis.⁶ Here the radiation drive that is emitted depends heavily on the axial and radial radiative transport inside the foam. Heavy-ion fusion schemes also depend on radiation transport where targets filled with high Z-doped foams absorb ions and also help thermalize the radiation.⁷⁻⁹

We have established a strong experimental program to investigate radiation physics using high-powered lasers. Radiation transport is also one of the main thrusts of the Stockpile Stewardship Program along with

hydrodynamics. Therefore the goal of the radiation transport experiments is to experimentally investigate the basic Marshak wave phenomena, concentrating on the propagation of supersonic heat waves in diffusive medium.

The experiments described here have been conducted over the last year and a half at the OMEGA facility in Rochester, New York. Experiments have been performed with both low-temperature long 12-ns radiation drives and shorter high-powered 2.4-ns drives. In all cases, the laser irradiates a hohlraum to produce x rays that radiatively heat a test sample. The samples were low-density SiO_2 or Ta_2O_5 foams with densities from 10 mg/cm^3 to 50 mg/cm^3 .

The OMEGA experiments obtain three types of measurements: (1) the radiation temperature T_r , (2) the time-resolved face-on radiation breakout, and (3) two-dimensional (2D) x-ray images of the breakout. For these experiments, the radiatively heated samples were cylindrically shaped foams with different lengths that enabled temporally and radially resolved measurements at different propagation lengths.

Scale-3 Low-Temperature Experiments

In the 12-ns-long experiments, the heated SiO_2 foams had an initial density of 10 mg/cm^3 . A constant 1.5-TW, 12-ns, 3ω laser drive pulse irradiated a Scale-3 hohlraum, 8 mm long and 4.8 mm in

diameter, to create a radiation environment very similar to those used in typical 2-ns flat-topped Scale-3 Nova experiments. Due to the target geometry and the beam positions, only 48 of the 60 OMEGA beams were used to create the radiation drive. The laser beams were staggered so that six sets of eight beams provided a constant intensity pulse. The 48 drive-beam positions were chosen for optimum azimuthal flux symmetry in the hohlraum. The radiation drive temperature history was predicted to peak at 80 eV at about 12 ns. Figure 1 shows a schematic of the target. This x-ray radiation drive indirectly heated the aerogel foam (SiO_2) cylinder mounted on the side of the hohlraum. Other beams illuminating the outside of the hohlraum on the top and bottom of the foam support tube provided timing fiducials, while a 75- μm wire provided a spatial fiducial across an imaging slit on the external foam face where breakout of the radiation wave is measured.

The SiO_2 foam sample was cast into a 25- μm -thick Au ring that provided mechanical support. The outside face of the foam cylinder was masked by Mylar to form a 300- μm -wide slit in order to define the area of foam viewed by the diagnostics. The samples were fabricated in a 3-mm-diameter ring, a support tube as wide as possible, given the foam fragility, hohlraum size, and radiation drive, to obtain a radiation wave that was as planar as practical. The support rings were four different lengths: 0.5, 1.0, 1.5, and 2.0 mm. The radiation wave propagates axially down the cylindrical foam and breaks out of the exterior face. Thus, the different lengths permit direct comparisons with simulations over a range of radiative propagation lengths.

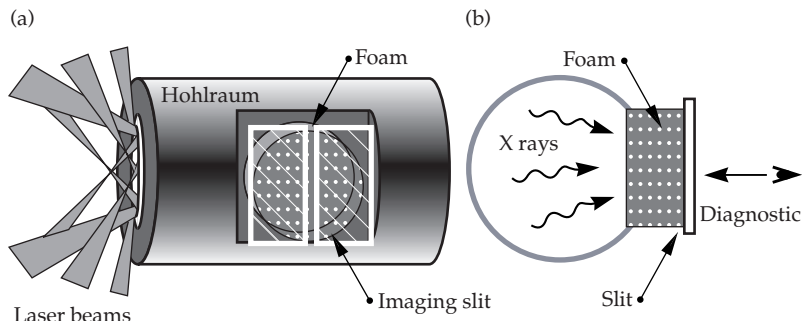
The primary diagnostic measured the emission breakout of radiation from a face-on view. A 2000- \AA -period Au transmission grating spectrometer coupled to an x-ray streak camera detects the foam emission. It viewed the exterior face and was oriented to spatially resolve the strip of foam defined by a Mylar slit. In the 3.0-mm-long vertical dimension of the slit, the spatial resolution was 80 μm while in the horizontal dimension it integrated over 300 μm . Inside the diagnostic, an internal slit was positioned after the x rays are dispersed by the grating to select photon energies of 250 eV with a spectral bandwidth of ~ 10 eV. A 5- μm parylene-n filter reduced the grating response in second order to 2×10^{-3} of first order. The spectral energy band centered at 250 eV was selected to match the Rosseland mean photon energy at $\sim 4T_r$.

Dante, the filtered x-ray diode array, measures the actual radiation drive inside of the hohlraum. The laser power was lower than expected and the actual peak drive temperature was ~ 75 eV instead of 80 eV. This measured drive was input to large-scale 2D simulations to calculate breakout times and intensity profiles.

The streaked x-ray imager (SXI) data from different length hohlraums are high quality and have both spatial and timing fiducials. The breakout is clear and Figure 2 shows an image as a function of time and space. The data show that the radiation wave takes about 2 ns longer to burn through at the edges of a 3-mm-diameter foam than at the center, so the radiation front is "bowed." Its curvature becomes more pronounced on longer foam lengths. The soft x-ray framing camera (SXRFC) instrument provided the 2D x-ray images

FIGURE 1. Schematic of hohlraum with foam mounted on the side. The side view is shown in (a) with the laser beam illumination through the LEH. A cross-section view in (b) shows the radiation from the cavity heating the foam.

(08-00-0300-0768pb01)



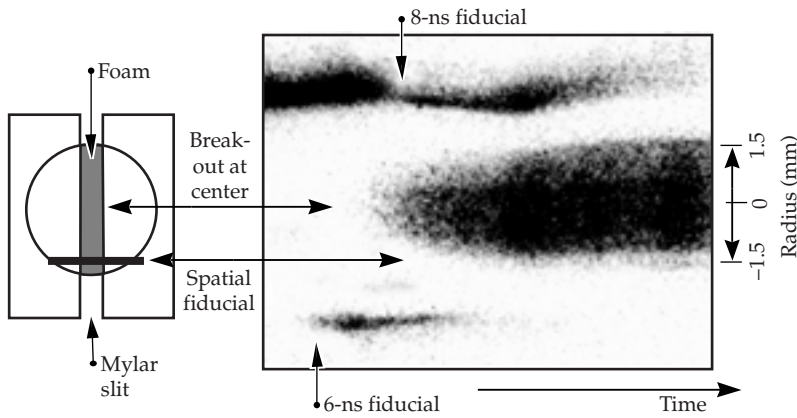


FIGURE 2. Diagnostic view of foam sample and example of data. The foam emission is spatially imaged in the vertical direction and integrated over the slit width. On the data, emission appears black and the horizontal axis represents time. Timing fiducials are x-ray signals created by laser beams irradiating the outside of the hohlraum body. (08-00-0300-0769pb01)

that were used to corroborate the streaked radial SXI intensity profiles.

Comparisons with simulations using OPAL¹⁰ to model the foam opacity show good agreement between these data and simulations of the intensity as a function of time for three different lengths of foam. The breakout times at the center are 3.8 ns, 6.7 ns, and 11.1 ns for the 0.5-, 1.0-, and 1.5-mm-long foams respectively, and the intensity lineouts are shown by dotted lines in Figure 3 along with those calculated by the simulations using the measured T_r shown by solid lines. No breakout signal was detected within the 18-ns temporal window of the instrument for the 2-mm-long foam. The breakout times are measured to high accuracy because of timing fiducials

recorded simultaneously on the film. The timing error is 3%, 3%, and 5% for the 0.5-, 1.0-, and 1.5-mm-long foams, respectively.

Postprocessing of the signal was also performed to predict the radial curvature and explore some other aspects of the foam targets. It is clear from Figure 4 that the data agree more closely to the simulations using the detailed OPAL opacity model. These detailed calculations are qualitatively different than those produced using an average atom model, XSN,¹¹ for the following reason. Although the Rosseland mean photon energy determines the radiation heat wave propagation, the measured intensity profile is determined by the opacity at the measured photon energy, which may be more highly dependent on the opacity model. At this

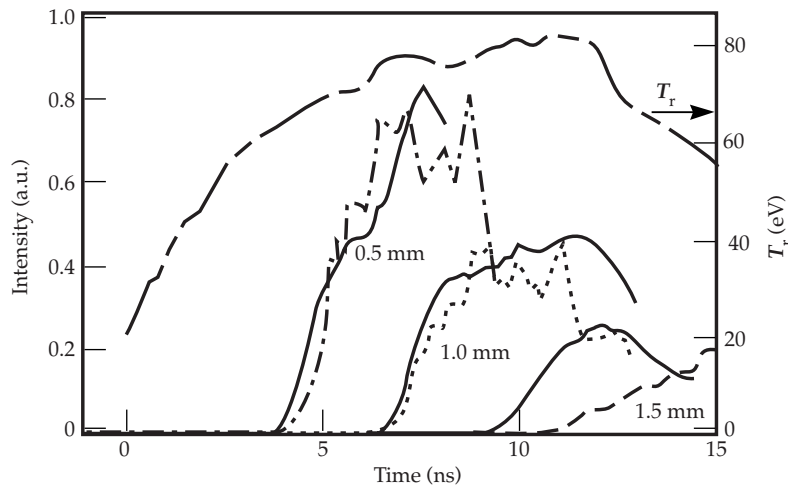


FIGURE 3. Intensity vs time lineouts at foam center for three different-length foams. Dashed lines show data; solid lines show calculations. The measured radiation-drive temperature is plotted along the right-hand axis. (08-00-0300-0770pb01)

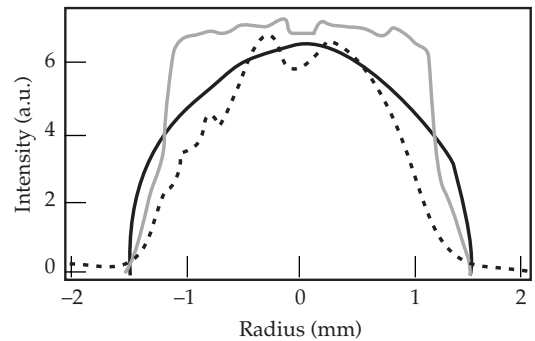


FIGURE 4. An example of radial lineouts at 9.5 ns after the x-ray drive starts. The dashed lines are the data, the solid line is the calculation using OPAL model for the SiO_2 , and the gray line is the calculation using an average atom model, XSN. (08-00-0300-0771pb01)

measured photon energy of $h\nu = 250$ eV, the $n = 2-3$ transitions in oxygen and silicon dominate, and an average atom model is inadequate. A comparison in Figure 5 of the temperature-dependent opacity of two models show differences up to an order of magnitude in the opacity at $h\nu = 250$ eV as the temperature in the radiation front varies between 40 to 80 eV. This difference produces drastically different radially resolved emission patterns. By contrast, the Rosseland mean opacity is virtually the same for the two opacity models at 60 eV, and 60% higher than the average atom opacity at 40 eV. The choice of the opacity model only affects the breakout times by $\sim 15\%$ because they depend on mean values, i.e., the Rosseland mean opacity averaged over a rising temperature profile. The radial intensity profile, however, is dependent on the opacity model at a particular photon energy and hence can be radically affected.

These 12-ns experiments were the first to implement the suite of instruments described above to measure radiation heating in a supersonic regime.¹² This regime is important because the radiation wave velocity is greater than the sound speed in the material and therefore effects due to radiative heating can be isolated from hydrodynamic perturbations. These experiments demonstrated the robustness of the experimental technique because the measured signal was unambiguous and had a good signal-to-noise ratio. However, it also revealed some pitfalls in modeling radiation transport experiments that we

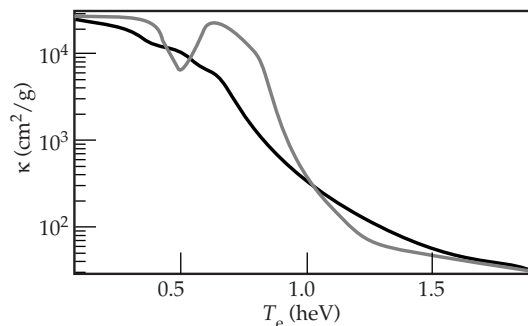


FIGURE 5. The SiO_2 opacities at the measured photon energy of 250 eV calculated by OPAL (solid line) and XSN (gray line) over the range of temperatures valid for the 12-ns experiments. The discontinuous drop in opacity between temperatures in the range of 40 to 60 eV is an artifact of the average atom model calculations and is not correct. (08-00-0300-0772pb01)

have addressed in subsequent half-hohlraum experiments.

The first was the opacity sensitivity, which led to a greater scrutiny of the opacity model, and how it was incorporated into the simulations. Simulations performed with XSN, an average atom model were compared with simulations using the OPAL model, a detailed atomic model. We expected differences in the breakout time predicted from the two because this quantity depends on the Rosseland mean opacity calculated by the model. However, we were surprised to find that the two also produced qualitatively different radial profiles. This sensitivity has led to much stricter attention to the opacity model and its frequency grid in subsequent simulations.

Second, the experimental geometry we used made it difficult to directly incorporate the measured radiation drive into 2D simulations of the hohlraum and foam. In the Scale-3 geometry discussed above, the foam was mounted on the side of the hohlraum. This geometry is inherently 3D because the inner Au hohlraum wall is both directly and indirectly heated by the lasers. Unfortunately matching the source heating on the foam could not reflect this experimental detail. The drive measurement by the Dante x-ray diodes only samples the indirectly heated Au wall; therefore, simply making the inner wall of a 2D simulation radiate at the measured T_r does not properly reflect the contribution of the directly heated wall. Although we are able to compensate for this ambiguity, we concluded that decoupling the radiation modeling of the foam from the deposition of the laser energy needed to heat the hohlraum would always present this difficulty.

Half-Hohlraum Axisymmetric Experiments

To improve comparison with simulations, experiments conducted in 1999 used a different geometry that was axisymmetric and enabled integrated modeling of the entire target with the 2D radiation hydrodynamics code LASNEX. In this geometry, we used a Scale-1 half-hohlraum 1.6 mm in diameter and 1.2 mm long. Figure 6 shows a schematic of the target. Only half

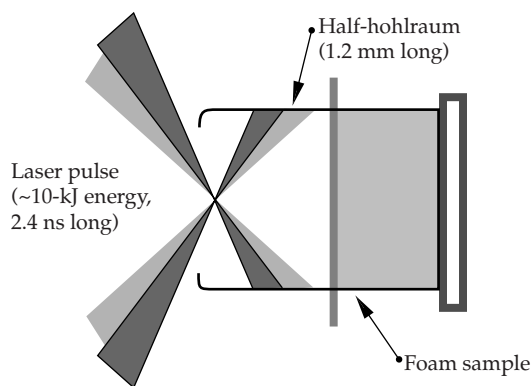


FIGURE 6. Schematic of the half-hohlraum target and foam. (08-00-0300-0773pb01)

the number of beams typically heating a full-sized hohlraum enter the left side of the hohlraum through a 1.2-mm-diameter laser entrance hole (LEH). The aerogel foam sample under investigation is a cylinder of the same diameter as the hohlraum, placed opposite the LEH. The radiation propagates down the axis of the hohlraum and breaks out of the side opposite the laser beams.

In this configuration, we used a stepped laser pulse that was ~ 5.8 TW for the first 1.2 ns and dropped to 2.2 TW in the following second 1.2 ns. This pulse was designed to produce a radiation temperature that rises to ~ 190 eV in the first half of the pulse and plateaus in the second half. Two types of denser foams were used to accommodate the higher temperature and also to maximize the number of mean free paths in the heated foam sample. These were SiO_2 at 50 mg/cm^3 and Ta_2O_5 at 40 mg/cm^3 . As before, we used multiple lengths of foams in order to sample the breakout time of the radiation wave through different propagation lengths.

Samples of Ta_2O_5 were 0.25, 0.50, 0.75, and 1.00 mm long, while SiO_2 samples were 0.50, 1.00, and 1.25 mm long. The shortest lengths corresponded to ~ 1 mean free path (MFP) of the heated material, and the longest length was determined by the maximum distance we were able to propagate while the laser pulse was still on, ~ 3.8 MFPs for Ta_2O_5 and 1.7 MFPs for SiO_2 . Measurements at late times after the laser pulse is off are often complicated by plasma filling followed by stagnation of the ablated plasma and do not provide definite quantitative data.

The principal diagnostic, the SXI, was the same as that used in the 12-ns experiments. It imaged the 1.6-mm vertical dimension and integrated over the $300\text{-}\mu\text{m}$ Mylar slit width in the temporal dimension of the data. However, this time it was configured to measure a spectral bandwidth ~ 50 eV, centered at $h\nu = 550$ eV, which is near the Rosseland mean energy of the radiation drive. Secondary diagnostics included photoconductive diodes to measure the radiation drive flux through the LEH and a gated imager to provide 2D x-ray images of the foam breakout.

The measurements by photoconductive diodes rise to the same peak radiation temperature as predicted by calculations. However, the rise time to the peak temperature is slower than predicted, and during the second half of the pulse the T_r tends to have a slight negative slope instead of remaining constant. These early time hohlraum radiation temperature calculations typically have a larger error bar, probably because establishing the T_r in the enclosure depends more crucially on the low-temperature albedo during this time. We will be investigating details of the drive in upcoming shots. However, for the purposes of radiation transport in the foam, we corrected for the lower measured drive in comparisons of the calculated radiation breakout with the data.

The calculations predict a radiation-wave curvature in the foams that depends on the axial and radial Rosseland MFPs in the heated foam sample. In Figure 7, we show a series of data from the 40-mg/cm^3 Ta_2O_5 foams 0.25 to 1.0 mm long. Here we span 1.2 to 3.8 MFPs in the foam from the shortest to longest foam, and we measure progressively more curved data images. In the shortest foam, the flat radiation front results from the fact that the foam is ~ 1 optical depth and therefore the flat front reflects the uniformity of the external source radiation provided the hohlraum. For the longer foams, the energy lost to the walls reduces the heating of the foam at the edges and causes a retardation in the radiation breakout at the edges. For the 0.75-mm-long foam, the edges break out nearly 1 ns later than in the center.

The propagation distance of the radiation versus time is modeled to within 10% by the simulations. These are shown in

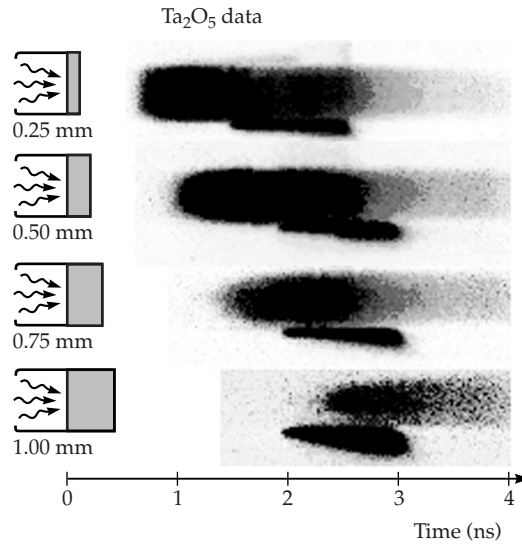


FIGURE 7. Images of the series of Ta_2O_5 data. Four different lengths span a range of 1.2 to 3.8 mean free paths. The radiation front breakout seen at the left-hand side of the data becomes more curved for longer lengths as the energy lost to the wall becomes more significant. (08-00-0300-0774pb01)

Figure 8 for the Ta_2O_5 and the SiO_2 foams where the solid lines are the calculations. The peak heights of the temporal breakout signals match the data quite well. The peak emission out of the unirradiated side of the foam depends on the foam fill and will decrease with distance for a diffusive medium. Therefore, the good intensity match of the breakout signal is significant because it indicates that the relative fluxes predicted by the simulations drop in magnitude consistently with the measured signals, even though we do not have an independent temperature measurement.

The radial emission profiles can also be analyzed in detail. In these data we measure a temperature gradient in the foam that depends on the radial MFPs of the foam material. For the SiO_2 , which has a radial MFP ~ 1.1 , the intensity profile half-maximum intensity is at ~ 0.6 mm from the center, whereas the Ta_2O_5 is nearly a factor of 2 smaller. The data also allows an inference of radial temperatures that are in relatively good agreement with calculations. The detailed behavior of the emission intensity as a function of time is also in progress, and preliminary comparisons show very good agreement of the relative intensity between the different-length foams.

Summary

These experiments have conclusively demonstrated diffusive supersonic radiative heating of low-density foam materials. The shape of the radiation wave, as witnessed by the breakout, is dependent on a combination of the foam and wall material properties. We are using the results of single-foam experiments described here as the control data set in order to better understand more complicated sample foam geometries. These experiments demonstrate that it is important to heat as large a sample as possible with

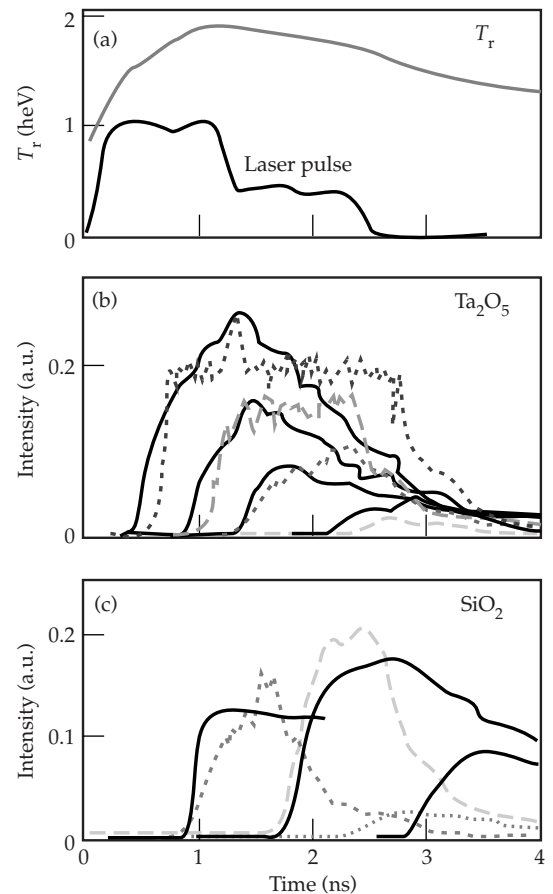


FIGURE 8. (a) The measured radiation drive temperature history is plotted along with the normalized laser pulse. (b) Temporal intensity lineouts of the Ta_2O_5 data at foam center. Dashed lines show data; solid lines show calculations. Each pair corresponds to a different-length foam: 0.25 mm, 0.50 mm, 0.75 mm, and 1.00 mm. (c) Temporal intensity lineouts of the SiO_2 data at foam center. Dashed lines show data; solid lines show calculations. Foam lengths were 0.5 mm, 1.0 mm, and 1.25 mm. (08-00-0300-0775pb01)

high-energy facilities, such as the OMEGA laser, to be able to distinguish between 1 and 2D effects. We are continuing to develop systematic studies of radiation propagation for future radiation experiments.

Acknowledgments

The authors would like to thank the OMEGA laser crew, LLNL technical support, and the LLNL target fabrication team members, particularly M. Spragge and H. Louis. We also thank the crew at the Nova laser where some preliminary shots were performed.

Notes and References

1. J. Lindl, *Phys. Plasmas* **2**, 3933 (1995); J. Lindl, *Inertial Confinement Fusion* (AIP, New York, 1998).
2. R. Sigel, K. Eidmann, F. Lavarenne, and R. F. Schmalz, *Phys. Fluids B* **2**, 199 (1990); K. Eidmann, R. F. Schmalz, and R. Sigel, *Phys. Fluids B* **2**, 208 (1990).
3. R. L. Kauffman, L. J. Suter, C. B. Darrow, J. D. Kilkenny, H. N. Kornblum, D. S. Montgomery, D. W. Phillion, M. D. Rosen, A. R. Theissen, R. J. Wallace, and F. Ze, *Phys. Rev. Lett.* **73**, 2320 (1994).
4. R. Pakula and R. Sigel, *Phys. Fluids* **28**, 232 (1985); J. Meyer-Ter-Vehn, R. Pakula, R. Sigel, and K. Unterseer, *Phys. Lett.* **104**, 410 (1984); N. Kaiser, J. Meyer-ter-Vehn, and R. Sigel, *Phys. Fluids B* **1**, 1747 (1989); R. Sigel, K. Eidmann, F. Lavarenne, and R. F. Schmalz, *Phys. Fluids B* **2**, 199 (1990); K. Eidmann, R. F. Schmalz, and R. Sigel, *Phys. Fluids B* **2**, 208 (1990).
5. M. K. Matzen, *Phys. Plasmas* **4**, 1519 (1997).
6. R. J. Leeper, T. E. Alberts, J. R. Asay, et al., *Nuc. Fusion* **39**, 1283 (1999); T. J. Nash, M. S. Derzon, G. A. Chandler, R. Leeper, et al., *Phys. Plasmas* **6**, 2023 (1999).
7. M. M. Basko and J. Meyer-ter-Vehn, *Nucl. Fusion* **33**, 601 (1993); M. M. Basko, *Phys. Fluids B* **4**, 3753 (1992).
8. D. A. Callahan-Miller and M. Tabak, *Nuc. Fusion* **39**, 883 (1999); G. O. Allshouse, R. E. Olsen, D. A. Callahan-Miller, and M. Tabak, *Nuc. Fusion* **39**, 893.
9. M. S. Derzon, G. A. Chandler, R. J. Dukart, et al., *Phys. Rev. Lett.* **76**, 435 (1996).
10. F. J. Rogers and C. A. Iglesias, *Ap. J. Suppl.* **79**, 507 (1992).
11. W. A. Lokke and W. H. Grasberger, Lawrence Livermore National Laboratory Report No. UCRL-52276 (1977), unpublished.
12. C. A. Back, J. D. Bauer, O. L. Landen, R. E. Turner, B. F. Lasinski, J. H. Hammer, M. D. Rosen, L. J. Suter, and W. H. Hsing, *Phys. Rev. Lett.* **84**, 274 (2000).

A NEW LASER-DRIVEN SOURCE FOR STUDYING RADIATION HYDRODYNAMIC PHENOMENA

J. Edwards

O. Landen

K. Budil

R. Wallace

S. G. Glendinning

R. E. Turner

H. Robey

*P. Graham**

L. J. Suter

T. J. Shepard

J. Kane

*M. Dunne**

B. A. Remington

B. Lasinski

H. Lewis

*B. R. Thomas**

At Lawrence Livermore National Laboratory (LLNL) we are developing a new laser-driven source for studying radiation hydrodynamics phenomena. The source generically consists of half a hohlraum driven by laser beams from one end. The opposite end of the hohlraum is filled with a low-density, typically CH, foam. Quasi-thermal soft x rays from the hohlraum supersonically heat the foam, which can then be used to drive a payload. Such a source potentially has applications in many fields, including equation of state, opacity (for which a double-ended design may be more applicable), hydrodynamic instabilities, and the properties of turbulent flows. In this article, we describe the application of the source in initial experiments on the Nova laser to study the growth of a mixing layer driven by classical turbulent Rayleigh–Taylor (RT) instability.¹ This new source has advantages over other laser-driven systems in that the acceleration can be almost shockless, reducing complications from any additional shock-driven Richtmyer–Meshkov (RM) instability growth,² and there is no unstable ablation front to influence the mixing region. Understanding these instabilities is important for interpreting numerous natural phenomena. For example, the RM and RT instabilities are expected to be very important in drawing out core material into the outer layers of a star during the explosion phase of a supernova, and then later for

disrupting the thin shell remnant as it plows into the ambient interstellar medium.^{3–9}

Instability growth during the explosion phase is thought to be significantly influenced by an initial seed provided by convection cells deep within the star.⁸ Thus the issues that need to be addressed in these situations are mixing due to turbulence, the effects of initial conditions, and thin layers. It will be possible to address these issues with the new source.

Rayleigh–Taylor Instability and Laser Experiments

The RT instability occurs at the interface between two fluids when a light fluid of density ρ_1 tries to support a heavy fluid of density ρ_2 in a gravitational field. Perturbations at the interface grow rapidly generating a 3D turbulent mixing region in which “bubbles” of light fluid rise into the heavier fluid, while “spikes” of heavy fluid fall into the lighter fluid. After memory of the initial conditions has been lost, the advance of the bubble and spike fronts is expected to enter a self-similar regime in which the growth is given by $h_{b(s)} = \alpha_{b(s)} A g t^2$ where $h_{b(s)}$ is the bubble (spike) height, $\alpha_{b(s)}$ a constant, $A = (\rho_2 - \rho_1)/(\rho_1 + \rho_2)$ the Atwood number, g the gravity (acceleration), and t time. Incompressible 3D simulations predict α (from here, α refers to the bubbles) ≈ 0.028 [Ref. 10], bubble merger models typically predict $\alpha \approx 0.05$ [Ref. 11], while others suggest α is

*Atomic Weapons Establishment plc, RG7 4PR, UK

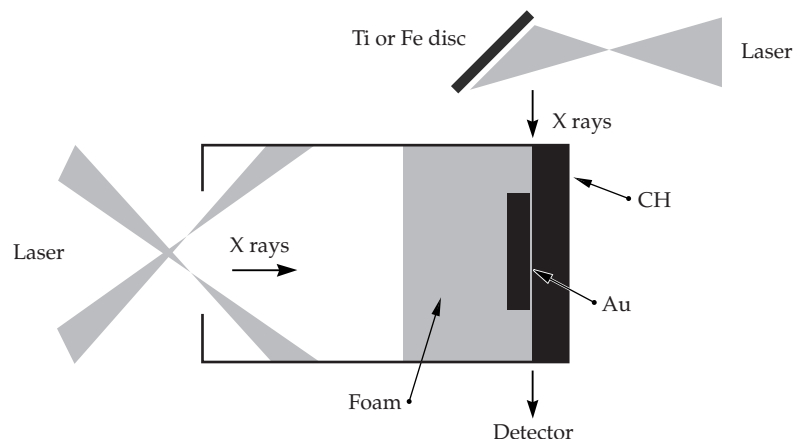
a function of compressibility.¹² Incompressible experiments find $\alpha \sim 0.06$ [Ref. 13] but vary from ~ 0.05 to ~ 0.075 [Ref. 14], and there are no compressible experiments. The apparent discrepancy between incompressible simulations and experiment is possibly due to a memory of an uncharacterized initial condition (perhaps due to vibration) promoting growth above the self-similar limit seen in the simulations, while the effects of compressibility remain not well established. New experiments are therefore desirable, and laser experiments have some attractive features. Solid targets allow initial conditions to be precisely controlled and measured; high-energy densities promote experiments into the compressible plasma regime; and a broad range of Atwood numbers and acceleration profiles are feasible. Added to these, laser drivers also have the attractive ability to readily tailor the drive history so that reasonably scaled versions of the plasma profiles in a supernova explosion, for example, can be obtained.⁷ These attractive features notwithstanding, the challenge for laser experiments in the turbulent regime has always been diagnosing the small scales involved. This new method clearly demonstrates an ability to begin to measure the growth of mixing regions on current facilities. Coupled with the advance of x-ray diagnostics, target fabrication techniques, and the prospect of the National Ignition Facility increasing the scale of experiments an order of magnitude, this makes it increasingly attractive to develop methods of studying hydrodynamic instabilities using lasers.

Experiment

The driver for the experiments was half a Scale 1 gold Nova hohlraum, 1.25 mm long by 1.6 mm diameter with a 50% laser entrance hole (LEH) (see Figure 1). This arrangement allows for a wider experimental package than the usual double-ended design, without any loss in performance, and has the additional advantage of being amenable to integrated simulation using 2D hydrocodes. The experimental package was mounted at the open end of the hohlraum and consisted of a short gold tube of the same diameter as the hohlraum containing a low-density $\sim 0.15\text{-g/cm}^3$ CH foam. A payload completed the package and consisted of a 1-mm-diam, $1/2\text{-}\mu\text{m}$ -thick gold disc supported centrally on a $10\text{-}\mu\text{m}$ -thick CH foil, which spanned the diameter of the tube. Five Nova beams delivered ~ 11 kJ of $0.35\text{-}\mu\text{m}$ laser light to the hohlraum in a square, 1-ns pulse raising the internal radiation temperature to ~ 200 eV. The quasi-thermal radiation was used to supersonically heat and pressurize the foam, which then accelerated the payload.

The payload dynamics were diagnosed using side-on x-ray backlighting, with photon energies selected to preferentially show up the gold layer, but which also allowed the CH foil to be detected. The x rays were K-shell emission from either an Fe (~ 6.7 keV) or Ti (~ 5 keV) disk irradiated by two temporally separated laser pulses of 1-ns and 2-ns duration respectively, with the first pulse timed to coincide with the start of the main heating

FIGURE 1. Schematic of the experimental setup. (50-00-1299-2761pb01)



beams. Each of the two backlighter laser beams used a random phase plate to ensure a smoothly varying x-ray spatial emission over ~ 1 mm diameter. The typical intensity for each pulse at the backlighter disc was ~ 1 to 2×10^{14} W cm $^{-2}$. The x rays passing through the target were imaged with a 10- μ m-wide slit onto an x-ray streak camera with a total magnification of ~ 30 . The temporal and spatial resolutions in the target plane were 100 ps and 12 μ m respectively. This provided a continuous record of both the trajectory and width of the gold layer. This data was complemented on separate shots by using a gated x-ray imager to provide 2D spatial information at discrete times throughout the duration of the backlighter pulses. A 4×4 array of 10- μ m pinholes was used to image the target onto four strips of a gated x-ray microchannel plate with a total magnification of either ~ 4 or ~ 8 . These were particularly important both to corroborate the streak data and to demonstrate that edge effects did not compromise the experiment.

The radiation environment in the hohlraum was diagnosed using diamond photoconductive detectors viewing at 22° to the hohlraum axis. These were used to measure the radiation flux emerging from the LEH on a shot with foam and payload. On separate shots, the radiation flux emitted from the open end of the hohlraum, both with and without the foam (but no payload), was also measured. These data were then used together with 2D radiation hydrocode simulations and 3D view factor simulations to help constrain the drive on the experimental package and has been described elsewhere.¹⁵

Target Dynamics

Foam Driver

The driver and payload dynamics are described with the aid of Figure 2. By tailoring the laser pulse and target specifications, it is possible to generate a variety of

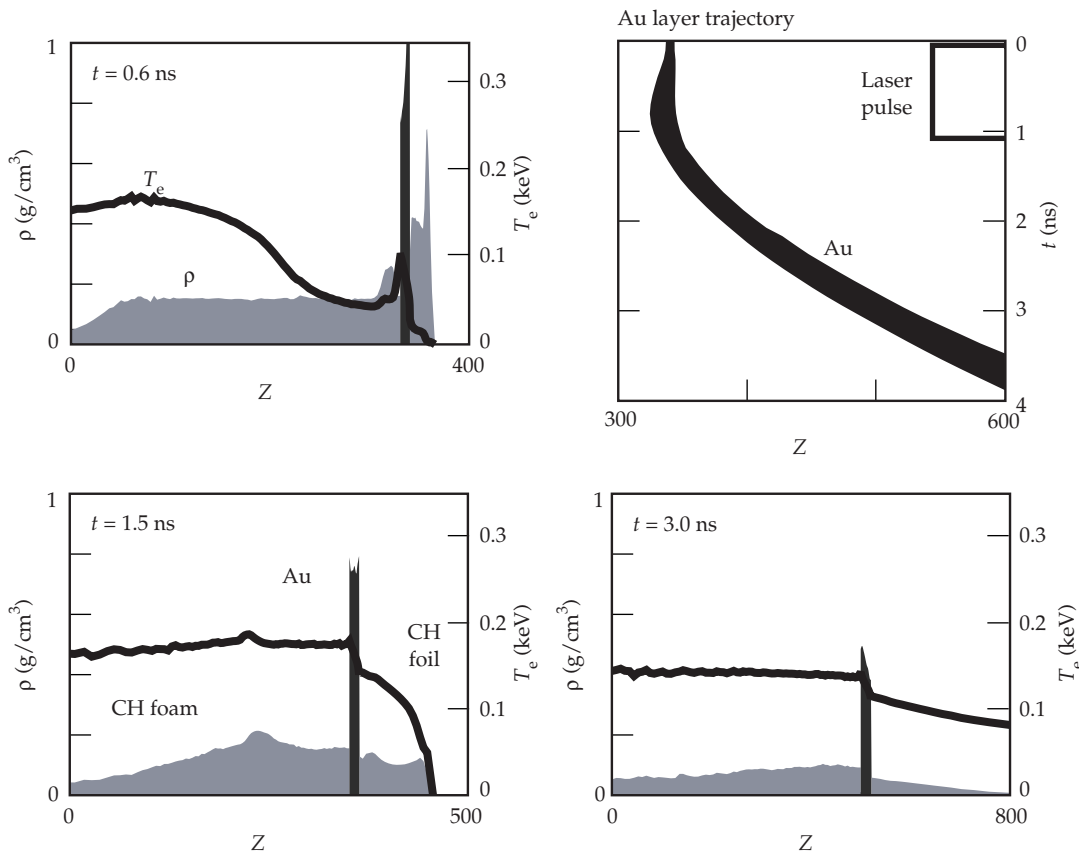


FIGURE 2. Density and temperature profiles predicted by the 1D hydrocode HYADES at selected times. The Au layer trajectory is also shown. (50-00-1299-2762pb01)

acceleration histories and introduce shocks of varying strengths if required. In these experiments, to avoid significant compression of the foam as the supersonic wave propagates, the radiation flow Mach number M_R , defined as the speed of the wave divided by the sound speed, must be ≥ 3 . For the ~ 200 -eV driver this placed an upper limit on the foam density ~ 0.15 g/cm³, corresponding to a pressure ~ 15 – 20 Mbar. The length of the foam, $L \sim 300$ μ m, was tuned so that the radiation wave arrived at the payload at t_B (burn-through time) towards the end of the laser pulse. A rarefaction follows the supersonic front into the foam at the sound speed, which in this case is $c \sim 100$ μ m/ns. This would eventually release the foam pressure at the payload and end the acceleration phase on a time scale $\sim L/c$ after the start of the laser pulse ($L/c - t_B$ after the start of the acceleration), or about 3 ns for these conditions. The fact that the payload is accelerating lengthens this but also causes a natural reduction in the “piston” pressure with time so that, in practice, the effective acceleration phase is still over by $t \sim 3$ ns. The parameters selected for this experiment maximize target acceleration.

Payload Dynamics

During foam burn-through, gold M-band x rays (photon energy ~ 2.5 keV) from plasma directly heated by laser light preheat the package, but are mostly stopped in the gold. This causes the $1/2$ - μ m layer to expand to ~ 20 μ m, dropping its density from 19 g/cm³ to $\sim 1/2$ g/cm³ by the time the radiation arrives. As a result, a weak compression wave runs a short distance into both the CH support and the foam, raising its density slightly to ~ 0.2 g/cm³. Once the radiation wave reaches the now low-density gold towards the end of the laser pulse, it rapidly burns through the layer raising its temperature to in excess of ~ 150 eV, on a time scale ~ 200 ps.¹⁶ The foam pressure is larger than the pressure in the hot gold causing a very weak shock ($M \sim 1.05$) to propagate through the gold. This shock is isothermal due to the strong radiation field and takes the form of a 1.3 – $1.5\times$ compression “pulse” that traverses the Au layer in around 200 ps, but

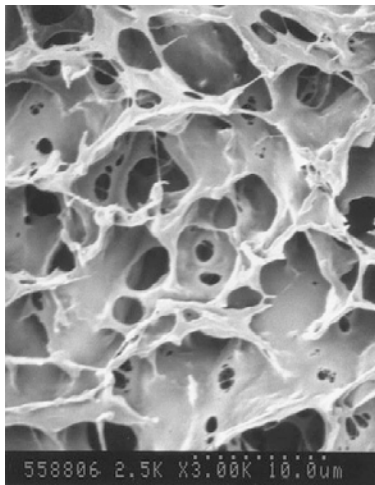
leaves the width of the layer virtually unchanged. Radiation leaking through the gold drives a weak, subsonic ablation wave, preceded by a shock wave, into the CH. After the shock hits the free surface and the rarefaction subsequently reflected returns to the gold, the entire payload begins to accelerate smoothly under the influence of the hot foam. Classical RT instability then develops at the interface between the hot gold and foam plasmas where the Atwood number is ~ 0.7 .

Instability Seed

The seed for the instability was provided by the intrinsic discrete random structure of the foam. Figure 3 shows scanning electron microscopy (SEM) pictures at different spatial scales of two foams used in these experiments. The TPX foam consists of a 3D honeycomb-like structure with a typical element size ~ 5 – 10 μ m and walls microns thick. The carbonized resorcinol foam on the other hand has an extremely fine intrinsic submicron structure. After machining, however, a 3D pseudo random pattern with structures ~ 5 - μ m wavelength and a fraction of this in depth can be observed. The foam structure imprints onto the gold during the preheat phase when the gold and foam expand, thus providing the seed for the instability. Clearly it is expected that the TPX foam will provide a very much larger seed than the resorcinol foam and therefore advance the growth of the mix region more rapidly at early time.

Experimental Results

A typical streak record obtained using an Fe backlighter is shown in Figure 4. For this shot, the foam density was 0.15 g/cm³ and its length was 230 μ m. To compensate for the slightly shorter foam length the laser energy was reduced to 7 kJ, for which the payload trajectory was calculated to be approximately equivalent to that for a nominal length foam (300 μ m) driven at full energy (~ 11 kJ). The foam itself was TPX of the type shown in Figure 3 with a typical pore size of 5–10 μ m. The shadow of the gold layer can be easily seen to move and grow with time. The initial



10 μm



10 μm

FIGURE 3. Series of SEM images of the surface of a TPX (left) and carbonized resorcinol (CR) foam. TPX has a 5- to 10- μm pore structure, while the intrinsic CR structure is submicron. Machining features with wavelengths $\sim 5 \mu\text{m}$ can be seen on the CR foam surface. (50-00-1299-2763pb01)

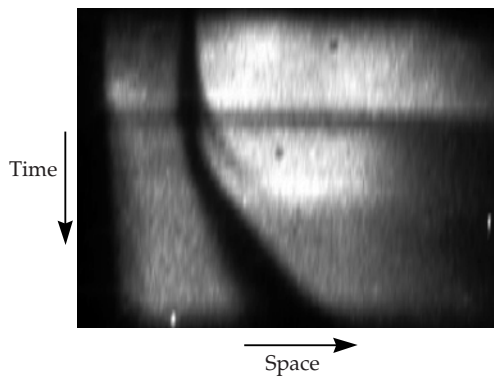


FIGURE 4. Streak record showing the backlit image of the Au layer trajectory (dark shadow). The shadow of the layer increases with time due to instability growth. A much weaker and narrower shadow due to the CH foil can be seen to move just ahead of the Au layer. (X rays incident from the left.) (50-00-1299-2764pb01)

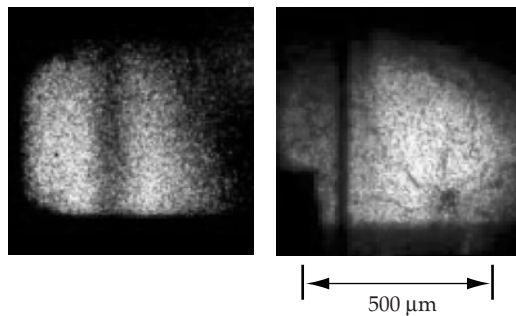


FIGURE 5. Comparison of GXI data obtained for the two different foams in Figure 3, but otherwise almost identical conditions. The Au layer is the dark vertical shadow and is much wider for the TPX foam (left). (50-00-1299-2765pb01)

width of the shadow, $\sim 25 \mu\text{m}$, is determined by a combination of parallax due to small alignment errors (equivalent to $\sim 1.5^\circ$ for $25\text{-}\mu\text{m}$ width) and instrument resolution. Less obvious, but nevertheless clearly visible, is the unablated portion of the CH foil moving just ahead of the gold layer. Very similar characteristics were seen in the gated images, which also showed that no gross distortions were present in the layer. Some very weak absorption features were observed at the edges but could be seen not to contribute significantly to the shadow at the center of the disc, making

the shadow a good diagnostic of the width of the layer.

Figure 5 compares gated x-ray imager (GXI) snapshots at 2.5 ns from two almost identical shots using the two different foams shown in Figure 4. What is striking is the substantial reduction in width as the initial seed is reduced.

Numerical Simulations

The experimental package was carefully designed to minimize deleterious effects such as large-scale curvature in the Au foil

as a result of drive nonuniformities or edge effects. This included detailed 2D radiation hydrodynamics code simulation and 3D view factor analysis.¹⁵ The simulations described here concentrate on the instability growth.

The data was simulated and analyzed using the 1D Lagrangian radiation hydrodynamics code, HYADES,¹⁷ and the 2D arbitrary Lagrangian Eulerian (ALE) radiation hydrocode CALE.¹⁸ HYADES employed a multigroup diffusion approximation to treat the radiation transport, with opacities derived from an in-line screened hydrogenic model. It was used extensively for parameter studies and to provide a 1D model consistent with the experimental data. CALE's ALE feature made it ideal for attempting to model the initial seed and the development of the instability. The modeling and approximations are discussed below.

1D Model

A particularly pleasing feature of the experimental design is that the trajectory of the CH foil is a very good diagnostic of the arrival of the radiation wave at the payload, which is a sensitive diagnostic of the drive, which in turn determines the acceleration. Furthermore, despite the instability in the gold layer, it appears from the CALE simulations that the leading edge of the gold is also a good diagnostic of the hohlraum drive, even for large seeds, at least to within the measurement uncertainty. Thus a baseline 1D model was set by tuning the hohlraum drive so as to reproduce approximately the experimentally measured trajectories of the leading edge of the gold layer and CH foil. The peak hohlraum drive temperature necessary to do this was close to 230 eV, which is consistent with detailed 2D radiation hydrocode simulation and 3D view factor calculations.¹⁵

It can be shown that, in the absence of instabilities, the width of the Au layer should be relatively insensitive to uncertainties in opacity and equation-of-state models, drive magnitude and preheat (due to hard

x rays).¹⁹ This has been borne out in an extensive suite of 1D simulations. This insensitivity is truly an attractive feature of this design, suggesting that for this particular experiment, the width of the layer should be a good indicator of instability growth.

2D CALE Simulations

CALE was used to help analyze the data, establish trends, and develop modeling techniques for these experiments, noting that in reality the flow is 3D. To model the foam in a more realistic fashion than the usual low-density homogeneous material approximation, the foam was treated as a collection of pseudo randomly distributed solid rods, separated by a typical pore size, sitting in a background of very-low-density material. The mean mass density of this "discrete solids" model was made equal to that of the foam $\sim 0.15 \text{ g/cm}^3$. For a typical pore size (separation) $\sim 5 \text{ }\mu\text{m}$, a single solid cylinder radius of $\sim 2 \text{ }\mu\text{m}$ was necessary. For practical reasons this technique is limited to relatively large pore sizes $\geq 2 \text{ }\mu\text{m}$. Below this, the usual low-density homogeneous material approach was used to approximate the foam. In this case, the seed was introduced as a surface perturbation. Although a simplified description of the radiation matter interaction was necessary to make the calculations tractable, care was taken to ensure that in 1D the CALE model was a good match to the 1D HYADES simulation.

An example of the evolution of a 50- μm -wide section of the target, representative of the dynamics away from the edges of the payload, is shown in Figure 6. The calculation used the discrete solids model for a 5- μm -pore-size foam with a mesh resolution of 0.25 μm , providing 8 cells across each solid foam "cylinder." Both the foam and Au can be seen to expand rapidly, imprinting an image of the foam structure on to the Au. As the payload accelerates, the perturbation develops into a mixing region exhibiting a bubble scale of the order of several initial wavelengths, characteristic of the beginnings of a turbulent flow.

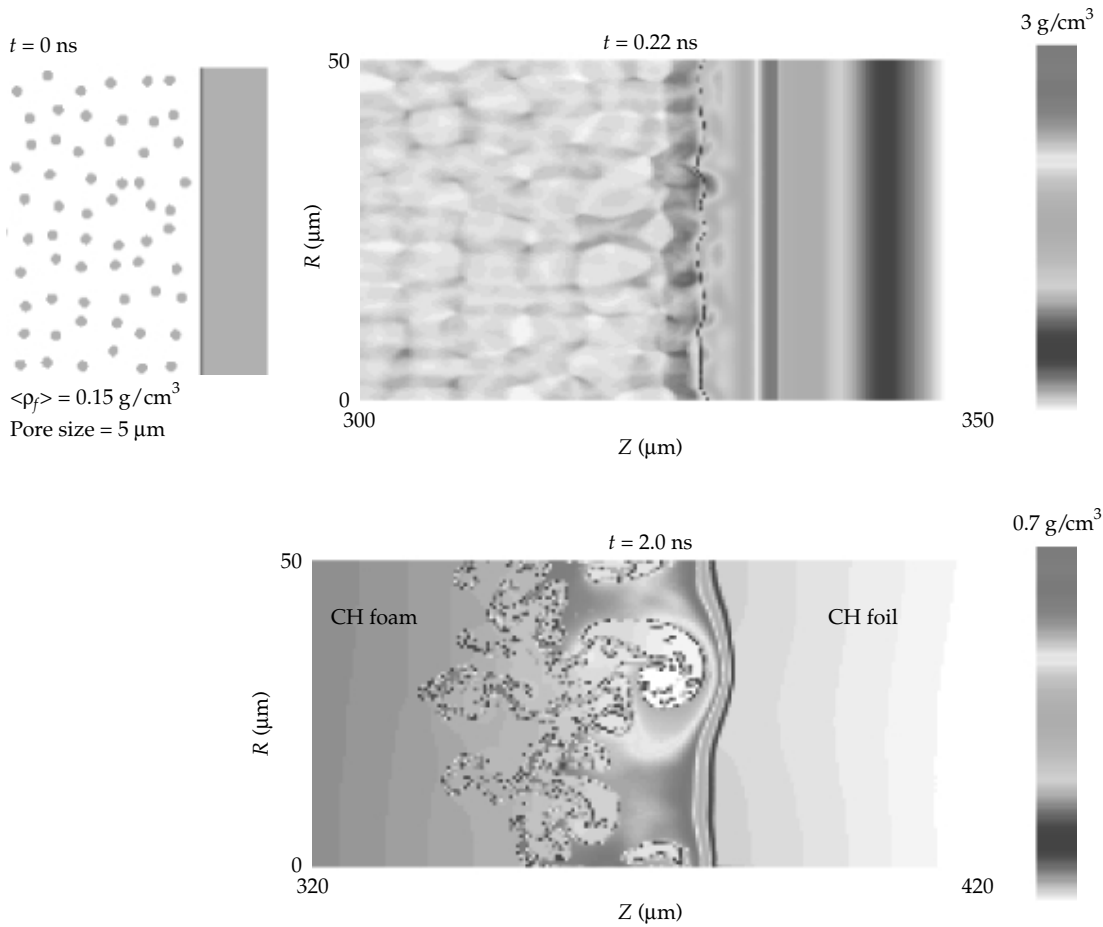


FIGURE 6. Time sequence of density maps from CALE illustrating seeding and growth of instability from foam structure with a pore size $\sim 5 \mu\text{m}$. (50-00-1299-2766pb01)

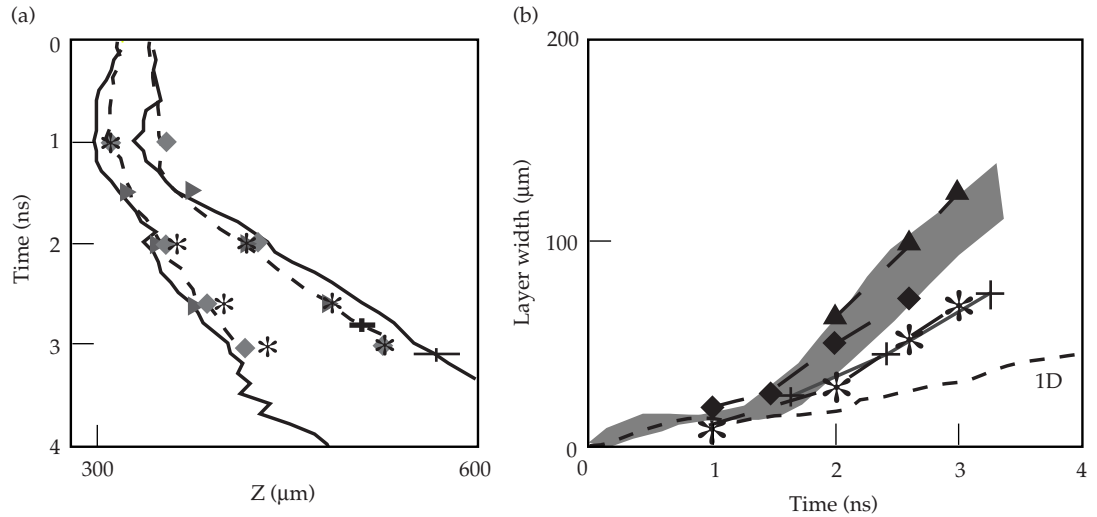
Comparison with Experiment

The predicted width and trajectory of the Au layer are compared against experiment as a function of time in Figure 7. In all the experiments, the width of the layer is measured to be significantly greater than that predicted by 1D HYADES. The correlation between the substantial reduction in layer width and initial seed is striking, strongly suggesting RT instability as the principal cause, and not curvature or edge effects. CALE appears to reproduce the trends in the experimental data rather well despite the 3D, turbulent nature of the flow.

Discussion

The above analysis provides a good qualitative and quantitative understanding of the general dynamics of the source and payload, which is important for designing future applications. In this particular experiment designed to study RT instability, the evidence that the instability is principally responsible for the increase in layer width as the seed is increased is compelling, showing promise for future experiments. The fact that CALE reproduces the trends seen in the experiments is not surprising since sensitivity to initial conditions is expected. However, it will be

FIGURE 7. (a) Comparison between CALE (discrete solids 5- μm pore size s ; homogeneous foam 2- μm surface finish u , and 0.2- μm surface finish \emptyset) and two streaks obtained in experiments using rough foam (TPX, Figure 3 left). (b) Au layer width from experiments with rough foam (shaded region) and smooth foam (solid line) compared with CALE (symbols as in 7a) and 1D HYADES.



necessary to measure and model the initial seed more accurately to be more quantitative about comparisons. This may mean mitigating the foam imprint and imposing a surface perturbation on the payload, both of which are possible. In addition to this, the mixing region is 3D and simulations will need to be similarly so. Preliminary 3D calculations using the PROMETHEUS hydrocode²⁰ suggest a growth rate $\sim 20\text{--}30\%$ above the 2D value. Finally, it has been estimated that the Reynolds number of the mixing region is $\sim 10^5\text{--}10^6$, which is adequate for turbulent flow to develop.¹⁹

Calculations aside, it is instructive to estimate a value of α from the experimental data to determine whether the experiments are in the right regime for fundamental turbulent RT studies. For this purpose the smooth foam data is selected because this is more likely to approach self-similar conditions. It is also less likely to be influenced by the finite width of the high-density layer, which 2D simulations suggest is the case (at least up to ~ 3 ns), although further analysis is necessary to confirm this. In the experiment, the diagnostic measures the trajectory of both the leading edge of the Au and the trailing edge, assumed to be the spike front. To proceed, it is assumed the width predicted by the 1D code is accurate. Subtracting this from the data provides the spike height. Simulations in 2D predict $h_b/h_s \approx 0.7$, which is not inconsistent with other simulations and experimental results for an Atwood number ~ 0.7 [Refs. 10 and 11]. This reveals

the bubble height. During the course of the experiment, the mixing region undergoes a gradual, spatially uniform, decompression according to 1D simulation. Removing this decompression provides histories of h_s and h_b . Finally, for variable acceleration, it is expected and has been shown in experiment that $h \approx 2\alpha S$, where $S = 1/2[\int \sqrt{(Ag)} dt]^2$ [Ref. 21]. Values of h are plotted against $2\alpha S$ in Figure 8 from which $\alpha \approx 0.03$ is obtained.

Despite the obvious difficulty of extracting a robust value of α directly from the current experimental data, the important point here is that the mixing layer is clearly approaching the right

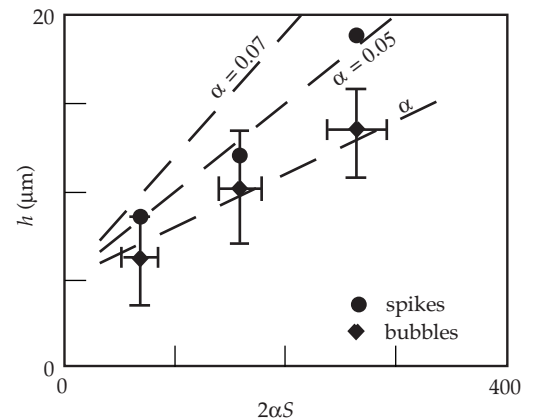


FIGURE 8. Bubble and spike growth as a function of RT scale factor $2\alpha S = 2 \times 1/2[\int \sqrt{(Ag)} dt]^2$. The experimental data suggests $\alpha_b \sim 0.03$.

regime because α is of the right order of magnitude. Thus these experiments appear to be a promising tool for augmenting the experimental database on turbulent RT instability. However, it will be necessary to improve the diagnostic techniques to provide a more direct measurement of the extent of the mixing region, perhaps utilizing absorption spectroscopy^{22,23} and ideally increasing the scale of the experiments. The absorption spectroscopy technique spatially images absorption features due to bound-bound transitions of dopants in the high- and low-density fluids across the mixing layer. This in principle should allow both the distribution of the two fluids across the mixing layer and the position of the bubble and spike fronts. Such experiments will be feasible on the National Ignition Facility at LLNL with scales increased by several fold compared to current facilities.

Summary

In summary, a versatile new source for studying radiation hydrodynamic phenomena is being developed. A bleaching front driven by x rays from a single-ended laser hohlraum heats a low-density foam, which can then drive a payload. Nova experiments have shown that the new driver may be a promising tool for studying turbulent Rayleigh–Taylor instability in the compressible high-temperature plasma regime (≥ 100 eV). It is also possible to generate a variety of acceleration histories and introduce shocks of varying strengths by tailoring the target and laser properties. In these experiments, however, the payload experiences an almost shockless acceleration, which is typically not the case in other laser-driven experiments. This minimizes any Richtmyer–Meshkov instability growth, which otherwise typically complicates the interpretation of the data. The experiments can naturally address the effects of thin layers on instability growth, but they also have the potential to address important questions, such as the influence of initial conditions and compressibility on development of the mixing layer. To this end, a value of $\alpha \sim 0.03$ was estimated from the current data, which is more in line with state-of-the-art incompressible

3D numerical simulations. Further analysis is required, however, to provide a reliable error bar and is in process. In the future, more direct methods to measure the spike and bubble heights, and larger scale experiments are necessary to provide a more robust value of α . This will be possible on the National Ignition Facility.

Notes and References

1. Lord Rayleigh, *Scientific Papers II*, 200, Cambridge, England (1900); G. I. Taylor, *Proc. R. Soc. London, Ser. A* **201**, 192 (1950).
2. R. D. Richtmyer, *Commun. Pure Appl. Math.* **13**, 297, (1960); E. E. Meshkov, *Izv. Acad. Sci. USSR Fluid Dynamics* **4**, 101 (1969).
3. D. Arnett, J. N. Bachal, R. A. Kirshner, and S. E. Woosley, *Annu. Rev. Astron. Astrophys.* **27**, 629 (1989).
4. D. Arnett, B. A. Fryxell, and E. Muller, *Astrophys. J.* **341**, L63 (1989).
5. B. A. Fryxell, E. Muller, and D. Arnett, *Astrophys. J.* **367**, 619 (1991).
6. E. Muller, B. A. Fryxell, and D. Arnett, *Astron. Astrophys.* **251**, 505 (1991).
7. J. Kane, et al., *Phys. Plasmas* **6**(5), 2065 (1999).
8. G. Bazen and D. Arnett, *Astrophys. J.* **496** (1998).
9. Chevalier, Blondin, and Emering, *Astrophys. J.* **392**, 118 (1992); *Ap. J.* **444**, 312 (1992).
10. D. L. Youngs, *Laser and Part. Beams* **12**(4), 725 (1994).
11. U. Alon, J. Hecht, D. Mukamel, and D. Shvarts, *Phys. Rev. Lett.* **27** (18), 2867 (1994); U. Alon, J. Hecht, D. Ofer, and D. Shvarts, *Phys. Rev. Lett.* **74**(4), 534 (1995).
12. J. Glimm, private communication (1999).
13. K. I. Read, *Physica* **D12**, 45 (1984); D. L. Youngs, *Physica* **D37**, 270 (1989).
14. G. Dimonte, *Phys. Plasmas* **6**(5), 2009 (1999).
15. P. Graham et al., *Bull. Amer. Phys. Soc.* **44**(7), 177, (1999).
16. 200 ps was estimated from data in J. D. Lindl, *Phys. Plasmas* (1995).
17. J. T. Larsen, and S. M. Lane, *J. Quant. Spect. Rad. Trans.* **51**, 179 (1994).
18. R. T. Barton, *Numerical Astrophysics* (Jones and Bartlett, Boston, Mass., 1985), pp. 482–497.
19. J. Edwards et al., *Bull. Amer. Phys. Soc.* **44**(7), 177 (1999); P. E. Dimotakis, *J. Fluid Mechanics* **409**, 69 (2000).
20. P. R. Woodward and P. Collela, *J. Comp. Phys.* **54**, 115 (1984).
21. G. Dimonte and M. Scheiner, *Phys. Rev. Lett.* **54**(4), 3740 (1996).
22. J. V. C. Hansom et al., *Laser and Particle Beams* (1984).
23. D. Hoarty, L. Barringer, C. Vickers, and O. Willi, *Phys. Rev. Lett.* **82**(15), 3070 (1999).

NOVA UPDATE APRIL-JUNE 1999

Nova Operations performed 154 experiments during April and May, which exceeded our goal for the quarter. These experiments supported efforts in ICF, Defense Sciences, university collaborations, Laser Science and Nova facility maintenance. The final Nova experiment was conducted on May 27, 1999. The total number of experiments conducted on Nova since its commissioning in 1985 is 13,424. Decommissioning efforts began in early June. By late June, some recipients of Nova components were making final arrangements to ship parts.

The most important experiments during Nova's final quarter were the Petawatt and the cryogenic campaigns. Both campaigns were highly productive and highly successful. The Petawatt experiments demonstrated efficient (40%) conversion

to relativistic electrons, measured the conversion efficiency to >0.5 MeV x rays, studied the production of a 60-MeV collimated proton beam, and investigated evidence of a collimated energy transport by electrons in solid density matter, which is promising for fast ignition concepts. The cryogenic target experiments resulted in numerous measurements. They measured the backscatter from cryogenic gasbags with NIF-like plasma conditions and found that they are close to the expected value. They measured double shock states of liquid deuterium and emulated conditions similar to the second shock state on the NIF. Finally, they determined the dispersion curve for reflectivity of shock compressed deuterium, which allows accurate estimates of the electron carrier density versus pressure up to 8 Mbar.

NATIONAL IGNITION FACILITY UPDATE

APRIL–JUNE 1999

Experience with Integrated Safety Management and the need for better alignment with the National Ignition Facility (NIF) experimental mission have provided substantial reasons for the NIF Laboratory Project Office to evaluate an alternate deployment strategy. This strategy, as discussed in the second quarter issue of 1999 *Quarterly Review*, calls for the completion of the NIF Conventional Facilities and the system “infrastructure” prior to the deployment of the first cluster in Laser Bay 2. Improvement in safety during facility deployment by more effectively separating construction from operations is the anticipated result of this strategy. This strategy will also provide for early “halfraum” experiments followed by symmetric irradiation experiments. Finally, the Project will be able to optimize the design feedback by utilizing the first bundle in Laser Bay 2 uninterrupted for a period of several years.

As the potential new strategy and plans are in development, the Project has placed high priority on the completion of the Title II detail design drawings and procurement packages. While it is believed that the overall progress is satisfactory, a minor schedule concern has now been identified due to the deviation from the completed milestones based on the established baseline.

Overall progress on the NIF site in the third quarter of 1999 was commendable as the total Conventional Facilities work completed reached 70%, compared with 56% at the end of last quarter. Progress on the Laser Building continued to be good, but the pace

in the Target Building and Optics Assembly Building slowed somewhat in June after being good during April and May.

The Laser Bay 2 mat slab was placed on May 15, 1999, permitting the commencement of concrete pedestal construction on June 1, 1999. The overhead work platform was removed, and the two bridge cranes were installed. In Laser Bay 1, the concrete mat slab was placed by the end of June, and the drywall ceiling plenum and finish ceiling grid system were nearly completed, which will allow the removal of the overhead work platform in July. Progress in the Operations Support area in the Laser Building core continued to be good. NIF Day occurred as planned on June 11, 1999. Installation of the Target Chamber sphere occurred the week after the ceremony, and the crane was moved back away from the Target Building early the following week, all as planned. The fifth of seven elevated slab pours for the Target Bay and the second lift of the three Switchyard (SY) 1 walls were placed in June. SY1 is currently scheduled for completion approximately two months ahead of the contract completion date. The second shift in the Optics Assembly Building was curtailed in June. The current goal is to complete the Optical Assembly Building (OAB) by the end of September, which will have no impact on the Project critical path. In Infrastructure, the construction of the SY2 space frame started in mid-June, two months behind the original schedule, and construction of the Laser Bay 2 concrete pedestals started on schedule, June 1, 1999.

In Special Equipment, overall progress was satisfactory. The highest priority in Special Equipment (including Infrastructure) is the completion of the Title II detailed design drawings in preparation for the procurements in each system. Procurement activities continue focusing on the Infrastructure areas along with Laser System area. Procurement reviews were held, and many procurement documents were prepared and reviewed along with the review of vendor submittals. Problem areas being addressed include a transport spatial filter (TSF) center vessel fabrication at Stadco and a recovery of lost schedules for rectangular vacuum beam tubes at Ranor and circular beam tubes at Meyer. NIF Warehouse and forward receiving area continued to receive, store, and conduct inventory control operations for NIF-bound materials using the Glovia system. Activity at the outdoor material storage facility increased considerably with the arrival of several transport spatial filters and support structure components.

In Optics, emphasis continued this quarter on completing vendor facilitization and on optics pilot production activities. Facilitization at Kodak, University of Rochester Laboratory for Laser Energetics (UR/LLE), and Spectra-Physics is proceeding toward

completion in July 1999. In May, the Lawrence Livermore National Laboratory (LLNL) Metrology Facility received the last of seven 24" Wyko interferometers deployed among the NIF optic vendors. Notable progress continued on the potassium dihydrogen phosphate (KDP) facilitization at Cleveland Crystals, and successful growth was completed in May of two KDP boules that could provide up to 15 doubler plates. Production of laser glass cladding began in the third quarter of 1999 at Schott, meeting specifications. The first full-size laser glass pilot slabs were delivered to Zygo for finishing. Pilot production of fused silica optics from Corning was completed in May, and one hundred fused silica blanks were delivered. At the coating vendors, the first large area conditioner is operational at UR/LLE, and the installation of the 18" Zygo interferometer has been completed. The dip-coating system for coating silica optics with sol-gel AR coatings was received from Chemat at LLNL.

Key Assurance activities to support the Project are all on schedule, including construction safety support, litigation support to the Department of Energy for the settlement of 60(b) (e.g., quarterly reports), and the *Final Safety Analysis Report* (FSAR).

PUBLICATIONS AND PRESENTATIONS

APRIL–JUNE 1999

A

Afeyan, B. B., Fleischer, J. W., Geddes, C., Montgomery, D. S., Kirkwood, R., Estabrook, K., Schmitt, A. J., Meyerhofer, D., and Town, R. P. J., *Optical Mixing Controlled Stimulated Scattering Instabilities: Effects of a Large Amplitude Probe Beam on the Backscattering of a Pump Beam*, Lawrence Livermore National Laboratory, Livermore, CA, UCRL-JC-133943-ABS. Prepared for 29th Annual Anomalous Absorption Conf, Pacific Grove, CA, Jun 13, 1999.

Amendt, P., Turner, R. E., Landen, O. L., Decker, C., Glendinning, S. G., Haan, S. W., Jones, O. S., Pollaine, S. M., Suter, L. J., and Wallace, R., *High-Convergence Implosion Studies on the OMEGA Laser with Indirectly-Driven Vacuum Hohlraums*, Lawrence Livermore National Laboratory, Livermore, CA, UCRL-JC-133890-ABS. Prepared for 29th Annual Anomalous Absorption Conf, Pacific Grove, CA, Jun 13, 1999.

Arabadzhi, V. V., Bogatyrev, S. D., Druzhinin, O. A., Kazakov, V. I., Korotkov, D. P., Matusov, P. A., Pugatchev, V. A., Serin, B. V., Talanov, V. I., and Zaborskikh, D. V., *Experimental Study of Internal Waves Generated by a Sphere Moving in a Stratified Fluid with a Thermocline*, Lawrence Livermore National Laboratory, Livermore, CA, UCRL-JC-123583. Submitted to *J. Fluid Mech.*

B

Berger, R. L., Langdon, A. B., Hinkel, D. E., Still, C. H., and Williams, E. A., *Evolution of the Frequency and Wavenumber of the Transmitted and Reflected Light in 3D Simulations*, Lawrence Livermore National Laboratory, Livermore, CA, UCRL-JC-133777-ABS. Prepared for 29th Annual Anomalous Absorption Conf, Pacific Grove, CA, Jun 13, 1999.

Berger, R. L., Langdon, A. B., Rothenberg, J. E., Still, C. H., and Williams, E. A., *Stimulated Raman and Brillouin Scattering of Polarization-Smoothed and Temporally Smoothed Laser Beams*, Lawrence Livermore National Laboratory, Livermore, CA, UCRL-JC-132259; also in *Phys. Plasmas* **6**(4), 1043–1047 (1999).

Boley, C. D., and Rhodes, M. A., *Modeling of a Plasma Electrode Pockels Cell*, Lawrence Livermore National Laboratory, Livermore, CA, UCRL-JC-131445; also in *IEEE Trans. Plasma Sci.* **27**(3), 713–726 (1999).

C

Chang, L., *Lean Manufacture of Assemblies for the National Ignition Facility*, Lawrence Livermore National Laboratory, Livermore, CA, UCRL-JC-134230-ABS. Prepared for 3rd Biennial Tri-Laboratory Engineering Conf on Modeling and Simulation, Pleasanton, CA, Nov 3, 1999.

D

Decker, C., Berger, R. L., Moody, J., Williams, E. A., Suter, L. S., and Lours, L., *Designs of He/H₂ Filled Gasbag Experiments on Nova*, Lawrence Livermore National Laboratory, Livermore, CA, UCRL-JC-134331-ABS. Prepared for 29th Annual Anomalous Absorption Conf, Pacific Grove, CA, Jun 13, 1999.

Dimonte, G., *Nonlinear Evolution of the Rayleigh–Taylor and Richtmyer–Meshkov Instabilities*, Lawrence Livermore National Laboratory, Livermore, CA, UCRL-JC-132439; also in *Phys. Plasmas* **6**(5), Pt.2, 2009–2015 (1999).

Dimonte, G., *Spanwise Homogeneous Buoyancy-Drag Model for Rayleigh–Taylor Mixing and Comparison with Experiments*, Lawrence Livermore National Laboratory, Livermore, CA, UCRL-JC-133936. Submitted to *Phys. of Plasmas*.

Ditmire, T., Zweiback, J., Yanovsky, V. P., Cowan, T. E., Hays, G., and Wharton, K. B., *Nuclear Fusion from Explosions of Femtosecond Laser-Heated Deuterium Clusters*, Lawrence Livermore National Laboratory, Livermore, CA, UCRL-JC-135040; also in *Nature* **398**(6727), 489–492 (1999).

Dittrich, T. R., Haan, S. W., Marinak, M. M., Pollaine, S. M., Hinkel, D. E., Munro, D. H., Verdon, C. P., Strobel, G. L., McEachern, R., Cook, R. C., Roberts, C. C., Wilson, D. C., Bradley, P. A., Foreman, L. R., and Varnum, W. S., *Review of Indirect-Drive Ignition Design Options for the National Ignition Facility*, Lawrence Livermore National Laboratory, Livermore, CA, UCRL-JC-131383; also in *Phys. Plasmas* **6**(5), Pt. 2, 2164–2170 (1999).

F

Fearon, E., *Characterization of Russian Ballistic Furnace Shells, February, 1999, Batch*, Lawrence Livermore National Laboratory, Livermore, CA, UCRL-ID-133929.

G

Geddes, C. G. R., Afeyan, B. B., Fleischer, J. W., Kirkwood, R. K., Montgomery, D. S., Meyerhofer, D., Seka, W., Estabrook, K., Schmitt, A. J., and Town, R. P. J., *Backscatter and Transmitted Beam Measurements at OMEGA for Optical Mixing and Other Experiments*, Lawrence Livermore National Laboratory, Livermore, CA, UCRL-JC-133941-ABS. Prepared for 29th Annual Anomalous Absorption Conf, Pacific Grove, CA, Jun 13, 1999.

Geddes, C. G. R., Kirkwood, R. K., Glenzer, S. H., Estabrook, K. G., Joshi, C., and Wharton, K. B., *Study of the Saturation of Stimulated Raman Scattering by Secondary Decays*, Lawrence Livermore National Laboratory, Livermore, CA, UCRL-JC-130328-ABS Rev. Prepared for 29th Annual Anomalous Absorption Conf, Pacific Grove, CA, Jun 13, 1999.

Glendinning, S. G., Remington, B. A., Wallace, R. J., Galmiche, D., Cherfils, C., Holstein, P. A., and Richard, A., *Ablative Rayleigh–Taylor Instability in Spherically Convergent Geometry*, Lawrence Livermore National Laboratory, Livermore, CA, UCRL-JC-133828-ABS. Prepared for 29th Annual Anomalous Absorption Conf, Pacific Grove, CA, Jun 13, 1999.

Glenzer, S. H., Alley, W. E., Estabrook, K. G., De Groot, J. S., Haines, M. G., Hammer, J. H., Jadaud, J.-P., MacGowan, B. J., Moody, J. D., Rozmus, W., Suter, L. J., Weiland, T. L., and Williams, E. A., *Thomson Scattering from Laser Plasmas*, Lawrence Livermore National Laboratory, Livermore, CA, UCRL-JC-131357; also in *Phys. Plasmas* **6**(5), Pt. 2, 2117–2128 (1999).

Glenzer, S. H., Estabrook, K. G., Lee, R. W., MacGowan, B. J., and Rozmus, W., *Detailed Characterization of Laser Plasmas for Benchmarking of Radiation-Hydrodynamic Modeling*, Lawrence Livermore National Laboratory, Livermore, CA, UCRL-JC-133739. Submitted to *J. Quant. Spectros. and Radiat. Transfer*.

Glenzer, S. H., Geddes, C. G., Kirkwood, R. K., MacGowan, B. J., Moody, J. D., and Young, P. E., *Thomson Scattering on Ion Waves Driven by SBS in Large-Scale Length Plasmas*, Lawrence Livermore National Laboratory, Livermore, CA, UCRL-JC-133945-ABS. Prepared for 29th Annual Anomalous Absorption Conf, Pacific Grove, CA, Jun 13, 1999.

H

Haan, S. W., Jones, O. S., Dittrich, T. R., Koch, J. A., Sangster, T. C., and Edwards, M. J., *Diagnosis of Ignition Shots on NIF: How Will We Know What Happened?* Lawrence Livermore National Laboratory, Livermore, CA, UCRL-JC-133724-ABS. Prepared for Anomalous Absorption Conf, Monterey, CA, Jun 13, 1999.

Haber, I., Friedman, A., Grote, D. P., Lund, S. M., and Kishkek, R. A., "Recent Progress in the Simulation of Heavy Ion Beams," *Phys. Plasmas* 6(5), Pt. 2, 2254-2261 (1999).

Hammer, J. H., Tabak, M., Wilks, S. C., Lindl, J. D., Bailey, D. S., Rambo, P. W., Toor, A., Zimmerman, G. B., and Porter Jr., J. L., *High Yield Inertial Confinement Fusion Target Design for a Z-Pinch Driven Hohlraum*, Lawrence Livermore National Laboratory, Livermore, CA, UCRL-JC-131389; also in *Phys. Plasmas* 6(5), Pt. 2, 2129-2136 (1999).

Hatchett, S., Snavely, R. A., Key, M., Brown, C., Cowan, T., Henry, G., Langdon, B., Lasinski, B., Pennington, D., and Perry, M., *Observation and Interpretation of the Angular Patterns and Characteristic Energies of Relativistic Electrons Ejected from Petawatt Laser Targets*, Lawrence Livermore National Laboratory, Livermore, CA, UCRL-JC-133725-ABS. Prepared for Anomalous Absorption Conf, Monterey, CA, Jun 13, 1999.

Hinkel, D. E., and Haan, S. W., *Laser-Plasma Interactions in the 350-eV National Ignition Facility Target*, Lawrence Livermore National Laboratory, Livermore, CA, UCRL-JC-133083-ABS Rev. Prepared for 29th Annual Anomalous Absorption Conf, Pacific Grove, CA, Jun 13, 1999.

J

Jones, O. S., Suter, L. J., Marinak, M. M., and Kerbel, G. D., *Radiation Environment in Nonsymmetric NIF Hohlräume*, Lawrence Livermore National Laboratory, Livermore, CA, UCRL-JC-134038-ABS. Prepared for 29th Annual Anomalous Absorption Conf, Pacific Grove, CA, Jun 13, 1999.

K

Kalantar, D., and Dixit, S., *Baseline Unconverted Light Management Plan (Indirect Drive Configuration)*, Lawrence Livermore National Laboratory, Livermore, CA, UCRL-ID-134173.

Kane, J. O., Arnett, D., Remington, B. A., Glendinning, S. G., Wallace, R., Ryutov, D., Drake, R. P., Rubenchik, A., and Teyssier, R., *Scaling Supernova Hydrodynamics to the Laboratory*, Lawrence Livermore National Laboratory, Livermore, CA, UCRL-JC-132438-ABS Rev. Prepared for 94th Mtg of the American Astronomical Society, Chicago, IL, May 30, 1999.

Kane, J., Arnett, D., Remington, B. A., Glendinning, S. G., Bazan, S. G., Drake, R. P., Fryxell, B. A., Teyssier, R., and Moore, K., *Scaling Supernova Hydrodynamics to the Laboratory*, Lawrence Livermore National Laboratory, Livermore, CA, UCRL-JC-132438; also in *Phys. Plasmas* 6(5), Pt. 2, 2065-2071 (1999).

Kauffman, R., *1998 Inertial Confinement Fusion Annual Report*, Lawrence Livermore National Laboratory, Livermore, CA, UCRL-LR-105820-98.

Kauffman, R., *Inertial Confinement Fusion Monthly Highlights*, March 1999, Lawrence Livermore National Laboratory, Livermore, CA, UCRL-TB-128550-99-6.

Kauffman, R., *Inertial Confinement Fusion Monthly Highlights*, April 1999, Lawrence Livermore National Laboratory, Livermore, CA, UCRL-TB-128550-99-7.

Kauffman, R., *Inertial Confinement Fusion Monthly Highlights*, May 1999, Lawrence Livermore National Laboratory, Livermore, CA, UCRL-TB-128550-99-8.

Key, M. H., Campbell, E. M., Cowan, T. E., Hammel, B. A., Hatchett, S. P., Henry, E. A., Kilkenny, J. D., Koch, J. A., Langdon, A. B., and Lasinski, B. F., *Studies of the Prospects for Fast Ignition Using a Petawatt Laser Facility*, Lawrence Livermore National Laboratory, Livermore, CA, UCRL-JC-134181-ABS. Prepared for *Advanced High Power Lasers and Applications*, Osaka, Japan, Nov 1, 1999.

Kirkwood, R. K., Berger, R. L., Geddes, C. G., Glenzer, S. H., Langdon, A. B., MacGowan, B. J., Moody, J. D., and Young, P. E., *Experimental Study of the Effect of Speckle Size on Backscatter in a Phase Plate Smoothed Beam*, Lawrence Livermore National Laboratory, Livermore, CA, UCRL-JC-133944-ABS. Prepared for *29th Annual Anomalous Absorption Conf*, Pacific Grove, CA, Jun 13, 1999.

Koch, J., Key, M., Lee, R., Hatchett, S., Brown, C., and Pennington, D., *Experimental Measurements of Deep Heating Generated by Ultra-Intense Laser-Plasma Interactions*, Lawrence Livermore National Laboratory, Livermore, CA, UCRL-JC-133831-ABS. Prepared for *29th Annual Anomalous Absorption Conf*, Pacific Grove, CA, Jun 13, 1999.

L

Labaune, C., Baldis, H. A., Cohen, B., Rozmus, W., Depierreux, S., Schifano, E., Bauer, B. S., and Michard, A., "Nonlinear Modification of Laser-Plasma Interaction Processes under Crossed Laser Beams," *Phys. Plasmas* 6(5), Pt. 2, 2048–2056 (1999).

Landen, O. L., Amendt, P. A., Suter, L. J., Turner, R. E., Glendinning, S. G., Haan, S. W., Pollaine, S. M., Hammel, B. A., Tabak, M., Rosen, M. D., and Lindl, J. D., *A Simple Time-Dependent Analytic Model of the P_2 Asymmetry in Cylindrical Hohlraums*, Lawrence Livermore National Laboratory, Livermore, CA, UCRL-JC-132445; also in *Phys. Plasmas* 6(5), Pt. 2, 2137–2143 (1999).

Lasinski, B. F., Langdon, A. B., Hatchett, S. P., Key, M. H., and Tabak, M., *Particle in Cell Simulations of Ultra Intense Laser Pulses Propagating Through Overdense Plasma for Fast-Ignitor and Radiography Applications*, Lawrence Livermore National Laboratory, Livermore, CA, UCRL-JC-131245; also in *Phys. Plasmas* 6(5), Pt. 2, 2041–2047 (1999).

M

Mackinnon, A. J., Brown, C. G., Ditmire, T., Hatchett, S., Koch, J., Key, M. H., Moody, J., Offenberger, A. A., Pennington, D., and Perry, M. D., *Study of the Interaction of Ultra-Intense Laser Pulses with Solid Targets on the Petawatt Laser System*, Lawrence Livermore National Laboratory, Livermore, CA, UCRL-JC-133976-ABS. Prepared for *29th Annual Anomalous Absorption Conf*, Pacific Grove, CA, Jun 13, 1999.

Moody, J. D., MacGowan, B. J., Decker, C. D., Glenzer, S. H., Kirkwood, R. K., Young, P. E., Berger, R. L., Collins, G. W., Geddes, C. G., and Sanchez, J. A., *Measurements of SRS and SBS Backscattered Light from He/H₂ Cryogenic Nova Gasbag Targets*, Lawrence Livermore National Laboratory, Livermore, CA, UCRL-JC-133942-ABS. Prepared for *29th Annual Anomalous Absorption Conf*, Pacific Grove, CA, Jun 13, 1999.

N

Nash, T. J., Derzon, M. S., Chandler, G. A., Leeper, R., Fehl, D., Lash, J., Ruiz, C., Cooper, G., Seaman, J. F., McGum, J., Lazier, S., Torres, J., Jobe, D., Gilliland, T., Hurst, M., Mock, R., Ryan, P., Nielsen, D., Armijo, J., McKenney, J., Hawn, R., Hebron, D., MacFarlane, J. J., Petersen, D., Bowers, R., Matuska, W., and Ryutov, D. D., "High-Temperature Dynamic Hohlraums on the Pulsed Power Driver Z," *Phys. Plasmas* 6(5), Pt. 2, 2023–2029 (1999).

P

Pennington, D., Brown, C. G., Cowan, T. E., Fountain, W., Hatchett, S. P., Henry, E., Hunt, A. W., Johnson, J., Kartz, M., and Key, M., *Petawatt Experiments at LLNL*, Lawrence Livermore National Laboratory, Livermore, CA, UCRL-JC-133590-ABS. Darmstadt, Germany, July 2, 1999.

Perry, M. D., Stuart, B. C., Banks, P. S., Feit, M. D., Yanovsky, V., and Rubenchik, A. M., *Ultrashort-Pulse Laser Machining of Dielectric Materials*, Lawrence Livermore National Laboratory, Livermore, CA, UCRL-JC-132156; also in *J. Appl. Phys.* **85**(9), 6803–6810 (1999).

Pollaine, S., Bradley, D., Landen, O., Wallace, R., Jones, O., Amendt, P., Glendinning, G., Turner, R., and Suter, L., *P6 and P8 Modes in NIF Hohlräume*, Lawrence Livermore National Laboratory, Livermore, CA, UCRL-JC-133888-ABS. Prepared for *29th Annual Anomalous Absorption Conf*, Pacific Grove, CA, Jun 13, 1999.

R

Remington, B. A., Arnett, D., Drake, R. P., and Takabe, H., "Modeling Astrophysical Phenomena in the Laboratory with Intense Lasers," *Science* **284**, 1488–1493 (1999).

Rosen, M. D., *The Physics Issues That Determine Inertial Confinement Fusion Target Gain and Driver Requirements: A Tutorial*, Lawrence Livermore National Laboratory, Livermore, CA, UCRL-JC-131381; also in *Phys. Plasmas* **6**(5), Pt. 2, 1690–1699 (1999).

Ryutov, D., Drake, R. P., Kane, J., Liang, E., Remington, B. A., and Wood-Vasey, W. M., *Similarity Criteria for the Laboratory Simulations of Supernova Hydrodynamics*, Lawrence Livermore National Laboratory, Livermore, CA, UCRL-JC-130956; also in *Astrophys. J.* **518**(N2PT1), 821–832 (1999).

S

Sathyam, U. S., Colston Jr., B. W., Da Silva, L. B., and Everett, M. J., *Evaluation of Optical Coherence Quantitation of Analytes in Turbid Media by Use of Two Wavelengths*, Lawrence Livermore National Laboratory, Livermore, CA, UCRL-JC-131433; also in *Appl. Optics* **38**(10), 2097–2104 (1999).

Sheehan, L., *NIF Small Optics Laser Damage Test Specifications*, Lawrence Livermore National Laboratory, Livermore, CA, UCRL-ID-133979.

Shigemori, K., Ditmire, T., Remington, B. A., Estabrook, K. G., Farley, D. R., Ryutov, D. D., Rubenchik, A. M., Kodama, R., Koase, T., and Ochi, Y., *Radiative Hydrodynamics Experiments for Astrophysics*, Lawrence Livermore National Laboratory, Livermore, CA, UCRL-JC-133835-ABS. Prepared for *29th Annual Anomalous Absorption Conf*, Pacific Grove, CA, Jun 13, 1999.

Sommer, S., Trummer, D. J., MacCalden, P. B., and Gerhard, M. A., *Seismic Analyses of NIF Structures*, Lawrence Livermore National Laboratory, Livermore, CA, UCRL-JC-134210-ABS. Prepared for *3rd Biennial Tri-Laboratory Engineering Conf on Modeling & Simulation*, Pleasanton, CA, Nov 3, 1999.

Suter, L., Porter, J., Bourgaude, J., Kauffman, R., Simmons, W., and Turner, R., *Requirements for NIF's Soft X-Ray Drive Diagnostic*, Lawrence Livermore National Laboratory, Livermore, CA, UCRL-JC-133889-ABS. Prepared for *29th Annual Anomalous Absorption Conf*, Pacific Grove, CA, Jun 13, 1999.

Suter, L., Van Wonterghem, B., Munro, D., Haan, S., Pollaine, S., and Tabak, M., *Feasibility of High Yield/High Gain NIF Capsules*, Lawrence Livermore National Laboratory, Livermore, CA, UCRL-JC-133887-ABS. Prepared for *29th Annual Anomalous Absorption Conf*, Pacific Grove, CA, Jun 13, 1999.

V

Van Wonterghem, B., Hibbard, W., Kalantar, D., Lee, F. D., MacGowan, B. J., Pittenger, L., Tobin, M., and Wong, K., *Target Experimental Area and Systems of the National Ignition Facility (NIF)*, Lawrence Livermore National Laboratory, Livermore, CA, UCRL-JC-134007-ABS. Prepared for *1st Intl Conf on Inertial Fusion Sciences and Applications*, Bordeaux, France, Sept 12, 1999.

W

Wallace, J. M., Murphy, T. J., Delamater, N. D., Klare, K. A., Oertel, J. A., Magelssen, G. R., Lindman, E. L., Hauer, A. A., Gobby, P., Schnittman, J. D., Craxton, R. S., Seka, W., Kremens, R., Bradley, D., Pollaine, S. M., Turner, R. E., Landen, O. L., Drake, D., and MacFarlane, J. J., "Inertial Confinement Fusion with Tetrahedral Hohlräume at OMEGA," *Phys. Rev. Lett.* **82**(19), 3807–3810 (1999).

Wharton, K. B., Kirkwood, R. K., Glenzer, S. H., Estabrook, K. G., Afeyan, B. B., Cohen, B. I., Moody, J. D., MacGowan, B. J., and Joshi, C., *Observation of Resonant Energy Transfer between Identical-Frequency Laser Beams*, Lawrence Livermore National Laboratory, Livermore, CA, UCRL-JC-130320; also in *Phys. Plasmas* **6**(5), Pt. 2, 2144–2149 (1999).

Williams, E. A., Langdon, A. B., Still, C. H., Berger, R. L., and Dixit, S. N., *F3D Simulations of the Propagation of Nova Beams in Gasbag Targets*, Lawrence Livermore National Laboratory, Livermore, CA, UCRL-JC-133775-ABS. Prepared for 29th Annual Anomalous Absorption Conf, Pacific Grove, CA, Jun 13, 1999.

Williams, W., *FSFIN, Version 1.0*, Lawrence Livermore National Laboratory, Livermore, CA, UCRL-CODE-99022.

Williams, W., *GMPFIN, Version 1.0*, Lawrence Livermore National Laboratory, Livermore, CA, UCRL-CODE-99021.

Wootton, A. J., *Fusion Research and the Developing Nations*, Lawrence Livermore National Laboratory, Livermore, CA, UCRL-JC-134097. Submitted to *Phys. Community News*.

Z

Zweiback, J., Ditmire, T., and Perry, M. D., *Femtosecond Time-Resolved Studies of the Dynamics of Noble-Gas Cluster Explosions*, Lawrence Livermore National Laboratory, Livermore, CA, UCRL-JC-131241; also in *Phys. Rev. A* **59**(5), R3166–R3169 (1999).

ICF/NIF and HEDES Program
Lawrence Livermore National
Laboratory
P.O. Box 808, L-475
Livermore, California 94551

Address Correction Requested